Description and basic evaluation of simulated mean state, internal variability, and climate sensitivity in MIROC6

Hiroaki Tatebe[1], Tomoo Ogura[2], Tomoko Nitta[3], Yoshiki Komuro[1], Koji Ogochi[1], Toshihiko Takemura[4], Kengo Sudo[5], Miho Sekiguchi[6], Manabu Abe[1], Fuyuki Saito[1], Minoru Chikira[3], Shingo Watanabe[1], Masato Mori[7], Nagio Hirota[2], Yoshio Kawatani[1], Takashi Mochizuki[1], Kei Yoshimura[3], Kumiko Takata[2], Ryouta O'ishi[3], Dai Yamazaki[8], Tatsuo Suzuki[1], Masao Kurogi[1], Takahito Kataoka[1], Masahiro Watanabe[3], and Masahide Kimoto[3]

1: Japan Agency for Marine-Earth Science and Technology, Yokohama, Japan

2: National Institute for Environmental Studies, Tsukuba, Japan

3: Atmosphere and Ocean Research Institute, University of Tokyo, Kashiwa, Japan

4: Research Institute for Applied Mechanics, Kyushu University, Kasuga, Japan

5: Graduate School of Environmental Studies, Nagoya University, Nagoya, Japan

6: Tokyo University of Marine Science and Technology, Tokyo, Japan

7: Research Center for Advanced Science and Technology, University of Tokyo, Tokyo, Japan

8: Institute of Industrial Sciences, University of Tokyo, Tokyo, Japan

Corresponding author: Hiroaki Tatebe (E-mail: tatebe@jamstec.go.jp)

Research Center for Environmental Modeling and Application, Japan Agency for Marine-Earth Science and Technology

3173-25 Showamachi, Kanazawaku, Yokohama, Kanagawa 236-0001, Japan

Abstract

The sixth version of the Model for Interdisciplinary Research on Climate (MIROC), called MIROC6, was cooperatively developed by a Japanese modeling community. In the present manuscript, simulated mean climate, internal climate variability, and climate sensitivity in MIROC6 are evaluated and briefly summarized in comparison with the previous version of our climate model (MIROC5) and observations. The results show that overall reproducibility of mean climate and internal climate variability in MIROC6 is better than that in MIROC5. The tropical climate systems (e.g., summertime precipitation in the western Pacific and the eastward propagating Madden-Julian Oscillation) and the mid-latitude atmospheric circulations (e.g., the westerlies, the polar night jet, and troposphere-stratosphere interactions) are significantly improved in MIROC6. These improvements can be attributed to the newly implemented parameterization for shallow convective processes and to the inclusion of the stratosphere . While there are significant differences in climates and variabilities between the two models, the effective climate sensitivity of 2.5 K remains the same because the differences in radiative forcing and climate feedback tend to offset each other. With an aim towards contributing to the sixth phase of the Coupled Model Intercomparison Project, designated simulations tackling a wide range of climate science issues, as well as seasonal-to-decadal climate predictions and future climate projections, are currently ongoing using MIROC6.

41 **1 Introduction**

42 As the global warming due to increasing emissions of the anthropogenic greenhouse gases
43 progresses, global and regional patterns of atmospheric circulations and precipitation as well as
44 temperature are projected to be drastically changed until the end of the twentieth-first century (e.g.,
45 Neelin et al., 2006; Zhang et al., 2007; Bengtsson et al., 2009; Andrews et al., 2010; Scaife et al.,
46 2012) and that occurrence frequency of extreme weather events such as heatwaves, droughts will be
47 increased and extratropical cyclones will be stronger than in the present (e.g., Mizuta et al., 2012;
48 Sillmann et al., 2013; Zappa et al., 2013). Corresponding to the atmospheric changes under the global
49 warming, the sea levels will rise due to the thermal expansion of sea water and ice-sheet melting in
50 the polar continental regions (e.g., Church and White, 2011; Bamber and Aspinall, 2013). Additionally,
51 ocean acidification due to absorption of atmospheric carbon dioxide (CO_2) and changes in carbon-
52 nitrogen cycles are expected to lead to the loss of Earth biodiversity (e.g., Riebesell et al., 2009;
53 Rockström, et al. 2009; Taucher and Oschlies, 2011; Watanabe et al., 2017). Societal demands for
54 information on the global and regional climate changes have increased significantly worldwide in
55 order to meet information requirements for political decision making related to mitigation and
56 adaptation to the global warming.

57 The Intergovernmental Panel on Climate Change (IPCC) has continuously published the
58 assessment reports (ARs) in which a comprehensive view of past, present, and future climate changes
59 on various timescales, including the centennial global warming, are synthesized. Together with
60 observations, climate models have been contributing to the IPCC-ARs through a broad range of
61 numerical simulations, especially, future climate projections after the twenty-first century. However,
62 there are many uncertainties in future climate projections and the range of uncertainties has not been
63 narrowed by an update of the IPCC reports. The uncertainties are arising from imperfections of climate
64 models in representing micro- to global-scale physical and dynamical processes in sub-systems of the

Earth's climate and their interactions. To reduce the uncertainties and errors in climate projections and predictions, utilizing observations, extracting essences of physical processes in the real climate, and investigating the response of the climate system to various external forcings based on a set of climate model simulations are necessary. In particular, a state-of-the-art climate model which can represent various processes in the Earth's climate system is a powerful tool for deeper understanding the Earth's climate system.

One of Japanese climate models, which is called MIROC (Model for Interdisciplinary Research on Climate), has been cooperatively developed at the Center for Climate System Research (CCSR; the precursor of a part of the Atmosphere and Ocean Research Institute), the University of Tokyo, the Japan Agency for Marine-Earth Science and Technology (JAMSTEC), and the National Institute for Environmental Studies (NIES). Utilizing MIROC, our Japanese climate modelling group has been tackling a wide range of climate science issues and seasonal-to-decadal climate predictions and future climate projections. At the same time, by providing simulation data, we have been participating to the third and fifth phases of the Coupled Model Intercomparison Projects (CMIP3 and CMIP5; Meehl et al. 2007; Taylor et al. 2011) which have been contributing to the IPCC-ARs by synthesizing multi-model ensemble datasets.

In the years up to the IPCC fifth assessment report (IPCC-AR5; IPCC 2013), we have developed four versions of MIROC, three of which (MIROC3m, MIROC3h, and MIROC4h) have almost the same dynamical and physical packages, but different resolutions. MIROC3m (K-1 model developers, 2004) is composed of T42L20 atmosphere and 1.4°L43 ocean. Resolutions of MIROC3h (K-1 model developers, 2004) are higher than MIROC3m and are T106L56 for the atmosphere and eddy-permitting for the ocean (1/4° × 1/6°). Only the horizontal resolution of the atmosphere of MIROC3h is changed to T213 in MIROC4h (Sakamoto et al., 2012). MIROC5 is composed of T85L40 atmosphere and 1.4°L50 ocean, but with considerably updated physical and dynamical packages

(Watanabe et al., 2010). These models have been used to study various scientific issues such as the detection of natural influences on climate changes (e.g., Nozawa et al., 2005; Mori et al, 2014; Watanabe et al., 2014), uncertainty quantification of climate sensitivity (e.g., Shiogama et al., 2012; Kamae et al., 2016), future projections of regional sea-level rises (e.g., Suzuki et al., 2005; Suzuki and Ishii, 2011), and mechanism studies on tropical decadal variability (e.g., Tatebe et al., 2013; Mochizuki et al., 2016).

During the last decade, our efforts have been preferentially devoted to providing science-oriented risk information on climate changes that is beneficial to international, domestic, and municipal communities. For example, so-called event attribution (EA) studies with large ensemble simulations initiated from slightly different conditions have been conducted in order to statistically evaluate influences of the global warming on the occurrence frequencies of observed individual extremes (e.g., Imada et al., 2013; Watanabe et al., 2013; Shiogama et al., 2014). Seasonal-to-decadal climate predictions are also of significant concerns. By initializing prognostic variables in our climate models using observation-based data (Tatebe et al., 2012), significant prediction skills in several specific phenomena, such as the El Niño/Southern Oscillation (ENSO) and the Arctic sea-ice extent on seasonal timescales, the Pacific Decadal Oscillations (PDO; Mantua et al., 1997), the Atlantic Multi-decadal Oscillations (AMO; Schlesinger and Ramankutty, 2004), and the tropical trans-basin interactions between the Pacific and the Atlantic on decadal timescales, are detected (e.g., Mochizuki et al., 2010; Chikamoto et al. 2015; Imada et al., 2015; Ono et al., 2018).

However, while the applicability of MIROC has been extended to a wide range of climate science issues, almost all of the above-mentioned approaches were based on our medium-resolution versions of MIROC (MIROC3m and MIROC5), and it is well known that higher-resolution models are capable of better representing the model mean climate and internal climate variability, such as regional extremes, orographic winds, and oceanic western boundary currents/eddies than lower-

113 resolution models (e.g., Shaffrey et al., 2009; Roberts et al., 2009; Sakamoto et al., 2012). Nevertheless,
114 there remain persistent biases associated with, for example, cloud-aerosol-radiative feedback and
115 turbulent vertical mixing of the air in the planetary boundary layer (e.g., Bony and Dufresne, 2005;
116 Bodas-Salcedo et al., 2012; Williams et al., 2013), which are tightly linked with dominant uncertainties
117 in climate projections. Therefore, improvement of physical parameterizations for sub-grid scale
118 processes is essential for better representing observed climatic-mean states and internal climate
119 variability. As well as physical parameterizations, enhanced vertical resolution in both of atmosphere
120 and ocean components, along with a highly accurate tracer advection scheme, have been suggested to
121 have impacts on reproducibility of model-climate and internal climate variations (e.g., Tatebe and
122 Hasumi, 2010; Ineson and Scaife, 2009; Scaife et al., 2012).
123 Recently, we have developed the sixth version of MIROC, called MIROC6. This newly
124 developed climate model has updated physical parameterizations in all sub-modules. In order to
125 suppress an increase of computational cost, the horizontal resolutions of MIROC6 are not significantly
126 higher than those of MIROC5. The reason is that a larger number of ensemble members are required
127 to realize significant seasonal predictions of, for example, the wintertime Eurasian climate (Murphy
128 et al., 1990; Scaife et al., 2014). Indeed, climate predictions by the older versions of MIROC having
129 at most 10 ensemble members are skillful only in the tropical climate and the mid-latitude ocean not
130 in the mid-latitude atmosphere. Large ensemble predictions are also required in decadal-scale
131 predictions in order to evaluate the human influences on the near-term climate changes. The model
132 top in MIROC6 is placed at the 0.004 hPa pressure level which is higher than that of MIROC5 (3 hPa),
133 and the stratospheric vertical resolution has been enhanced in comparison to MIROC5 in order to
134 represent the stratospheric circulations. Overall, the reproducibility of the mean climate and internal
135 variability of MIROC6 is better than those of MIROC5, but the model's computational cost is about
136 3.6 times as large as that of MIROC5. Considering that the computational costs of large ensemble

predictions based on climate models with horizontal resolutions of, for example, 50 km atmosphere and eddy-resolving ocean are still huge on recent computer systems, the use of relatively low resolution models such as MIROC6 with further elaborated parameterizations can still be actively useful in science-oriented climate studies and climate predictions produced for societal needs.

The rest of the present paper is organized as follows. We describe the model configuration, tuning and spin-up procedures in Section 2, while simulated mean-state, internal variability, and climate sensitivity are evaluated in Section 3. Simulation performance of MIROC6 and remaining issues are briefly summarized and discussed in Section 4. Currently, MIROC6 is being used for various simulations designed by the sixth phase of the CMIP (CMIP6; Eyring et al., 2016), which aims to strengthen the scientific basis of the IPCC-AR6. Large ensemble simulations and climate predictions using MIROC6 are also on-going for science-oriented studies in our modeling group and for societal benefits. In addition, the latest earth system model version of MIROC with the global carbon cycle, whose physical core will be MIROC6, has been developed for the CMIP6 towards further wide range issues of climate and societal applications (Hajima et al., in preparation).

2 Model configurations and spinup procedures

MIROC6 is composed of three sub-models: atmosphere, land, and sea ice-ocean. The atmospheric model is based on the CCSR-NIES atmospheric general circulation model (AGCM; Numaguti et al., 1997). The land surface model is based on Minimal Advanced Treatments of Surface Interaction and Runoff (MATSIRO; Takata et al. 2003), which includes a river routing model of Oki and Sud (2003) based on a kinematic wave flow equation (Ngo-Duc et al., 2007) and a lake module where one-dimensional thermal diffusion and mass conservation are considered. The sea ice-ocean model is based on the CCSR Ocean Component model (COCO; Hasumi, 2006). A coupler system calculates heat and freshwater fluxes between the sub-models in order to ensure that all fluxes are

161 conserved within machine precision and then exchanges the fluxes among the sub-models (Suzuki et
162 al., 2009). No flux adjustments are used in MIROC6. In the remaining part of this section, we will
163 provide details of MIROC6 configurations, focusing on updates from MIROC5. Readers may also
164 refer to Table A in Appendix where the updates are briefly summarized.
165
166 **2.1 Atmospheric component**
167 MIROC6 employs a spectral dynamical core in its AGCM component as in MIROC5. The
168 horizontal resolution is a T85 spectral truncation that is an approximately 1.4° grid interval for both
169 latitude and longitude. The vertical grid coordinate is a hybrid σ-p coordinate (Arakawa and Konor,
170 1996). The model top is placed at 0.004 hPa, and there are 81 vertical levels (Fig. 1a). The vertical
171 grid arrangement in MIROC6 is considerably enhanced in comparison to that in MIROC5 (40 levels;
172 3 hPa) in order that the stratospheric circulations can be represented. A sponge layer that damps wave
173 motions is set at the model top level by increasing Rayleigh friction to prevent extra wave reflection
174 near the model top. The atmospheric component of MIROC6 has standard physical parameterizations
175 for cumulus convections, radiation transfer, cloud microphysics, turbulence, and gravity wave drag. It
176 also has an aerosol module. These are basically the same as those used in MIROC5, but several updates
177 have been made, as will be detailed below. The parameterizations for cloud micro-physics and
178 planetary boundary layer processes in MIROC6 are the same as in MIROC5. The standard timestep
179 for MIROC6 is 6 minutes which is shorter than that of MIROC5 (12 minutes) because stratospheric
180 winds whose speed sometimes exceeds 150 ms^{-1} must be resolved in time integration. The timestep
181 for radiative transfer models is set separately and is 3 hours in both of MIROC6 and MIROC5.
182 A cumulus parameterization proposed by Chikira and Sugiyama (2010), which uses an
183 entrainment formulation of Gregory (2001), is adopted in MIROC6 as in MIROC5. This
184 parameterization deals with multiple cloud types including shallow cumulus and deep convective

clouds. MIROC5, however, tends to overestimate the low-level cloud amounts over the low-latitude oceans and has a dry bias in the free troposphere. These biases appear to be the result of insufficient vertical mixing of the humid air in the planetary boundary layer and the dry air in the free troposphere. To alleviate these biases, an additional parameterization for shallow cumulus convection based on Park and Bretherton (2009) is implemented in MIROC6. Shallow convections associated with the atmospheric instability are calculated by the Chikira and Sugiyama (2010) scheme, and those associated with turbulence in the planetary boundary layer are represented by the Park and Bretherton (2009) scheme. The shallow convective parameterization is a mass flux scheme based on a buoyancy-sorting, entrainment-detrainment single plume model that calculates the vertical transport of liquid water, potential temperature, total water mixing ratio, and horizontal winds in the lower troposphere. The cloud-base mass flux is controlled by turbulent kinetic energy within the sub-cloud layer and convective inhibition. The cloud-base height for shallow cumulus is set between the lifting condensation level and the boundary layer top, which is diagnosed based on the vertical profile of relative humidity. When implementing the parameterization in MIROC6, the following conditions for triggering the shallow convection are specified: 1) The estimated inversion strength (Wood and Bretherton, 2006) is smaller than a tuning parameter, and 2) the convection depth diagnosed by a separate cumulus convection scheme (Chikira and Sugiyama, 2010) is smaller than a tuning parameter.

The Spectral Radiation-Transport Model for Aerosol Species (SPRINTARS; Takemura et al., 2000, 2005, 2009) is used as an aerosol module for MIROC6 to predict the mass mixing ratios of the main tropospheric aerosols which are black carbon, organic matter, sulfate, soil dust, and sea salt, and the precursor gases of sulfate (sulfur dioxide, SO_2, and dimethylsulfide). By coupling the radiation and cloud-precipitation schemes in MIROC, SPRINTARS calculates not only the aerosol transport processes of emission, advection, diffusion, sulfur chemistry, wet deposition, dry deposition, and gravitational settling, but also the aerosol-radiation and aerosol-cloud interactions. There are two

primary updates in SPRINTARS of MIROC6 that were not included in MIROC5. One is the treatment of precursor gases of organic matters as prognostic variables. In the previous version, the conversion rates from the precursor gases (e.g., terpene and isoprene) to organic matters are prescribed (Takemura et al., 2000), while an explicit simplified scheme for secondary organic matters was introduced from a global chemical climate model (Sudo et al., 2002). The other is a treatment of oceanic primary and secondary organic matters. Emissions of primary organic matters are calculated with wind at a 10-m height, the particle diameter of sea salt aerosols, and chlorophyll-*a* concentration at the ocean surface (Gantt et al., 2011). The oceanic isoprene and monoterpene, which are precursor gases of organic matters, are emitted depending on the photosynthetically active radiation, diffuse attenuation coefficient at 490 nm, and the ocean surface chlorophyll-*a* concentration (Gantt et al., 2009).

The radiative transfer in MIROC6 is calculated by an updated version of the *k*-distribution scheme used in MIROC5 (Sekiguchi and Nakajima 2008). The single scattering parameters have been calculated and tabulated in advance, and liquid, ice, and five aerosol species can be treated in this updated version. Given the significant effect of crystal habit on a particle's optical characteristics (Baran, 2012), the assumption of ice particles habit has been updated from our previous simple assumption of sphere used in MIROC5 to a hexagonal solid column (Yang et al., 2013) in MIROC6. The upper limits of the mode radius of cloud particles have been extended from 32 μm to 0.2 mm for liquids and from 80 μm to 0.5 mm for ice. Therefore, the scheme can now handle the large-sized water particles (e.g., drizzle and rain) that have been shown to have significant radiative impacts (Waliser et al., 2011).

Following Hines (1997) and Watanabe et al. (2011), a non-orographic gravity wave parameterization is newly implemented into MIROC6 in order to represent realistic large-scale circulations and thermal structures in the stratosphere and mesosphere. Following Watanabe (2008), a present-day climatological source of non-orographic gravity waves, which is estimated using results

233 of a gravity wave-resolving version of MIROC-AGCM (Watanabe et al., 2008), is launched at the 70
234 hPa level in the extratropics, while an isotropic source of non-orographic gravity waves is launched at
235 the 650 hPa level in the tropics. Together with this parameterization, an orographic gravity wave
236 parameterization of McFarlane (1987) is also adopted as in MIROC5. In both the orographic and non-
237 orographic gravity wave parametrizations, wave source parameters at launch levels are tuned so that
238 the realistic seasonal progress of the middle atmosphere circulations, frequency of sudden
239 stratospheric warmings, and period and amplitude of the equatorial quasi-biennial oscillations (QBOs)
240 can be represented.
241
242 **2.2 Land surface component**
243 The land surface model is also basically the same as in MIROC5. Energy and water
244 exchanges between land and atmosphere are calculated, considering the physical and physiological
245 effects of vegetation with a single layer canopy, and the thermal and hydrological effects of snow and
246 soil respectively with a three-layers snow and a six-layers soil down to a 14 m depth. Sub-grid fractions
247 of land use and snow cover have also been considered. The timestep for the land surface model
248 integration is 1 hour in MIROC6 which is the same as in MIROC5. In addition to the standard package
249 in MIROC5, a few other physical parameterizations are implemented as described below.
250 A physically-based parameterization of sub-grid snow distribution (SSNOWD; Liston,
251 2004; Nitta et al., 2014) replaces the simple functional approach of snow water equivalent in
252 calculating sub-grid snow fractions in MIROC5 in order to improve seasonal cycle of snow cover. In
253 SSNOWD, the snow cover fraction is formulated for accumulation and ablation seasons separately.
254 For the ablation season, the snow cover fraction decreases based on the sub-grid distribution of the
255 snow water equivalent. A lognormal distribution function is assumed and the coefficient of variation
256 category is diagnosed from the standard deviation of the sub-grid topography, coldness index, and

257 vegetation type that is a proxy of surface winds. While the cold degree month was adopted for coldness
258 in the original SSNOWD, we decided instead to introduce the annually averaged temperature over the
259 latest 30 years using the time-relaxation method of Krinner et al. (2005), in which the timescale
260 parameter is set to 16 years. The temperature threshold for a category diagnosis is set to 0°C and 10°C.
261 In addition, a scheme representing a snow-fed wetland that takes into consideration sub-grid terrain
262 complexity (Nitta et al., 2017) is incorporated. The river routing model and lake module are the same
263 as those used in MIROC5, but the river network map is updated to keep the consistency to the new
264 land-sea mask (Yamazaki et al., 2009).
265
266 **2.3 Ocean and sea-ice component**
267 The ocean component of MIROC6 is basically the same as that used in MIROC5, but
268 several updates are implemented as described below. The warped bipolar horizontal coordinate system
269 in MIROC5 has been replaced by the tripolar coordinate system proposed by Murray (1996). Two
270 singular points in the bipolar region to the north of about 63°N are placed at (63°N, 60°E) in Canada
271 and (63°N, 120°W) in Siberia (Fig. 2). In the spherical coordinate portion to the south of 63°N, the
272 longitudinal grid spacing is 1° and the meridional grid spacing varies from about 0.5° near the equator
273 to 1° in the mid-latitudes. In the central Arctic Ocean where the bipole coordinate system is applied,
274 the grid spacings are about 60 km in zonal and 33 km in meridional, respectively. By introducing the
275 horizontal tripolar coordinate system, it is expected that theoretical westward propagation of the
276 oceanic baroclinic Rossby can be represented with less numerical dispersions because of agreement
277 of the coordinate system and the geographical coordinate system and that the horizontal resolutions in
278 the Arctic Ocean where the Rossby radius of deformation is relatively small are higher than in the case
279 where the bipolar warped coordinate system in MIROC5 is adopted. There are 62 vertical levels in a
280 hybrid σ-z coordinate system. The horizontal grid spacing in MIROC5 is nominally 1.4°, except for

281 the equatorial region and there are 49 vertical levels. The resolutions in MIROC6 are higher than in
282 MIROC5. In particular, 31 (23) of the 62 (49) vertical layers in MIROC6 (MIROC5) are within the
283 upper 500 m depth (Fig. 1b). The increased vertical layers in MIROC6 have been adopted in order to
284 better represent the equatorial thermocline and observed complex hydrography in the Arctic Ocean.
285 An increase in computational costs of the ocean component due to higher resolutions in MIROC6 is
286 suppressed by implementing a time-staggered scheme for the tracer and baroclinic momentum
287 equations (Griffies et al., 2005). Owing to the time-staggered scheme, the timestep for the ocean and
288 sea-ice components of MIROC6 is 20 minutes which is longer than that in MIROC5 (15 minutes).
289 The tracer advection scheme (Prather, 1986), the surface mixed layer parameterization
290 (Noh and Kim, 1999), and the parameterization for eddy isopycnal diffusion (Gent et al., 1995) used
291 in MIROC6 are the same as those used in MIROC5. Also as in MIROC5, the bottom boundary layer
292 parameterization of Nakano and Suginohara (2002) is introduced south (north) of 54°S (49°N) for
293 representing the down-sloping flow of dense waters. The constant parameters used in the above-
294 mentioned parameterizations are determined in the same manner as that of MIROC5, except for the
295 Arctic region. An empirical profile of background vertical diffusivity, which is proposed in Tsujino et
296 al. (2000), is modified above the 50 m depth to the north of 65°N. It is 1.0×10^{-6} m^2 s^{-1} in the uppermost
297 29 m and gradually increases to 1.0×10^{-5} m^2 s^{-1} at the 50 m depth. Additionally, the turbulent mixing
298 process in the surface mixed layer is changed so that there is no surface wave breaking and no resultant
299 near-surface mixing in regions covered by sea ice. The combination of the weak background vertical
300 diffusivity and suppression of turbulent mixing under the sea-ice contributes to better representations
301 of the surface stratification in the Arctic Ocean with little impact on the rest of the global oceans
302 (Komuro, 2014).
303 The sea-ice component in MIROC6 is almost the same as in MIROC5. A brief description,
304 along with some major parameters, is given here. Readers may refer to Komuro et al. (2012) and

Komuro and Suzuki (2013) for further details. A subgrid-scale sea-ice thickness distribution is incorporated by following Bitz et al. (2001). There are five ice categories (plus one additional category for open water), and the lower bounds of the ice thickness for these categories are set to 0.3, 0.6, 1, 2.5, and 5 m. The momentum equation for sea-ice dynamics is solved using elastic-viscous-plastic rheology (Hunke and Dukowicz, 1997). The strength of the ice per unit thickness and concentration is set at 2.0×10^4 N m^{-2}, and the ice–ocean drag coefficient is set to 0.02. The surface albedo for bare ice surface is 0.85 (0.65) for the visible (infrared) radiation. The surface albedo in snow-covered areas is 0.95 (0.80) when the surface temperature is lower than -5ºC for the visible (infrared) radiation, and it is 0.85 (0.65) when the temperature is 0ºC. Note that the albedo changes linearly between -5ºC and 0ºC. These parameter values listed here are the same as those listed in MIROC5.

2.4 Boundary conditions

A set of external forcing data recommended by the CMIP6 protocol are used. The historical solar irradiance spectra, greenhouse gas concentrations, anthropogenic aerosol emissions, and biomass burning emissions are given by Matthes et al. (2017), Meinshausen et al. (2017), Hoesly et al. (2018), and van Marle et al. (2017), respectively. The concentrations of greenhouse gases averaged globally and annually are given to MIROC6. Radiative forcing of stratospheric aerosols due to volcanic eruptions are computed by vertically integrating extinction coefficients for each radiation band, which are provided by Thomason et al. (2016), in the model layers above the tropopause. Three-dimensional atmospheric concentrations of historical ozone (O_3) are produced by the Chemistry-Climate Model Initiative (Hegglin et al., in preparation; the data are available at http://blogs.reading.ac.uk/ccmi/forcing-databases-in-support-of-cmip6/). Three dimensional concentrations of the OH radical, hydrogen peroxide (H_2O_2) and Nitrate (NO_3) are precalculated by a chemical atmospheric model of Sudo et al. (2002). As precursors of secondary organic aerosol,

329 emission data of terpenes and isoprene provided by the Global Emissions Inventory Activity (Guenther
330 et al., 1995) are normally used, although simulated emissions from the land ecosystem model of Ito
331 and Inatmoni (2012) are also used alternatively.

332 For specifying the soil types and area fractions of natural vegetation and crop-land on grids
333 of the land-surface component, the harmonized land-use dataset (Hurtt et al., in prep.), Center for
334 Sustainability and the Global Environment global potential vegetation dataset (Ramankutty and Foley,
335 1999), and the dataset provided by the International Satellite Land Surface Climatology Project
336 Initiative I (Sellers et al., 1996) are used. These datasets are also used in prescribing background
337 reflectance at the land surface. Leaf-area index data are prepared based on the Moderate Resolution
338 Imaging Spectroradiometer Leaf-area index products of Myneni et al. (2002).

339 The forcing dataset used for the preindustrial control simulation is basically composed of
340 the data for the year 1850, which are included in the above-mentioned historical dataset. The
341 stratospheric aerosols and solar irradiance in the preindustrial simulation are given as monthly
342 climatology averaged in 1850 – 2014 and in 1850 – 1873, respectively. The total solar irradiance is
343 about 1361 Wm^{-2}, and the global-mean concentrations of CO_2, methan (CH_4), and nitrous oxide (N_2O)
344 are 284.32 ppm, 808.25 ppb, and 273.02 ppb, respectively.

345

346 **2.5 Spin-up and tuning procedures**

347 Firstly, the stand-alone ocean component of MIROC6, which includes the sea-ice
348 processes, is integrated from the initial motionless state with the observed temperature and salinity
349 distribution of the Polar Science Center hydrographic climatology (Steele et al., 2001). Ocean model
350 coastline geometry and bottom bathymetry are specified based on horizontal interpolation of the land
351 and sea-floor dataset of ETOPO5 (National Geophysical Data Center, 1993). The ocean component is
352 spun-up for 1000 years by the monthly climatological surface fluxes of Röske (2006). An acceleration

353 method of Bryan (1984) is used in the spin-up stage in order to obtain a thermally and dynamically
354 quasi-steady state. After the spin-up, additional integration for 200 years is performed without the
355 acceleration method. By analyzing the last 50-yr-long data from the stand-alone ocean component, the
356 monthly climatology of typical variables (e.g., zonal-mean temperature and salinity in several basins,
357 volume transports across major straits and archipelagos, meridional overturning circulations, and sea-
358 ice distributions) are compared with observations. Once the configuration of the ocean component is
359 frozen, the land-sea distribution and land-sea area ratios on the atmospheric and land surface model
360 grids are determined according the coastline geometry of the ocean component, after which the
361 atmospheric and the land surface components are coupled with the ocean component. Surface
362 topography in the atmospheric and land surface component are also made using the ETOPO5 dataset.
363 Note that horizontal grid arrangement of the land surface model is exactly same as the atmospheric
364 component. The coupling interval among the sub-models is 1 hour. An initial condition of the ocean
365 component in MIROC6 is given by the stand-alone ocean experiment, and those of the atmosphere
366 and land are taken from an arbitrary year of the pre-industrial control run of MIROC5.

367 After coupling the sub-models, climate model tuning is done under the pre-industrial
368 boundary conditions. Conventionally, the climate models of our modeling community are retuned in
369 coupled modes after stand-alone sub-model tuning. This is because reproducibility of climatic-mean
370 state and internal climate variations is not necessarily guaranteed in climate models with the same
371 parameters determined in stand-alone sub-model tuning, which is particularly the case in the tropical
372 climate. In our tuning procedures described below, many of the 10-yr-long climate model runs are
373 conducted with different parameter values. There are numerous parameters associated with physical
374 parameterizations, whose upper/lower bounds are constrained by empirical or physical reasoning. The
375 main parameters used in our tuning procedures are chosen referring to a perturbed parameter ensemble
376 set made by Shiogama et al. (2012) in which parameter sensitivity to cloud-radiative processes is

examined. The impact of parameter tuning on the present climate is also discussed by Ogura et al (2017), focusing on the top-of-the-atmosphere (TOA) radiation and clouds. Any objective and optimal methods for parameter tuning are not used in our modeling group and the tuning procedures are like those in other climate modeling groups as summarized in Hourdin et al. (2017).

In the first model tuning step, climatology, seasonal progression, and internal climate variability in the tropical coupled system are tuned in order that departures from observations or reanalysis datasets are reduced. Here, it should be noted that representation of the tropical system in MIROC6 is sensitive to the parameters for convections and planetary boundary layer processes. Specifically, parameters of reference height for cumulus precipitation, efficiency of the cumulus entrainment of surrounding environment and maximum cumulus updraft velocity at the cumulus base are used to tune strength of the equatorial trade wind, climatological position and intensity of the Inter-Tropical Convergence Zone (ITCZ) and South Pacific Convergence Zone (SPCZ), and interannual variability of El-Niño/Southern Oscillation (ENSO). In particular, the parameter for the cumulus entrainment is known as a controlling factor of ENSO in MIROC5 (Watanabe et al., 2011). Summertime precipitation in the western tropical Pacific and characteristic of tropical intraseasonal oscillations are tuned by using the parameter for shallow convection describing the partitioning of turbulent kinetic energy between horizontal and vertical motions at the sub-cloud layer inversion. Next, the wintertime mid-latitude westerly jets and the stationary waves in the troposphere are tuned using the parameters of the orographic gravity wave drag and the hyper diffusion of momentum. The parameters of the hyper diffusion and the non-orographic gravity wave drag are also used when tuning stratospheric circulations of the polar vortex and QBO. Finally, the radiation budget at the TOA is tuned, primarily using the parameters for the auto-conversion process so that excess downward radiation can be minimized and maintained closer to 0.0 Wm^{-2}. The surface albedos for bare sea-ice and snow-covered sea-ice are set to higher values than in observations (see Section 2.3) in order to

avoid underestimating of the summertime sea-ice extent in the Arctic Ocean due to excess downward shortwave radiation in this region. In addition, parameter tuning for the total radiative forcing associated with aerosol-radiation and aerosol-cloud interactions is done. In order that the total radiative forcing can be closer to the estimate of -0.9 Wm^{-2} (IPCC, 2013; negative value indicates cooling) with an uncertainty range of -1.9 to -0.1 Wm^{-2}, parameters of cloud microphysics and the aerosol transport module, such as timescale for cloud droplet nucleation, in-cloud properties of aerosol removal by precipitation, and minimum threshold of number concentration of cloud droplets, are perturbed. To determine a suitable parameter set, several pairs of a present-day run under the anthropogenic aerosol emissions at the year 2000 and a pre-industrial run are conducted. A pair of the present and preindustrial runs has exactly the same parameters, and differences of tropospheric radiations between two runs are considered as anthropogenic radiative forcing. Note that MIROC6 in a coupled mode is used in this tuning procedure, and thus the sea surface temperature (SST) is not fixed. The estimated radiative forcing here is not strictly the same as the effective radiative forcing estimated in IPCC (2013). However, by the present tuning procedure, the global-mean surface air temperature (SAT) change after the mid-19th century is well reproduced in the historical runs by MIROC6 (details are discussed in Section 4). As above-mentioned, reproducibility of the global-mean SAT is not a tuning goal but is a typical metric which reflects results of the parameter tunings for individual processes of convections, dynamics, and radiative forcing.

After fixing the model parameters, the climate model is spun-up for 2000 years. During the first several hundred years, waters contained in the land surface are drained to the ocean via river runoff, which leads to a temporal weakening of the meridional overturning circulations in the ocean and a rising of the global-mean sea level. After the global hydrological cycle reaches to an equilibrium state, the strengths of the meridional overturning circulations recover and keep quasi steady state. The above-mentioned processes spend about 1000 years, after which an additional 1000-yr-long

integration is performed in order to obtain a thermally and dynamically quasi-steady ocean state.

Figure 3 shows the time series of the global-mean quantities after the spin-up. The labeled year in Fig. 3 indicates the elapsed year after the spin-up duration of 2000 years. Linear trend of the global-mean SAT is 9.5×10^{-3} K/100 yr and is much smaller than the observed value of about 0.62 K/100 yr in the twentieth century, indicating that there is no significant drift and the global-mean SAT is in a quasi-steady state. While the global-mean SST is in a quasi-steady state (linear trend of 7.0×10^{-3} K/100 yr), the global-mean ocean temperature shows a larger trend of 6.8×10^{-3} K/100 yr in the first 500 years than that of 1.3×10^{-3} K/100 yr in the later period. In the later sections, the 200-yr-long data between the 500-th and 699-th years are analyzed.

The trend of the global-mean ocean temperature in the later period suggests slight but continuous warming of the deep ocean. The radiation budget at the TOA is 1.1 Wm^{-2} downward on average (linear trend of 9.5×10^{-3} K/100 yr) and the net heat input at the sea surface is 0.32 Wm^{-2}. The deep ocean warming is explained by the net heat input. Note that there is about 0.78 Wm^{-2} inconsistency between the TOA radiation budget and the ocean heat uptake. This heat energy inconsistency is due to that internal energy associated with precipitation, water vapor and river runoff is not taken account in the atmospheric and land surface component in MIROC6 and that these waters with no temperature information implicitly set their temperature to the SST when they flow or fall into the ocean. Perpetual melting of the prescribed Antarctic ice-sheet with invariant ice thickness, which is occurred due to the warm SAT bias in the Antarctic region (details will be discussed in Section 3.1.3), is also a cause of the heat energy inconsistency.

3 Results of pre-industrial simulation

Representations of climatic-mean field and internal climate variability in MIROC6 are evaluated in comparison with MIROC5 and observations. The 200-yr-long data of the preindustrial

control simulation by MIROC5 are used. The observations and reanalysis datasets used in the comparison are listed in Table 1.

Here, the model climatology in the pre-industrial simulations is compared with observations in the recent decades. Because observations are obtained concurrently with the progress of the global-warming due to increasing anthropogenic radiative forcing, the model climate under the pre-industrial conditions may not be adequate for use when making comparisons with recent observations. However, the root-mean-squared (RMS) errors of typical variables (e.g., the global-mean SAT) in the climate models with respect to observations are much larger than the RMS differences between the model climatology in the pre-industrial simulation and those in the last 30-yr-long period in the historical simulations. Therefore, the era differences where climatology is defined are not significant concern in comparisons among the climate models and observations.

3.1 Climatology

3.1.1 Atmosphere and Land-surface

First, model systematic biases in radiations at the TOA are evaluated because they reflect model deficiencies in cloud-radiative processes that contribute to a large degree of uncertainty in climate modelling. Figure 4 shows annual-mean biases in radiative fluxes at the TOA in MIROC6 and MIROC5 with respect to the recent Clouds and the Earth's Radiant Energy System (CERES) estimate (Loeb et al., 2009; the data are available at https://ceres.larc.nasa.gov/). At the top-right of each panel, a global-mean (GM) value and a root-mean-squared error (RMSE) with respect to observations are written. In the present manuscript, RMSE is computed without model and observed global-mean quantities unless otherwise noted.

Persistent overestimates of net shortwave radiative flux and the sum of net shortwave and net longwave fluxes over low-latitude oceans in MIROC5 are significantly reduced in MIROC6.

473 Hereafter, net shortwave, longwave, and the sum of them are denoted as OSR, OLR and NET,
474 respectively, for simplicity. As described in Ogura et al. (2017), since parameter tuning cannot
475 eliminate the above-mentioned excess upward radiations, it is suggested that implementing a shallow
476 convective parameterization is required in order to reduce the biases. Figure 5 shows annual-mean
477 moistening rates associated with deep and shallow convections at the 850 hPa pressure level in
478 MIROC6. Moistening due to shallow convections occurs mainly over the low-latitude oceans,
479 especially the eastern subtropical Pacific and the western Atlantic and Indian oceans. These active
480 regions of shallow convections occur separately from regions with active deep convections in the
481 western tropical Pacific and the ITCZ. The clear separation of the two convection types is consistent
482 with satellite-based observations (Williams and Tselioudis, 2007). Owing to the shallow convective
483 process that mixes the humid air in the planetary boundary layer with the dry air in the free troposphere,
484 low-level cloud cover over the low-latitude oceans is better represented in MIROC6 than in MIROC5.
485 Figure 6 shows annual-mean biases in cloud covers with respect to the International Satellite Cloud
486 Climatology Project (ISCCP; Rosso et al., 1996; Zhang et al., 2004; the data are available at
487 https://isccp.giss.nasa.gov/). Overestimate of low-level cloud cover over the low-latitude oceans in
488 MIROC5 (Fig. 6b) is apparently reduced in MIROC6 (Fig. 6a), which results in the smaller biases in
489 NET and OSR biases (Fig. 4). RMS error in low-level cloud cover in MIROC6 is 9% lower than that
490 in MIROC5.

491 OSR in the mid-latitudes are also better represented in MIROC6 than in MIROC5. Zonally
492 distributed downward OSR bias in MIROC5 is reduced or becomes a relatively small upward bias in
493 MIROC6 (Figs. 4cd). This difference in the OSR bias is commonly found in both hemispheres. Cloud
494 covers at middle and high levels are larger in MIROC6 over the subarctic North Pacific, North Atlantic,
495 and the Southern Ocean (Figs. 6c-f), while low-level cloud cover over the same regions is smaller in
496 MIROC6 than in MIROC5 over the same regions (Figs. 6ab). The smaller low-level cloud cover in

MIROC6 is inconsistent with the larger upward OSR bias in MIROC6. The wintertime mid-latitude westerlies are stronger and are located more poleward in MIROC6 than in MIROC5. Correspondingly, activity of sub-weekly disturbances in the mid-latitudes is strengthened in MIROC6 (details are described later). These differences in the mid-latitude atmospheric circulations between MIROC6 and MIROC5 lead to an enhanced poleward moist air transport from the subtropics to the subarctic region, which could result in an increase in the mid- and high-level cloud covers in MIROC6, as reported in previous modeling studies (e.g., Bodas-Salcedo et al., 2012; Williams et al., 2013). Consequently, the downward OSR bias in the mid-latitudes is smaller in MIROC6 than in MIROC5. In polar regions, both biases in OSR and NET remain the same as in MIROC5.

Systematic bias in the outgoing longwave radiative flux (hereafter, OLR) is worse in MIROC6 than in MIROC5 because MIROC6 tends to underestimate OLR over almost the entire global domain, except for Antarctica (Figs. 4ef). The global-mean of the high-level cloud cover in MIROC6 is larger than in MIROC5 by 0.04 (Figs. 6ef), which is consistent with the smaller OLR in MIROC6. The increased moisture transport due to the strengthening of the westerlies and sub-weekly disturbances can partly explain the increase in the mid-latitude high-level clouds in MIROC6, but high-level cloud cover is also larger in the low-latitudes. Hirota et al. (2018) reported that moistening of the free troposphere due to shallow convections creates favorable conditions for atmospheric instabilities that leads to the resultant activation of deep convections in the low-latitudes. Such processes may contribute to the inferior representation of OLR in MIROC6.

Next, we will discuss on the global budget of the radiative fluxes and the RMS errors between models and observations. Note that only deviations from the global means are considered when calculating RMS errors. As written on the upper right of panels in Fig. 4ab, the global-mean (RMS errors) NETs are -1.11 (12.7) Wm^{-2} in MIROC6 and -0.98 (15.9) Wm^{-2} in MIROC5, respectively, and these values are consistent with the observed value of -0.81 Wm^{-2} (CERES; Loeb et al, 2009).

521 However, the observed value is estimated in the present-day condition. Ideally, the model value in the
522 preindustrial condition should be 0 Wm^{-2} and is in the marginally acceptable range. If NET is divided
523 into OSR and OLR, so-called error compensation becomes apparent. The global means of OSR (OLR)
524 are -231.3 (230.2) Wm^{-2} in MIROC6 and -237.6 (236.6) Wm^{-2} in MIROC5, respectively (Figs. 4c-f).
525 The observed global-means of OSR and OLR are -240.5 Wm^{-2} and 239.7 Wm^{-2}. Biases in the global-
526 mean OSR (OLR) with respect to observations are 9.2 (-9.5) Wm^{-2} in MIROC6 and 2.9 (-3.1) Wm^{-2}
527 in MIROC5, respectively. Thus, the global-mean OSR and OLR in MIROC6 are worse than those in
528 MIROC5. Further division of OSR and OLR into cloud-radiative forcing and clear-sky shortwave
529 (longwave) radiative components shows that shortwave cloud-radiative forcing is dominant on the
530 biases in radiative fluxes. The biases in the global-mean shortwave (longwave) cloud-radiative forcing
531 with respect to observations are 12.0 (6.7) Wm^{-2} in MIROC6 and -4.0 (-0.2) Wm^{-2} in MIROC5,
532 respectively.

533 The global radiation budget in MIROC6 is inferior to that in MIROC5, while
534 reproducibility of climatic means of typical model variables, other than radiative fluxes, and internal
535 variations are better simulated in MIROC6 (details are shown later). As described in Section 2.5, the
536 intensive tuning by perturbing model parameters is done focusing on reproducibility of climatic means,
537 internal variations, and radiative forcing due to anthropogenic aerosols. During this procedure, the
538 global radiation budget is traded-off. On the other hand, RMS errors in NET, OSR, and OLR are 12.7,
539 16.2, and 6.3 Wm^{-2} in MIROC6 and 15.9, 18.9, and 6.8 Wm^{-2} in MIROC5, respectively, thereby
540 indicating that the errors in MIROC6 have been reduced by 7% to 20 %. This is also the case for
541 shortwave and longwave cloud radiative forcings, where the corresponding errors have been reduced
542 by 17% and 13 %, respectively. Taken toghther, these results show that the spatial patterns of the
543 radiative fluxes are better simulated in MIROC6 than in MIROC5.

544 The improvement in spatial radiation patterns, especially in low-latitude OSR, is explained

545 primarily by the implementation of shallow convective processes, which results in a moister free
546 troposphere in MIROC6 than in MIROC5. Figures 7ab show zonal-mean biases in annual-mean
547 specific humidity with respect to the European Centre for Medium-Range Weather Forecast interim
548 reanalysis (ERA-I; Dee et al., 2011; the data are available at
549 https://www.ecmwf.int/en/forecasts/datasets/archive-datasets/reanalysis-datasets/era-interim). Dry
550 bias in 30ºS–30ºN, which occurs persistently in MIROC5, are largely reduced in MIROC6 owing to
551 vertical mixing at the interface of the planetary boundary layer and the free troposphere. On the other
552 hand, moist bias below the 600 hPa pressure level in the mid-latitudes is somewhat worse in MIROC6
553 than in MIROC5. Shallow convections also contribute to the improvement of precipitations in the low
554 latitudes. Figure 8 shows global maps for climatological precipitation in boreal winter (December–
555 February) and summer (June–August). The second version of the Global Precipitation Climatology
556 Project (GPCP; the data are available at https://precip.gsfc.nasa.gov/) Monthly Precipitation Analysis
557 (Adler et al., 2003) is used for the observations. While MIROC5 suffers from underestimate of
558 summertime precipitation over the western tropical Pacific, the underestimate is largely reduced in
559 MIROC6 (Figs. 8df). The increase of precipitations is associated with deep convections because the
560 moister free troposphere in MIROC6 is more favorable for the occurrence of deep convections (Hirota
561 et al., 2018). On the other hand, model representation of the precipitation in MIROC6 is not necessarily
562 alleviated other than the western tropical Pacific. For example, the overestimate of wintertime
563 precipitation over the Indian Ocean and the mid-latitude North Pacific is worse in MIROC6 than in
564 MIROC5.

565 Zonal-mean biases in annual-mean air temperature and zonal wind velocity are also better
566 represented in MIROC6 than in MIROC5 (Figs. 7c-f). The upper stratospheric warm bias in 50ºS–
567 50ºN in MIROC5 is significantly reduced in MIROC6. The model top of MIROC6 is located at the
568 0.004 hPa pressure level and there are 42 vertical layers above the 50 hPa pressure level, while the

model top of MIROC5 is placed at the 3 hPa pressure level. As a result, there are significant differences in stratospheric circulations between the models. As shown in the annual-mean mass stream function calculated using zonal-mean meridional winds (Fig. 9), an upward wind continuing from the low-latitude troposphere to the stratosphere is stronger in MIROC6 than in MIROC5. It is considered that an increased upward advection of the temperature minimum around the tropopause in 30ºS–30ºN may lead to reduction of warm temperature bias in the stratosphere which is significant in MIROC5. Correspondingly, the stratospheric westerly bias in low latitudes of MIROC5 is also considerably alleviated in MIROC6. Note that the atmospheric O_3 concentration data used in MIROC5 is different from those in MIROC6, and the concentration in the stratosphere is higher than the data used in MIROC6. About 25% of the above-mentioned reduction in the stratospheric warm biases is explained by the smaller absorption of shortwave radiation by O_3. Note that the zonal-mean temperature bias in Fig. 7c is smaller when the climatological-mean temperature from 1980 to 2009 in a historical simulation are evaluated against observations because of the known stratospheric cooling with increased greenhouse gases and reduced O_3 concentrations.

The zonal-means of the air temperature and zonal wind in MIROC6 are also better simulated in the mid- and high latitudes. A pair of easterly and westerly biases in MIROC5, which is in the troposphere of the Northern Hemisphere, is associated with a weaker mid-latitude westerly jet and its southward shift with respect to observations. The pair of the biases is reduced in MIROC6, thereby suggesting that a strengthening and northward shift of the westerly jet occurs in MIROC6. Indeed, as shown in the upper panels of Fig. 10, the meridional contrast of high and low biases in the 500 hPa pressure level (Z500) along the wintertime westerly jet is weaker in MIROC6 than in MIROC5. The latitudes with the maximal meridional gradient of Z500 are located further northward in MIROC6 than in MIROC5, especially over the North Atlantic. Correspondingly, wintertime storm track activity (STA), which is defined as an 8-day-high-pass-filtered eddy meridional temperature flux

593 at the 850 hPa pressure level, is stronger over the North Pacific and Atlantic in MIROC6 than in
594 MIROC5 (see upper panels of Fig. 11) and is accompanied by an associated increase in precipitation,
595 especially in the North Pacific (Figs. 8ce). In the stratosphere above the 10 hPa pressure level, the
596 polar night jet is reasonably captured in MIROC6, although the westerly is somewhat overestimated
597 in 30ºN–60ºN. Also, in the Southern Hemisphere, representation of the tropospheric westerly and the
598 polar night jets are better in MIROC6 than in MIROC5, and the easterly bias centered at 60ºS in the
599 troposphere is clearly reduced in MIROC6. Although causality is unclear, the warm air temperature
600 bias above the tropopause to the south of 60ºS is smaller in MIROC6 than in MIROC5.

601 The enhanced wintertime STA in MIROC6 leads to a strengthening of the Ferrel circulation
602 in the Northern Hemisphere and a broadening of its meridional width. As shown in Fig. 9, the northern
603 edge of the Ferrel cell is located further northward in MIROC6 than in MIROC5. Because the Ferrel
604 cell is a thermally indirect circulation driven primarily by eddy temperature and momentum fluxes,
605 the stronger STA in MIROC6 possibly causes the Ferrel cell differences between the two models.
606 Associated with the northward extension of the Ferrel cell, the upward wind between the Ferrel cell
607 and the polar cell centered at 65ºN is stronger in MIROC6 than in MIROC5 and the meridional width
608 of the polar cell is smaller. Also, in the Southern Hemisphere, the upward wind around 60ºS at the
609 southern edge of the Ferrel cell is stronger in MIROC6 than in MIROC5. Correspondingly, high sea
610 level pressure (SLP) biases in polar region in MIROC5 are significantly reduced in MIROC6 (figures
611 are omitted) and RMS errors with respect to observations (ERA-I) are decreased by 30 %. Meanwhile,
612 in the stratosphere, anti-clockwise (clockwise) circulations to the north (south) of 50ºN (S) are stronger
613 and extend further upward in MIROC6 than in MIROC5. These circulations seem to continue from
614 the troposphere into the stratosphere, thereby implying that more active troposphere-stratosphere
615 interactions associated with wave-coupling exist in MIROC6. Further details will be described later,
616 focusing on the occurrence of the sudden stratospheric warmings.

Parameterizations of SSNOWD (Liston, 2004; Nitta et al., 2014) and a wetland due to snow-melting water have been newly implemented into MIROC6 (Nitta et al., 2017). In comparison of MIROC6 with MIROC5, it can be seen that the former parameterization brings about significant improvement in the Northern Hemisphere snow cover fractions from the early to the late winter (Fig. 12). Compared with observations of the Northern Hemisphere EASE-Grid 2.0 (Brodzik and Armstrong, 2013; the data are available at https://nsidc.org/data/ease/), the distribution of the snow cover fractions is more realistic in MIROC6 than MIROC5, especially where and when the snow water equivalent is relatively small (e.g., mid- and high latitudes in November, over Siberia in February). Note that no clear improvement is found in May. This is because the newly implemented SSNOWD represents hysteresis in the snow water equivalent-snow cover fraction relationship in both the accumulation and ablation seasons. MIROC6 underestimates the snow cover fraction in the partially snow-covered regions and overestimates it on the Tibetan plateau and in some parts of China. We note that meteorological (e.g., precipitation or temperature) phenomena might affect these biases, but further investigation will be necessary to identify their causes. Nevertheless, in spite of those discrepancies, it can be said that the seasonal changes of the snow cover fraction are better simulated in MIROC6 than in MIROC5 (Fig. 12j).

3.1.2 Ocean

Next, we evaluate the climatological fields of the ocean hydrographic structure, meridional overturning circulations (MOCs), and sea-ice distribution. The zonal-mean potential temperature and salinity are displayed in Figs. 13 and 14, respectively. Both MIROC6 and MIROC5 capture the general features of the observed climatological hydrography (ProjD; Ishii et al., 2003). However, the potential temperatures in the deep and bottom layers to the south of 60ºS in the two models are warmer than observations because of insufficient formation and sinking of cold and dense water due to intense

surface cooling around Antarctica (Figs. 13a-c and 14a-c). Such warm temperature bias associated with deep water formation is also found in northern high latitudes of the Atlantic sector (Figs. 13a-c). By horizontal advection of the warm temperature biases associated with the Pacific and Atlantic MOCs, the model temperatures in deep layers apart from polar regions are also warmer than in observations. The warm potential temperature bias in the deep layer is worse in MIROC6 than in MIROC5 in both of the Atlantic and Pacific sectors and the warm bias influences the subsurface and the intermediate layers above the 3000 m depth, which might be attributed to the excess ocean heat uptake and longer integration time in MIROC6 than in MIROC5 (the spinup duration of MIROC6 is 2000 years and that of MIROC5 is about 1000 years, repectively). Also the low salinity bias below the 2000 m depth is worse in MIROC6 than in MIROC5, especially in the Pacific sector (Figs. 14ef). This worsening can be explained the excess supply of the freshwater in the Southern Ocean and weaker northward intrusion of the less saline water in MIROC6.

In the Arctic Ocean, the halocline above the upper 500 m depth is sharper and more realistic in MIROC6 than in MIROC5 and the high salinity bias below the 500 m depth in MIROC5 is alleviated in MIROC6 (Figs. 13ef) because, as described in Section 2.3, there are many more vertical levels in the surface and subsurface layers of MIROC6. In addition, vertical diffusivity in the Arctic Ocean is set to smaller values in MIROC6 than in MIROC5, and the turbulent kinetic energy input induced by surface wave breaking, as a function of the sea-ice concentration in each grid cell, is reduced in MIROC6, as shown in Komuro (2014). In the North Pacific, the southward intrusion of North Pacific Intermediate Water (NPIW) around the 1000 m depth retreats northward in MIROC6. Strong tide-induced vertical mixing of sea water is observed along the Kuril Islands (e.g., Katsumata et al., 2004). The locally enhanced tide-induced mixing is known to reinforce the southward intrusion of the Oyashio and associated water mass transport from the subarctic to subtropical North Pacific, and to feed the salinity minimum of NPIW (Nakamura et al., 2004; Tatebe and Yasuda, 2004). Hence,

665 NPIW reproducibility is better in MIROC5 where enhanced tidal mixing is considered than in
666 MIROC6. Because we encountered significant uncertainty in implementing the tidal mixing, we
667 decided to quit implementing it in developing phase of MIROC6, at the expense of NPIW
668 reproducibility.

669 The annual-mean potential temperature and zonal currents along the equator in MIROC6
670 are better simulated in MIROC6 than in MIROC5 (Fig. 15). Relatively cold water below the equatorial
671 thermocline is upwelled in MIROC6, especially in the eastern tropical Pacific, which leads to a
672 strengthening of the vertical temperature gradient across the thermocline. The eastward speed of the
673 Equatorial Undercurrent in MIROC6 is over 80 cm s^{-1}, and is closer to the products of Simple Ocean
674 Data Assimilation (SODA; Carton and Giese, 2008; the data are available at
675 http://www.atmos.umd.edu/~lchen/SODA3.3_Description.html) than in MIROC5. These
676 improvements are mainly attributed to the higher vertical resolution of MIROC6 in the surface and
677 subsurface layers. However, the thermocline depths in the western tropical Pacific are still larger in
678 the models than in observations and are attributed to the stronger trade winds in the models. When
679 both of MIROC6 and MIROC5 are executed as stand-alone AGCMs with the prescribed SST obtained
680 from observations, the overestimate of the equatorial trade winds also appears due to overestimate of
681 the upward winds over the maritime continent associated with deep cumulus convection and the
682 resultant strengthening of the Walker circulation over the equatorial Pacific. Better parameterizing
683 deep cumulus convection in the models could be required for better representation of the equatorial
684 trade winds and thus oceanic states.

685 Figure 16 displays annual-mean Atlantic and Pacific MOCs. In the Atlantic, two deep
686 circulation cells associated with North Atlantic Deep Water (NADW; upper cell) and Antarctic Bottom
687 Water (AABW, lower cell) are found in both of the models. NADW transport across 26.5ºN is 17.2
688 (17.6) Sv (1 Sv = 10^6 m^3 s^{-1}) in MIROC6 (MIROC5). These values are consistent with the

689 observational estimate of 17.2 Sv (McCarthy et al., 2015). RMS amplitudes of NADW transport are
690 about 0.9 Sv in MIROC6 and 1.1 Sv in MIROC5 on longer-than-interannual timescales, respectively.
691 These are smaller than the observed amplitude of 1.6 Sv in 2005–2014. Because observations include
692 the weakening trend of the Atlantic MOC due to the global warming, they can be larger than the model
693 variability under the preindustrial conditions. In the Pacific Ocean, both the models have the deep
694 circulation associated with Circumpolar Deep Water (CDW), but the northward transport of CDW
695 across 10ºS is 8.6 Sv in MIROC6, which is slightly larger than 7.5 Sv of MIROC5. Although these
696 models values are somewhat smaller than observations, they are within the uncertainty range of
697 observations (Talley et al., 2003; Kawabe and Fujio, 2010).

698 Northern Hemisphere sea-ice concentrations are shown in Fig. 17. Here, it can be seen that
699 both the March and September sea-ice distributions in MIROC6 resemble the satellite-based
700 observation (SSM/I; Cavarieli et al., 1991; the data are available at https://nsidc.org/). In general, the
701 spatial patterns of the models resemble the observations. Sea-ice areas in March (September) are 12.4
702 (6.1), 13.0 (6.9), and 14.9 (5.7) Million km^2 in MIROC6, MIROC5, and observations, respectively.
703 The model estimates are smaller (larger) in March (September) than in observations. The
704 underestimate in March is still found in MIROC6 and is attributed to the underestimate of sea-ice area
705 in the Sea of Okhotsk and the Gulf of St. Lawrence, even though the sea-ice area in the former region
706 is better simulated in MIROC6 than in MIROC5. Meanwhile, the eastward retreat of the sea-ice in the
707 Barents Sea is better represented in MIROC6 than in MIROC5. The overestimates in September in the
708 models are due to that the model climatology is defined under the pre-industrial conditions while
709 observations are taken in present-day conditions of 1980–2009, where a rapid decreasing trend of
710 summertime sea-ice area (including a few events of drastic decreases) is on-going (e.g., Comiso et al.,
711 2008). Note that the model September sea-ice area in 1980–2009 of historical simulations is smaller
712 than the observations and the sea-ice area does not show year-to-year drastic sea-ice decrease with

713 comparable amplitude with observations. The underestimate of the mean September sea-ice area in
714 MIROC6 might be attributed to slightly rapid warming of the Arctic climate in MIROC6 than in
715 observations. On the other hand, the modeled sea-ice areas in the Southern Ocean are unrealistically
716 smaller than in observations. Southern Hemisphere sea-ice areas in March (September) are 0.1 (3.4),
717 0.2 (5.2), and 5.0 (18.4) Million km^2 in MIROC6, MIROC5, and observations, respectively. Since
718 there are no significant differences between the two models, the spatial maps for the sea-ice area in
719 the southern hemisphere are omitted.

720 Figure 18 shows the global maps of annual-mean sea level height relative to the geoid. The
721 absolute dynamic height data provided by Archiving, Validation, and Interpretation of Satellite
722 Oceanographic (AVISO; Rio et al. 2014) data are used as observed sea level height (the data are
723 available at https://www.aviso.altimetry.fr/en/home.html). Overall oceanic gyre structures in the two
724 models are consistent with observations. Although representation of the gyres in MIROC6 remain
725 generally the same as in MIROC5, there are a few improvements in the North Pacific and the North
726 Atlantic. The mid-latitude westerly in MIROC6 is stronger and is shifted further northward than in
727 MIROC5 (Fig. 10), which results in the strengthening of the subtropical gyres, northward shifts of the
728 western boundary currents, and their extensions. In particular, the current speed of the Gulf Stream
729 and the North Atlantic Current are faster in MIROC6 than in MIROC5, and the contours emanating
730 from the North Atlantic reach the Barents Sea in MIROC6. A corresponding increase in warm water
731 transport from the North Atlantic to the Barents Sea leads to sea-ice melting and an eastward retreat
732 of the wintertime sea-ice there in MIROC6 (Figs. 17a-c). An improvement in MIROC6 is also found
733 in the Subtropical Countercurrent (STCC) in the North Pacific along 20ºN. As reported in Kubokawa
734 and Inui (1999), the low potential vorticity water associated with a wintertime mixed layer deepening
735 in the western boundary current region is transported southward in the subsurface layer and it pushes
736 up isopycnal surfaces around 25ºN. Thus, the eastward-flowing STCC is induced around 25ºN.

737 Although both of the models show the wintertime mixed layer deepening, the ocean stratification along
738 160ºE is weaker in MIROC6 than in MIROC5 (not shown). This suggests that the isopycnal advection
739 of low potential vorticity water in MIROC6 is more realistic than in MIROC5.
740
741 **3.1.3 Discussions on model climatological biases**
742 We have evaluated the simulated climatology in MIROC6 in comparison with MIROC5
743 and observations. The model climatology in MIROC6 shows certain improvements in simulating
744 radiations, atmospheric and oceanic circulations, and the snow cover fractions in the Northern
745 Hemisphere. In Fig. 19, we display the model biases in annual-mean SAT and SST (Fig. 19) because
746 these are typical variables that reflect errors in individual processes in the climate system. The global-
747 mean of SAT (SST) is 15.2 (18.1) ºC in MIROC6, 14.6 (18.0) ºC in MIROC5, and 14.4 (18.1) ºC in
748 observations. The modeled global-mean SATs and SSTs are generally consistent with observations.
749 However, since the observed (model) value is estimated in the present-day (preindustrial) condition,
750 the model global-mean SATs and SSTs are overestimated. Here, it should be noted that while the
751 spatial patterns of the SAT and SST biases in MIROC6 resemble those in MIROC5, there are several
752 improvements. For example, cold SAT bias in MIROC5 extending from the Barents Sea to Eurasia is
753 significantly smaller in MIROC6, possibly owing to the increase in warm water transport by the North
754 Atlantic Current and the resultant eastward retreat of the sea ice in the Barents Sea (Figs. 17 and 18).
755 Warm SAT and SST biases along the west coast of the North America are smaller in MIROC6 than in
756 MIROC5. The reason is that an increase of southeastward Ekman transport in the eastern subarctic
757 North Pacific due to the strengthening of the mid-latitude westerly jet (Fig. 10) and the Aleutian low
758 tend to cancel out the relatively warm water supply from the subtropics to the subarctic region by the
759 surface geostrophic current. Although it is not clear from Fig. 19, the SAT and SST in the subtropical
760 North Pacific around 20ºN are warmer by 2 K in MIROC6 than in MIROC5. Also in the Atlantic, the

761 SAT in the western tropics is warmer in MIROC6. These warmer surface temperatures in MIROC6
762 indicates a reduction of the cold SAT and SST biases that can be alleviated by an increase in the
763 downward OSR in MIROC6 due to the implementation of a shallow convective parameterization (Fig.
764 4), and by an increase in eastward transport of the warm pool temperature associated with the stronger
765 STCC in MIROC6 (Fig. 18).

766 On the other hand, the warm SAT and SST biases in the Southern Ocean and the warm
767 SAT bias in Middle East and the Mediterranean are worse in MIROC6 than in MIROC5. Consequently,
768 the RMS error in SAT is larger in MIROC6 (2.4 K) than in MIROC5 (2.2 K). The former is due
769 essentially to the underestimate of mid-level cloud covers, excess downward OSR, and the resultant
770 underestimate of the sea ice in the Southern Ocean. Such bias commonly occurs in many of climate
771 models and is normally attributed to errors in cloud radiative processes (e.g., Bodas-Salcedo et al.,
772 2012; Williams et al., 2013). In addition, poor representations of mixed layer depths and open ocean
773 deep convections due to the lack of mesoscale processes in the Antarctic Circumpolar Current are
774 causes of the warm bias (Olbers et al., 2004; Downes and Hogg, 2013). The latter warm bias, seen in
775 Middle East around the Mediterranean, can be explained by a tendency to underestimate the radiative
776 forcing of aerosol-radiation interactions due to underestimate of dust emissions from the Sahara Desert
777 in MIROC6 (not shown).

778

779 **3.2 Internal climate variations**

780 **3.2.1 Madden-Julian oscillation and East Asian Monsoon**

781 In this section, we will evaluate the reproducibility of internal climate variations in
782 MIROC6 in comparison with MIROC5 and observations, beginning with an examination of the
783 equatorial waves in the atmosphere. Zonal wavenumber–frequency power spectra normalized by
784 background spectra for the symmetric and antisymmetric components of OLR are calculated following

785 Wheeler and Kiladis (1999) and are shown in Fig. 20. The daily-mean OLR data derived from the
786 Advanced Very High-Resolution Radiometer (AVHRR) of the National Oceanic and Atmospheric
787 Administration (NOAA) satellites (Liebmann and Smith, 1996; the data are available at
788 https://www.esrl.noaa.gov/psd/data/gridded/data.interp_OLR.html) are used for observational
789 references. The signals corresponding to the Madden-Julian oscillation (MJO), equatorial Kelvin (EK),
790 equatorial Rossby (ER), eastward inertia-gravity (n=1 EIG), and westward inertia-gravity (WIG)
791 waves in the symmetric component and mixed Rossby-gravity (MRG) and eastward inertia-gravity
792 (n=0 EIG) waves in the antisymmetric component stand out from the background spectra in
793 observations. MIROC5 qualitatively reproduces these spectral maxima of the symmetric MJO, EK,
794 and ER qualitatively, while the amplitudes of the MJO and the EK are underestimated. These
795 underestimates are partially mitigated in MIROC6. The power summed over the eastward
796 wavenumber 1–3 and periods of 30–60 days corresponding to the MJO are 20% larger in MIROC6
797 than in MIROC5. Furthermore, some additional analyses indicate that many aspects of the MJO,
798 including its eastward propagation over the western tropical Pacific, are improved in MIROC6. Those
799 improvements are primarily associated with the implementation of the shallow convective scheme that
800 moistens the lower troposphere. The results of these additional analyses, along with some sensitivity
801 experiments, are described in a separate paper (Hirota et al., 2018). The EIG and WIG in the symmetric
802 component and the MRG and the EIG in the antisymmetric component are missing in both MIROC6
803 and MIROC5.

804 Figure 21 shows the June–August (JJA) climatology of precipitation and circulations in
805 the East Asia. As shown in observations (ERA-I; Fig. 21a), the East Asian summer monsoon (EASM)
806 is characterized by the monsoon low over the warmer Eurasian continent and the subtropical high over
807 the colder Pacific Ocean (e.g., Ninomiya and Akiyama, 1992). The southwesterly between these
808 pressure systems transports moist air to the mid-latitudes forming a rainband called *Baiu* in Japanese.

809 The general circulation pattern of the EASM and the rainband are well simulated in both MIROC6
810 and MIROC5. It should be noted that one of major deficiencies in MIROC5, the underestimate of the
811 precipitation around the Philippines, has been largely alleviated in MIROC6. This improvement is,
812 again, associated with the moistening of the lower troposphere by shallow convective processes.
813 Interannual EASM variabilities are examined using an empirical orthogonal function (EOF) analysis
814 of vorticity at the 850 hPa pressure level over [100°E–150°E, 0°N–60°N] following Kosaka and
815 Nakamura (2010). The regressions of precipitation and 850hPa vorticity with respect to the time series
816 of the first mode (EOF1) are shown in the lower panels of Fig. 21. In observations, precipitation and
817 vorticity anomalies show a tripolar pattern with centers located around the Philippines, Japan, and the
818 Sea of Okhotsk (Hirota and Takahashi, 2012). The anomalies around the Philippines and Japan
819 correspond to the so-called Pacific-Japan pattern (Nitta et al., 1987). The southwest-northeast
820 orientation of the wave-like anomalies is better simulated in MIROC6 than in MIROC5.
821 Figure 22 shows the wintertime (December–February) climatology of circulations and the
822 STA in the East Asia. The East Asian winter monsoon (EAWM) is characterized by northwesterly
823 between the Siberian high and the Aleutian low in observations (ERA-I; e.g. Zhang et al., 1997). The
824 monsoon northwesterly advects cold air to East Asia, enhancing the meridional temperature gradients
825 and strengthening the subtropical jet around Japan. The jet's strength influences synoptic wave
826 activities in the storm track. MIROC5 captures the circulation pattern, but significantly underestimates
827 the STA. The STA in MIROC6 is better simulated than in MIROC5, but it is still smaller than in
828 observations. Interannual variability of the EAWM is also better represented in MIROC6 than in
829 MIROC5. The dominant variability of the monsoon northwesterly is extracted as the EOF1 of the
830 meridional wind at the 850 hPa pressure level over the region [30°N–60°N, 120°E–150°E]. In
831 observations, the regressions with respect to the time series of the EOF1 show stronger northwesterly
832 accompanied with suppressed STA, which is consistent with previous studies (Fig. 22d; e.g.,

833 Nakamura, 1992). This relationship between the circulations and the STA can be found in MIROC6
834 but not in MIROC5 (Figs. 22e, f). The explained variance of the EOF1 is 46.0% in observations, 37.1%
835 in MIROC5, and 47.1% in MIROC6, suggesting that the amplitude of this variability in MIROC6 is
836 consistent with observations.
837
838 **3.2.2 Stratospheric circulations**
839 A few of the major changes in the model setting from MIROC5 to MIROC6 are higher
840 vertical resolution and higher model top altitude in MIROC6, namely, representation of the
841 stratospheric circulations. Here, we examine representation of the Quasi-Biennial Oscillations (QBOs)
842 in MIROC6. Figure 23 shows the time-height cross-sections of the monthly mean, zonal-mean zonal
843 wind over the equator for observations (ERA-I) and MIROC6. In this figure, an obvious QBO with
844 mean period of approximately 22 months can be seen in MIROC6. The mean period is slightly shorter
845 than that of ~28 months in observations, and the simulated QBO period varies slightly from cycle to
846 cycle. The maximum speed of the easterly at the 20 hPa pressure level is approximately -25 m s^{-1} in
847 MIROC6 and that of the westerly is 15 m s^{-1}. On the other hand, the observed maximum wind speeds
848 are -35 m s^{-1} for the easterly and 20 m s^{-1} westerly, respectively. The simulated QBO has somewhat
849 weaker amplitude in MIROC6 than observations, but the same east-west phase asymmetry. The QBO
850 in the MIROC6 shifts upward compared with that in observations, and the simulated amplitude is
851 larger above the 5 hPa pressure level and smaller in the lower stratosphere. The simulated downward
852 propagation of the westerly shear zones of zonal wind ($\partial\bar{u}/\partial z > 0$, where z is the altitude) is faster
853 than the downward propagation of easterly shear zones ($\partial\bar{u}/\partial z$) < 0, which agrees with observations.
854 The QBOs in MIROC6 are qualitatively similar to that represented in the MIROC-ESM, which is an
855 Earth system model with a similar vertical resolution that participated in the CMIP5 (Watanabe et al.,
856 2011). Note that nothing resembling a realistic QBO was simulated in the previous low-top version

MIROC5, which only has a few vertical layers in the stratosphere.

Recently, Yoo and Son (2016) found that the observed MJO amplitude in the boreal winter is stronger than normal during the QBO easterly phase at the 50 hPa pressure level. They also showed that the QBO exerted greater influence on the MJO than did ENSO. Marshall et al. (2016) pointed out the improvement in forecast skill during the easterly phase of the QBO and indicated that the QBO could be a potential source of the MJO predictability. MIROC6 successfully simulates both the MJO and QBO in a way consistent with observations, as mentioned above, but correlations between the QBO and MJO are insignificant. One possible reason is smaller amplitude of the simulated QBO in the lowermost stratosphere. The QBO contribution to tropical temperature variation at the 100 hPa pressure level is ~0.1 K in the MIROC6, which is much smaller than the observed value of ~0.5 K (Randel et al., 2000). The simulated QBO has little effects on static stability and vertical wind shear in the tropical upper troposphere.

MIROC6 can also simulate Sudden Stratospheric Warming (SSW), which is a typical intra-seasonal variability of the mid-latitude stratosphere in the Northern Hemisphere. Standard deviation of monthly and zonal-mean zonal wind (colors) superimposed on monthly climatology of zonal-mean zonal wind (black contours) in February are shown in Fig. 24 (a)-(c). There are two maxima of the standard deviations over the equatorial stratosphere and the mid-to-high latitude upper stratosphere in the Northern Hemisphere in observations (Fig. 24a), which correspond to QBO and polar vortex variability. This feature is well captured in MIROC6 (Fig. 24b), while there are too small variations in MIROC5 where the stratosphere cannot be well resolved (Fig. 24c). The better representation of the polar vortex variability in MIROC6 is closely associated with that of the SSW. As shown in the bottom panels of Fig. 24, abrupt and short-lived warming events associated with SSW are detected in MIROC6, which are reproduced comparably to observations in terms of magnitude, but are not detected in MIROC5. This is consistent with previous modeling studies that reported the importance

881 of the well-resolved stratosphere for better simulation of stratospheric variability (e.g., Cagnazzo and
882 Manzini, 2009; Charlton-Perez et al., 2013; Osprey et al., 2013). In December–January, however,
883 MIROC6 still underestimates the frequency of SSW events, which is a common bias in other high-top
884 climate models (e.g., Inatsu et al., 2007; Charlton-Perez et al., 2013; Osprey et al., 2013). It is
885 conjectured that the less frequent SSW in December–January could be attributed to less frequent
886 stationary wave breakings due to overestimate of climatological zonal wind speed of the polar night
887 jet in MIROC6 (Figs. 24d and e).

888 The inclusion of a well-resolved stratosphere in MIROC6 is also considered to be
889 important for improvement in representation of stratosphere-troposphere coupling. In order to evaluate
890 this, we examine the time-development of the Northern Annular Modes (NAM) associated with
891 strongly weakened polar vortex events in the stratosphere. The NAM indices are defined by the first
892 EOF mode of the zonal-mean year-round daily geopotential height anomalies over the Northern
893 Hemisphere and are computed separately at each pressure level (Baldwin and Thompson, 2009). The
894 height anomalies are first filtered by a 10-day low-pass filter to remove transient eddies. Figure 25
895 shows the composite of time development of the NAM index for weak polar vortex events. The events
896 are determined by the dates on which the 10 hPa NAM index exceeded -3.0 standard deviations
897 (Baldwin and Dunkerton, 2001). Note that the NAM index is multiplied by the square root of the
898 eigenvalue in each level before the composite, that is, the composite having the geopotential height
899 dimension. The weak polar vortex signal in the stratosphere propagates downward to the surface and
900 persists approximately 60 days in the lower stratosphere and upper troposphere. These observational
901 features are well represented in MIROC6 (Figs. 25ab). Although MIROC5 has also captured
902 downward propagating signals, its magnitude is approximately half in the stratosphere, and its
903 persistency is weak in the lower stratosphere and upper troposphere. Therefore, these results strongly
904 indicate that the inclusion of a well-resolved stratosphere in a model is important for representing not

905 only stratospheric variability, but also stratosphere-troposphere coupling.

906

907 **3.2.3 El Niño/Southern Oscillation and Indian Ocean Dipole mode**

908 Among the various internal climate variabilities on interannual timescales, ENSO is of
909 great importance because it can influence climate not only in tropics but also mid- and high latitudes
910 of both hemispheres through atmospheric teleconnections associated with wave propagations (e.g.,
911 Hoskins and Karoly, 1981; Alexander et al., 2002). Here, we describe representation of ENSO and
912 related teleconnection pattern. Figure 26 shows anomalies of SST, precipitation, the 500 hPa pressure
913 height, and the equatorial ocean temperature regressed onto the NINO3 index which is defined as the
914 area average of the SST in [5°S–5°N, 150°W–90°W]. ProjD and ERA-I in 1980–2009 are used as
915 observations. Although the maximum of the SST anomalies in the tropical Pacific is shifted more
916 westward than in observations, the ENSO-related SST anomalies simulated in both of MIROC6 and
917 MIROC5 are globally consistent with observations (Figs. 26a-c). Simulated positive precipitation
918 anomalies in MIROC6 still overextend to the western Pacific (Figs. 26d-f). Meanwhile, dry anomalies
919 over the maritime continent, the eastern equatorial Indian Ocean, and the SPCZ are better simulated
920 in MIROC6 than in MIROC5. ENSO teleconnection patterns in Z500 (Figs. 26g-i) are also realistically
921 simulated as seen in, for example, the Pacific-North American pattern (Wallace and Gutzler, 1981).
922 Equatorial subsurface ocean temperature anomalies in MIROC6 are more confined within the
923 thermocline than in MIROC5 (Figs. 26j-l), and the signals in MIROC6 are closer to observations.
924 However, the subsurface signals in MIROC6 reside deeper than in observations. This is due to the
925 difference in the climatological structure of the equatorial thermocline, which is attributed to the
926 overestimate of the trade winds over the equatorial Pacific, as mentioned in Section 3.1.2.

927 As well as ENSO, the Indian Ocean Dipole (IOD) mode is recognized as a prominent
928 interannual variability (Saji et al., 1999; Webster et al., 1999). Figure 27 shows anomalies of SST, 10

m wind, and precipitation regressed onto the autumn (September–November) dipole mode index (DMI) which is defined as the zonal difference of the anomalous SST averaged over [10°S–10°N, 50°E–70°E] and that averaged in [10°S–10°N, 90°E–110°E]. ProjD and ERA-I in 1980–2009 are used as observations. The observed positive IOD phase is characterized by a basin-wide zonal mode with positive (negative) SST anomalies in the western (eastern) Indian Ocean, and precipitation is increased (decreased) over the positive (negative) SST anomalies (Figs. 27ad). The dipole SST pattern is better simulated in MIROC6 than in MIROC5 where the eastern SST anomalies are located more southward than in observations (Figs. 27a-c). Correspondingly, a meridional dipole pattern in the precipitation of MIROC5 is alleviated, and MIROC6 shows a zonal dipole precipitation pattern, as in observations (Figs. 27d-f). Seasonal IOD phase locking to boreal autumn, which is assessed based on RMS amplitude of the DMI, is also better simulated in MIROC6 than in MIROC5 (not shown). Seasonal shoaling of the eastern equatorial thermocline in the Indian Ocean is realistically simulated in MIROC6 during boreal summer to autumn. The shallower thermocline leads the stronger thermocline feedback which is evaluated based on the SST anomalies regressed onto the 20°C isotherm depth anomalies averaged over the eastern part of the IOD region. As displayed in the top of the upper panels of Fig. 27, the thermocline feedback in MIROC6 is comparable to observations. This larger thermocline feedback in MIROC6 possibly leads to the above-mentioned improvements in the IOD pattern. Note that the simulated surface wind anomalies are more realistic in MIROC6 than in MIROC5, although the magnitude of SST anomalies is overestimated in MIROC6. The overestimate of the SST anomalies may have arisen from an excessive response of the equatorial and coastal Ekman up- and down-welling to the wind changes, which are favorable in coarse-resolution ocean models.

3.2.4 Decadal-scale variations in the Pacific and Atlantic Oceans

On longer-than-interannual timescales, the PDO (Mantua et al., 1997) or the Inderdecadal

953 Pacific Oscillations (IPO; Power et al., 1999) is known to be a dominant climate mode that is detected
954 in the SST and the SLP over the North Pacific. To examine simulated PDO patterns, monthly SST and
955 wintertime (December–February) SLP anomalies are regressed onto the PDO index defined as the 1st
956 EOF mode of the North Pacific SST to the north of 20°N and are shown in Fig. 28. In order to detect
957 the decadal-scale variation, the COBE-SST2/SLP2 data (Hirahara et al., 2014) from 1900 to 2013 are
958 used as observations. Negative SST anomalies in the western and central North Pacific and positive
959 SST anomalies in the eastern North Pacific are found in observations. These signals are also
960 represented in both of MIROC6 and MIROC5. The regression of SLP anomalies corresponding to the
961 deepening of the Aleutian low are well simulated in the models over the subarctic North Pacific, and
962 it can be seen that the amplitudes of the SLP anomalies are larger in MIROC6 than in MIROC5, which
963 is closer to the observation. In the tropical Pacific, positive SST anomalies, which are among the more
964 important driving processes of the PDO (e.g. Alexander et al., 2002), are seen in both the models and
965 the observations. In MIROC5, the 5-yr running means of the wintertime (November–March) North
966 Pacific Index (NPI), defined as the SLP averaged over [30°N–65°N, 160°E–140°W], are less sensitive
967 to the NINO3 index (correlation coefficient r = -0.37) than to the NINO4 index (r = -0.64). Note that
968 the NINO4 index is defined as the area average of the SST in [5°S–5°N, 160°E–150°W]. The distorted
969 response of the extratropical atmosphere to the tropical SST variations works to unsuitably modify the
970 extratropical ocean and plays a major role in limiting the decadal predictability of the PDO index in
971 MIROC5 (Mochizuki et al., 2014). In contrast, those in MIROC6 are well correlated with the NINO3
972 index (r = -0.61) in addition to the NINO4 index (r = -0.62). Overestimate of the tropical signals of
973 MIROC5 in the western tropical Pacific are also alleviated in MIROC6. The above-mentioned PDO
974 improvement and the linkage between the tropics and the mid-latitude North Pacific imply a potential
975 for improved skills in initialized decadal climate predictions.
976 In the Atlantic Ocean, there is another decadal-scale variability, which is called the AMO

977 (Schlesinger and Ramankutty, 2004). Figure 29 shows anomalies of SST and SLP regressed onto the
978 AMO index, which is defined as the area average of the SST anomalies in the North Atlantic [0°–
979 60°N, 0°–80°W] with the global-mean SST anomalies subtracted (Trenberth and Shea, 2006). As in
980 the PDO, the centennial-long data of the COBE-SST2/SLP2 data in 1900–2013 are used as
981 observations. The observed AMO spatial pattern in its positive phase is characterized by positive SST
982 anomalies in the off-equator and the subarctic North Atlantic, and by negative or weakly-positive SST
983 anomalies in the western subtropical North Atlantic (Fig. 29a). Corresponding to negative (positive)
984 SLP anomalies over the subtropical (subarctic) North Atlantic, the mid-latitude westerly jet is weaker
985 in a positive AMO phase than in normal years. These spatial patterns in the SST and SLP are simulated
986 in both of MIROC6 and MIROC5. It is especially noteworthy that the positive SST anomalies in low
987 latitudes have larger amplitudes in MIROC6 than in MIROC5, and they extend to the South Atlantic
988 as in observations (Figs. 29bc). On the other hand, the positive SST anomalies in the subarctic region
989 are underestimated in MIROC6, which may be due to the smaller RMS amplitudes of NADW transport
990 in MIROC6 (see Section 3.1).
991
992 **3.3 Climate sensitivity**
993 Following the regression method by Gregory et al. (2004) and Gregory and Webb (2008),
994 we conducted abrupt CO_2 quadrupling experiments with MIROC6 and MIROC5 in order to evaluate
995 effective climate sensitivity (ECS), radiative forcing, and climate feedback. The CO_2 quadrupling
996 experiments were initiated from the pre-industrial control runs. Data from the first 150 years after the
997 CO_2 increase were used for the analysis.
998 ECS, $2 \times CO_2$ radiative forcing, and climate feedback for MIROC6 are estimated to be 2.6
999 K, 3.7 Wm^{-2}, and -1.4 $Wm^{-2}K^{-1}$, respectively (Fig. 30a and Table 2). The ECS, radiative forcing, and
1000 climate feedback in MIROC6 are lower, higher, and negatively larger than those of the CMIP5 multi-

model ensemble means, although these estimates for MIROC6 are within the ensemble spread of the multi-models (Andrews et al., 2012). The ECS of MIROC6 is almost the same as MIROC5 because the decrease in radiative forcing is counterbalanced by the positive increase in climate feedback, although the change in climate feedback is small and not statistically significant. The decrease in radiative forcing of MIROC6 relative to MIROC5 is evident in the longwave and shortwave cloud components (LCRE and SCRE in Fig. 30b and Table 3). On the other hand, the clear-sky shortwave component (SWclr) increases in MIROC6 relative to MIROC5, which partially cancels the differences between the two models. The positive increase in climate feedback is pronounced in the SCRE, which is partially offset by the decrease in the clear sky longwave (LWclr) and SWclr (Fig. 30c and Table 3).

We now focus on the SCRE of the radiative forcing and climate feedback, which show the largest differences between the two models, and compare the geographical distribution (Fig. 31). The distribution is calculated by regressing the changes in SCRE caused by the CO_2 increase at each latitude-longitude grid box against the change in the global-mean SAT. There is a large difference in the geographical distribution between MIROC6 and MIROC5, with the former showing more pronounced zonal contrast in the tropical Pacific than the latter. The changes in the global mean from MIROC5 to MIROC6 (Figs. 30bc) are correlated with the changes in the western tropical Pacific, showing more negative radiative forcing and more positive climate feedback, which are partially offset by the changes in the central tropical Pacific with opposite signs. The radiative forcing and climate feedback tend to show similar geographical patterns with opposite signs in each model.

4. Summary and discussions

The sixth version of a climate model, MIROC6, was developed by a Japanese climate modeling community, aiming at contributing to the CMIP6 through deeper understanding of a wide range of climate science issues and seasonal-to-decadal climate predictions and future climate

projections. The model configurations and basic performances in the pre-industrial control simulation have been described and evaluated in the present manuscript. Major changes from MIROC5, which was our official model for the CMIP5, to MIROC6 are mainly done in the atmospheric component. These include implementation of a parameterization of shallow convective processes, the higher model top and vertical resolution in the stratosphere. The ocean and land-surface components have been also updated in terms of the horizontal grid coordinate system and higher vertical resolution in the former, and parameterizations for sub-grid scale snow distribution and wet lands due to snow-melting water in the latter. Overall, the model climatology and internal climate variability of MIROC6, which are assessed in comparison with observations, are better simulated than in MIROC5.

Overestimate of low-level cloud amounts in low latitudes, which can be partly attributed to insufficient representation of shallow convective processes, are significantly alleviated in MIROC6. The free atmosphere becomes wetter and the precipitation over the western tropical Pacific becomes larger in MIROC6 than in MIROC5, primarily due to vertical mixing of the humid air in the planetary boundary layer with the dry air in the free troposphere. Shallow convections also contribute to better propagation characteristics of intra-seasonal variability associated with MJO in MIROC6, as well as East Asian summer monsoon variability on interannual timescales. In addition, QBO, which is absent in MIROC5, appears in MIROC6 because of its better stratospheric resolution and non-orographic gravity wave drag parameterization.

Climatic mean and internal climate variability in the mid-latitudes are also improved in MIROC6. Together with enhanced activity of sub-weekly disturbances, the tropospheric westerly jets in MIROC6 are shifted more poleward and are stronger than in MIROC5, especially in the Northern Hemisphere. Overestimates in zonal wind speed of the polar night jet are reduced in MIROC6. These advanced representations lead to tighter interactions between the troposphere and the stratosphere in MIROC6. SSW events in the form of polar vortex destructions induced by upward momentum transfer

1049 from the troposphere to the stratosphere (e.g., Matsuno, 1971), are well captured in MIROC6. On
1050 interannual timescales, the improvement of the westerly jet results in better representations of the
1051 spatial wind pattern of the wintertime East Asian monsoon. Associated with changes in the large-scale
1052 atmospheric circulations, the western boundary currents in the oceans, the Kuroshio-Oyashio current
1053 system, the Gulf Stream, and their extensions are better simulated in MIROC6. The increase in warm
1054 water transport from the subtropical North Atlantic to the Barents Sea seems to melt the sea ice in the
1055 Barents Sea, and to alleviate the overestimate of the wintertime sea-ice area that is seen in that region
1056 in MIROC5. Another improvement in MIROC6 is found in the climatological snow cover fractions in
1057 the early winter over the Northern Hemisphere continents. In the Southern Hemisphere, however, the
1058 underestimate of mid-level clouds and the corresponding warm SAT bias, the underestimate of sea-ice
1059 area, and the overestimate of incoming shortwave radiation in the Southern Ocean, all of which are
1060 attributed to errors in cloud radiative and planetary boundary layer processes (e.g., Bodas-Salcedo et
1061 al., 2012; Williams et al., 2013), remains the same as in MIROC5.

1062 Qualitatively, the linkage representations between the tropics and the mid-latitudes
1063 associated with ENSO in MIROC6 are mostly the same as in MIROC5. Meanwhile, oceanic
1064 subsurface signals, which partly control ENSO characteristics, are more confined along the equatorial
1065 thermocline in MIROC6, which is consistent with observations. Regarding the PDO, tropical influence
1066 on the mid-latitudes is more dominant in MIROC6 than in MIROC5, suggesting improvements in
1067 decadal-scale atmospheric teleconnections in MIROC6.

1068 The above descriptions are mainly on the Pacific internal climate variabilities. Regarding
1069 the Indian Ocean, the zonal dipole structures in the SST and precipitation associated with the
1070 interannual variability, known as the IOD, are better simulated in MIROC6 than in MIROC5, which
1071 has a bias of a false meridional precipitation pattern. In the Atlantic, the multi-decadal variability,
1072 known as the AMO, is represented in both the models roughly consistent with observations, but their

reproducibility shows both drawbacks and advantage. Signals associated with AMO in the subarctic (tropical) region are underestimated in MIROC6 (MIROC5).

As a metric for climate change induced by atmospheric CO_2 increase, ECS is also estimated. Although the model configurations and performances are different between the models, the ECS is almost the same (2.5 K). However, looking at geographical distributions of radiative forcing and climate feedback, the amplitudes of shortwave cloud components are much larger in MIROC6 than in MIROC5. Since the larger negative (positive) radiative forcing and positive (negative) climate feedback in the western (central) tropical Pacific cancel each other, global-mean quantities in MIROC6 almost remain the same as in MIROC5. As a topic of future study, estimating radiative forcing and climate feedback with Atmospheric Model Intercomparison Project-type experiments in order to check robustness of the present study would be desirable. Elucidating the impact of different geographical patterns of radiative forcing and climate feedback on the projected future climates would also be useful.

After conducting the pre-industrial control simulation and evaluating the model reproducibility of the mean climate and the internal climate variability, ensemble historical simulations that were initiated from the pre-industrial simulations were executed using the historical forcing data recommended by the CMIP6 protocol. Figure 32 shows a time series of the global-mean SAT anomalies with respect to the 1961–1990 mean. There are 30 (5) ensemble members in the MIROC6 (MIROC5) historical simulations. Note that the MIROC5 historical simulations are executed using the forcing datasets of the CMIP5 protocol. As shown in Fig. 32, the simulated SAT variations in both of MIROC6 and MIROC5 follow observations (HadCRUTv4.4.0; Morice et al., 2012; the data are available at https://crudata.uea.ac.uk/cru/data/temperature/) on a centennial timescale. The temperature rises from the nineteenth century to the early twenty-first century are about 0.72 K in MIROC6, 0.85 K in MIROC5, and 0.82 K in observations, respectively. Focusing on the period from the 1940s to the 1960s, the SAT variations seem to be better simulated in MIROC6 than in MIROC5,

1097 which can be due to both of an update of the forcing datasets and the larger ensemble number in
1098 MIROC6. On the other hand, the warming trend during the first half of the twentieth century in the
1099 models is about half as large as in observations. Whether it can be attributed to internal climate
1100 variability (e.g., Thompson et al., 2014; Kosaka and Xie, 2016) or to an externally forced mode (e.g.,
1101 Meehl et al., 2003; Nozawa et al., 2005) is still being debated. The so-called recent hiatus of the global
1102 warming (Easterling and Wehner, 2009) in the first decade of the twenty-first century is not simulated
1103 in both of MIROC6 and MIROC5. The observed hiatus is considered to occur in association with a
1104 negative IPO phase as internal climate variations (e.g., Meehl et al., 2011; Watanabe et al., 2014). As
1105 external drivers of the hiatus, the increase in stratospheric water vapor and the weakening of solar
1106 activity are given as possible candidates, for example (e.g., Solomon et al., 2010; Kaufmann et al.,
1107 2011). Failure of simulating the hiatus in the models could be attributed to uncertainties in the
1108 historical forcing datasets or cancellation of internal climate variations of the IPO by ensemble-mean
1109 manipulation of the individual historical simulations.

1110 As summarized above, the overall reproducibility of the mean climate and the internal
1111 variability in the latest version of our climate model, MIROC6, has progressed, as well as the historical
1112 warming trend of the climate system. During the first trial of the preindustrial simulation conducted
1113 just after the model configuration was frozen, however, the model reproducibility was not as good as
1114 seen in MIROC5. As described in Section 2.5, we intensively tuned the model by perturbing
1115 parameters associated with, especially, cumulus and shallow convections, and planetary boundary
1116 processes. In addition, before starting the historical simulations, we estimated and tuned the radiative
1117 forcing due to aerosol-radiation and aerosol-cloud interactions by changing the parameters of cloud
1118 microphysics in order to ensure that the estimated radiative forcing would be closer to the best-estimate
1119 of the IPCC-AR5 (IPCC, 2013). Without this parameter tuning, the simulated warming trend after the
1120 1960s was 70% as large as seen in observations. This dependence of radiative forcing and

reproducibility of the warming trend on cloud microphysics has also been reported in other climate models (Golaz et al., 2013). A recent comparison of cloud mircophysical statistics between climate models and satellite-based observations has pointed out that "tuned" model parameters that were adjusted for adequate radiative forcing and realistic SAT changes do not necessarily ensure cloud properties and rain/snow formations will be consistent with observations and implies the presence of error compensations in climate models (e.g., Suzuki et al., 2013; Michibata et al., 2016). Error compensations are found also in both of global and regional aspects. As described in Section 3.1, the global TOA radiation imbalance in MIROC6 is about -1.1 Wm^{-2}, which is in the acceptable range of observations. However, when the TOA imbalance is examined in parts, cloud radiative components in the model contain non-negligible biases with respect to satellite-based observations. Regarding error compensations in the oceanic processes, for example, the modeled northward transport of CDW, which is within the uncertainty range of observations, is maintained by spurious open ocean convections in the Southern Ocean which often appear in coarse-resolution ocean models where oceanic mesoscale eddies and coastal bottom water formation cannot be represented (e.g., Olbers et al., 2004; Downes and Hogg, 2013).

There remain several key foci of ongoing model development efforts. These include process-oriented refinements of cloud microphysics and convective systems based on constraints from satellite data and feedbacks from cloud-resolving atmospheric models (e.g., Satoh et al., 2014), higher resolutions for representations of regional extremes, oceanic eddies and river floods, and parameterization of tide-induced micro-scale mixing of sea water. Improvement of computational efficiency, especially on massive parallel computing systems, is among the urgent issues for long-term and large ensemble simulations. These improvements can contribute to deeper understanding of the Earth's climate, reducing uncertainties in climate projections and predictions, and more precise evaluations of human influences on carbon-nitrogen cycles when applied to Earth system models.

Code and data availability. Please contact the corresponding author if readers may want to validate the model configurations of MIROC6 and MIROC5 and to conduct replication experiments. The source codes and required input data will be provided by the modeling community where the author belongs. The model output from the CMIP6/CMIP5 pre-industrial control and historical simulations used in the present manuscript are distributed through the Earth System Grid Federation and are freely accessible. Details on ESGF are given on the CMIP Panel website (https://www.wcrp-climate.org/wgcm-cmip).

Competing interests. The authors declare that they have no conflict of interest.

Acknowledgements

This research is supported by the "Integrated Research Program for Advancing Climate Models (TOUGOU Program)" from the Ministry of Education, Culture, Sports, Science, and Technology (MEXT), Japan. Model simulations were performed on the Earth Simulator at JAMSTEC and NEC SX-ACE at NIES. The authors are much indebted to Dr. Teruyuki Nishimura and Mr. Hiroaki Kanai for their long-term support in areas related to model developments and server administration. The authors also wish to express thanks to our anonymous reviewers for their suggestions and careful reading of the manuscript.

References

Adcroft, A., Hill, C., and Marshall, J.: Representation of topography by shaved cells in a height coordinate ocean model, Mon. Wea. Rev., 125, 2293–2315, 1997.

Adler, R. F., Huffman, G. J., Chang, A., Ferraro, R., Xie, P., Janowiak, J., Rudolf, B., Schneider, U.,

1169 Curtis, S., Bolvin, D., Gruber, A., Susskind, J., and Arkin, P.: The Version 2 Global Precipitation
1170 Climatology Project (GPCP) Monthly Precipitation Analysis (1979–Present), J. Hydrometeor., 4,
1171 1147–1167, 2003.
1172 Alexander, M. A., Bladé, I., Newman, M., Lanzante, J. R., Lau, N.-C., and Scott, J. D.: The
1173 atmospheric bridge: The influence of ENSO teleconnections on air–sea interaction over the global
1174 oceans, J. Clim., 15, 2205–2231, 2002.
1175 Andrews, T., Foster, P., Boucher, O., Bellouin, N., and Jones, A.: Precipitation, radiative forcing and
1176 global temperature change. Geophys. Res. Lett., 37, doi:10.1029/2010GL043991, 2010.
1177 Andrews, T., Gregory, J. M., Webb, M. J., and Taylor, K. E.: Forcing, feedbacks and climate sensitivity
1178 in CMIP5 coupled atmosphere-ocean climate models, Geophys. Res. Lett., 39, L09712,
1179 doi:10.1029/2012GL051607, 2012.
1180 Arakawa, A. and Konor, C. S.: Vertical differencing of the primitive equations based on the Charney-
1181 Phillips grid in hybrid σ-p vertical coordinates, Mon. Wea. Rev., 124, 511-528, 1996.
1182 Baldwin, M. P. and Dunkerton, T. J.: Stratospheric harbingers of anomalous weather regimes, Science,
1183 294, 581-584, 2001.
1184 Baldwin, M. P. and Thompson, D. W. J.: A critical comparison of stratosphere-troposphere coupling
1185 indices, Quart. J. Roy. Meteorol. Soc., 135, 1661–1672, 2009.
1186 Bamber, J. L. and Aspinall, W. P.: An expert judgement assessment of future sea level rise from the
1187 ice sheets, Nature Clim. Change, 3, 424–427, 2013.
1188 Baran, A. J.: From the single-scattering properties of ice crystals to climate prediction: A way forward,
1189 Atmospheric Res., 112, 45-69, 2012.
1190 Bengtsson, L., Hodges, K. I., and Keenlyside, N.: Will extratropical storms intensify in a warmer
1191 climate? J. Clim., 22, 2276-2301, 2009.
1192 Bitz, C., Holland, M., Weaver, A., and Eby, M.: Simulating the ice-thickness distribution in a coupled

1193 climate model, J. Geophys. Res., 106, 2441–2463, 2001.
1194 Bryan, K.: Accelarating the convergence to equilibrium of ocean-climate models, J. Phys. Oceanogr.,
1195 14, 666-673.
1196 Brodzik, M. and Armstrong, R.: Northern Hemisphere EASE-Grid 2.0 Weekly Snow Cover and Sea
1197 Ice Extent. Version 4, Boulder, Colorado USA: NASA DAAC at the National Snow and Ice Data
1198 Center, 2013.
1199 Cagnazzo, C. and Manzini, E.: Impact of the stratosphere on the winter tropospheric teleconnections
1200 between ENSO and the North Atlantic and European region, J. Clim., 22, 1223-1238, 2009.
1201 Carton, J. A. and Giese, B. S.: A reanalysis of ocean climate using simple ocean data assimilation,
1202 Mon. Wea. Rev., 136, 2999–3017, 2008.
1203 Cavarieli, D. J., Corawford, J. P., Drinkwater M. R., Eppler, D. T., Farmer, L. D., Jentz, R. R., and
1204 Wackerman, C. C.: Aircraft active and passive microwave validation of sea ice concentrations from
1205 the DMSP SSM/I, J. Geophy. Res., 96, 21989-22088, 1991.
1206 Charlton-Perez, A. J., and co-authors: On the lack of stratospheric dynamical variability in low-top
1207 versions of the CMIP5 models, J. Geophys. Res., 118, 2494-2505, 2013.
1208 Chikamoto, Y., Timmermann, A., Luo, J.-J., Mochizuki, T., Kimoto, M., Watanabe, M., Ishii, M., Xie,
1209 S.-P., and Jin, F.-F.: Skillful multi-year predictions of tropical trans-basin climate variability, Nature.
1210 commun., 6, doi:10.1038/ncomms7869, 2015.
1211 Chikira, M. and Sugiyama, M.: A cumulus parameterization with state-dependent entrainment rate.
1212 Part I: Description and sensitivity to temperature and humidity profiles, J. Atmos. Sci., 67, 2171-2193,
1213 2010.
1214 Church, J. A. and White, N. J.: Sea-level rise from the late 19th to the early 21st century, Surv.
1215 Geophys., 32, 585–602, 2011.
1216 Comiso, J. C., Parkinson, C. L., Gersten, R., and Stock, L.: Accelerated decline in the Arctic sea ice

cover, Geophys. Res. Lett., 35, doi:10.1029/2007GL031972, 2008.

Dee, D.. and co-authors: The ERA-Interim reanalysis: configuration and performance of the data assimilation system. Quart J Roy Met. Soc., 137, 535–597, 2011.

Downes, S. M. and Hogg, A. M.: Southern Ocean circulation and eddy compensation in CMIP5 models, J. Clim., 26, 7198-7220, 2013.

Easterling, D. R. and Wehner, M. F.: Is the climate warming or cooling? Geophys. Res. Lett., 36, doi:10.1029/2009GL037810, 2009.

Eyring, V., Bony, S., Meehl, G. A., Senior, C. A., Stevens, B., Stouffer, R. J., and Taylor, K. E.: Overview of the Coupled Model Intercomparison Project Phase 6 (CMIP6) experimental design and organization, Geosci. Model. Dev., 9, 1937-1958, 2016.

Gantt, B., Meskhidze, N., and Kamykowski, D.: A new physically-based quantification of marine isoprene and primary organic aerosol emissions, Atmos. Chem. Phys., 9, 4915-4927, doi:10.5194/acp-9-4915-2009, 2009.

Gantt, B., Meskhidze, N., Facchini, M. C., Rinaldi, M., Ceburnis, D., and O'Dowd, C. D.: Wind speed dependent size-resolved parameterization for the organic mass fraction of sea spray aerosol, Atmos. Chem. Phys., 11, 8777-8790, doi:10.5194/acp-11-8777-2011, 2011.

Gent, P.R., Willebrand, J., McDougall, T.J., and McWilliams, J.C: Parameterizing eddy-induced tracer transports in ocean circulation models, J. Phys. Oceanogr., 25, 463-474, 1995.

Golaz, J. C., Horowitz, L. W., and Levy II, H.: Cloud tuning in a coupled climate model: Impact on 20th century warming, Geophys. Res. Lett., 40, 2246-2251, 2013.

Gregory, D.: Estimation of entrainment rate in simple models of convective clouds, Quart. J. Roy. Meteor. Soc., 127, 53–72, 2001.

Gregory, J. M., Ingram, W. J., Palmer, M. A., Jones, G. S., Stott, P. A., Thorpe, R. B., Lowe, J. A., Johns, T. C., and Williams, K. D.: A new method for diagnosing radiative forcing and climate

sensitivity, Geophys. Res. Lett., 31, L03205, doi:10.1029/2003GL018747, 2004.

Gregory, J. and Webb, M.: Tropospheric adjustment induces a cloud component in CO2 forcing, J. Clim., 21, 58-71, 2008.

Griffies, S. M., Gnanadesikan, A., Dixon, K. W., Dunne, J. P., Gerdes, R., Harrison, M. J., Rosati, A., Russell, J. L., Samuels, B. L., Spelman, M. J., Winton, M., and Zhang, R.: Formulation of an ocean model for global climate simulations, Ocean Sci., 1, 45-79, 2005.

Guenther, A., Hewitt, N., Erickson, D., Fall, R., Geron, C., Graedel, T., Harley, P., Klinger, L., Lerdau, M., McKay, W., Pierce, T., Scholes, B., Steinbrecher, R., Tallamraju, R., Taylor, J., and Zim-merman, P.: A global model of natural volatile organic compound emissions, J. Geophys. Res., 100, 8873–8892, 1995.

Hajima, T., and co-authors: Model description of a new Earth system model “MIROC-ES2L” and the sensitivity analysis of the biogeochemical feedbacks, in preparation.

Hasumi, H.: CCSR Ocean Component Model (COCO) version 4.0, Center for Climate System Research Rep., 25, 103 pp., 2006. [Available online at http://www.ccsr.u-tokyo.ac.jp/hasumi/COCO/coco4.pdf.]

Hegglin, M. I., and co-authors: Historical and future ozone database (1850-2100) in support of CMIP6, in prep.

Hines, C. O.: Doppler-spread parameterization of gravity wave momentum deposition in the middle atmosphere, Part 2: Broad and quasi monochromatic spectra, and implementation, J. Atmos. Solar Terr. Phys., 59, 387–400, 1997.

Hirahara, S., Ishii, M., and Fukuda, Y.: Centennial-scale sea surface temperature analysis and its uncertainty, J. Clim., 27, 57-75, 2014.

Hirota, N., Ogura, T., Tatebe, H., Shiogama, H., Kimoto, M., and Watanabe, M.: Roles of shallow convective moistening in the eastward propagation of the MJO in MIROC6, J. Clim., 31, 3033-3034,

2018.

Hirota, N. and Takahashi, M.: A tripolar pattern as an internal mode of the East Asian summer monsoon, Clim. Dyn., 39, 2219–2238, doi:10.1007/s00382-012-1416-y, 2012.

Hoesly, R.M., and co-authors: Historical (1750-2014) anthropogenic emissions of reactive gases and aerosols from the Community Emission Data System (CEDS), Geosci. Model Dev., 11, 369-408, doi:10.5194/gmd-11-369-2018, 2018.

Hourdin, F., Maurisen, T., Getteleman, A., Golaz, J.-C., Balaji, V., Duan, Q., Folini, D., Klocke, D., Qian, Y., Rauser, F., Rio, C., Tomassini, L., Watanabe, M., and Williamson, D.: The art and science of climate model tuning, Bull. Amet. Meteor. Soc., 98, 589-602, 2017.

Hoskins, B. J. and Karoly, D. J.: The steady linear response of a spherical atmosphere to thermal and orographic forcing, J. Atmos. Sci., 38, 1179-1196, 1981.

Hunke, E. and Dukowicz, J.: An elastic–viscous–plastic model for sea ice dynamics, J. Phys. Oceanogr., 27, 1849–1867, 1997.

Hurtt, G., and co-authors: Harmonization of global land-use change and management for the period 850-2100, Geosci. Model Dev., in preparation.

Inatsu, M., Kimoto, M. and Sumi, A.: Stratospheric sudden warming with projected global warming and related tropospheric wave activity, SOLA, 3, 105-108, 2007.

Ineson, S. and Scaife, A. A.: The role of the stratosphere in the European climate response to El Niño, Nature Geosci., 2, 32-36, 2009.

IPCC: Climate Change 2013: The Physical Science Basis. Contribution of Working Group I to the Fifth Assessment Report of the Intergovernmental Panel on Climate Change, edited by Stocker, T.F. et al., Cambridge University Press, Cambridge, United Kingdom and New York, NY, USA, 1535 pp, 2013.

Ishii, M., Kimoto, M., and Kachi, M.: Historical ocean subsurface temperature analysis with error

estimate, Mon. Wea. Rev., 131, 51-73, 2003.

Imada, Y., Watanabe, M., Mori, M., Kimoto, M., Shiogama, H., and Ishii, M.: Contribution of atmospheric circulation change to the 2012 heavy rainfall in southwestern Japan, Bull. Amer. Meteor. Soc., 95, S52-S54, 2013.

Imada, Y., Tatebe, H., Ishii, M., Chikamoto, Y., Mori, M., Arai, M., Watanabe, M., and Kimoto, M.: Predictability of two types of El-Niño assessed using an extended seasonal prediction system by MIROC, Mon. Wea. Rev., 143, 4597-4617, 2015.

Ito, A. and Inatomi, M.: Use of a process-based model for assessing the methane budgets of global terrestrial ecosystems and evaluation of uncertainty, Biogeosciences, 9, 759-773, 2012.

K-1 model developers: K-1 coupled GCM (MIROC) description, K-1 Tech. Rep., 1, edited by H. Hasumi, H., and Emori, S., 34 pp., Center for Climate System Research, the Univ. of Tokyo, Tokyo, 2004.

Kamae, Y., Shiogama, H., Watanabe, M., Ogura, T., Yokohata, T., and Kimoto, M.: Lower tropospheric mixing as a constraint on cloud feedback in a multiparameter multiphysics ensemble, J. Clim., 29, 6259-6275, 2016.

Katsumate, K., Ohshima, K. I., Kono, T., Itoh, M., Yasuda, I., Volkov, Y., and Wakatsuchi, M.: Water exchange and tidal current through the Bussol's Strait revealed by direct current measurements, J. Geophys. Res., 109, doi:10.1019/2003JC001864, 2004.

Kaufmann, R. K., Kauppi, H., Mann, M. L., and Stock, J. H.: Reconciling anthropogenic climate change with observed temperature 1998–2008, Proc. Natl. Acad. Sci. USA, 108, 11790-11793, 2011.

Kawabe, M. and Fujio, S.: Pacific Ocean circulation based on observation, J. Oceanogr., 66, 389-403, doi:10.1007/s10872-010-0034-8, 2010.

Krinner, G., Viovy, N., de Noblet-Ducoudre, N., Ogee, J., Polcher, J., Friedlingstein, P., Ciais, P., Sitch, S., and Prentice, I. C.: A dynamic global vegetation model for studies of the coupled atmosphere-

biosphere system, Global Biogeochem. Cycles, 19, GB1015, doi:10.1029/2003GB002199, 2005.

Komuro, Y., Suzuki, T., Sakamoto, T. T., Hasumi, H., Ishii, M., Watanabe, M., Nozawa, T., Yokohata, T., Nishimura, T., Ogochi, K., Emori, S., and Kimoto, M.: Sea-ice in twentieth-century simulations by new MIROC coupled models: a comparison between models with high resolution and with ice thickness distribution, J. Meteor. Soc. Japan, 90A, 213–232, 2012.

Komuro, Y. and Suzuki, T.: Impact of subgrid-scale ice thickness distribution on heat flux on and through sea ice, Ocean Modell., 71, 13–25, 2013.

Komuro, Y.: The Impact of Surface Mixing on the Arctic River Water Distribution and Stratification in a Global Ice–Ocean Model, J. Clim., 27, 4359-4370, 2014.

Kosaka, Y. and Nakamura, H.: Mechanisms of meridional teleconnection observed between a summer monsoon system and a subtropical anticyclone. Part I: The Pacific-Japan pattern, J. Clim., 23, 5085–5108, 2010.

Kosaka, Y, and Xie, S.-P.: The tropical Pacific as a key pacemaker of the variable rates of global warming, Nature Geosci., 9, 669-673, 2016.

Kubokawa, A., and Inui, T.: Subtropical Countercurrent in an idealized Ocean OGCM, J. Phys. Oceanogr., 29, 1303-1313, 1999.

Liebmann, B.: Description of a complete (interpolated) outgoing longwave radiation dataset, Bull. Amer. Meteor. Soc., 77, 1275–1277, 1996.

Liston, G.E.: Representing subgrid snow cover heterogeneities in regional and global models, J. Clim., 17, 1381-1397, 2014.

Loeb, N. G., Wielicki, B. A., Doelling, D. R., Smith, G.L., Keyes, D.F., Kato, S., Manalo-Smith, N., and Wong, T.: Toward optimal closure of the earth's top-of-atmosphere radiation budget, J. Clim., 22, 748–766, 2009.

Mantua, N. J., Hare, S. R., Zhang, Y., Wallace, J. M., and Francis, R. C: A Pacific interdecadal climate

oscillation with impacts on salmon production, Bull. Amer. Meteor. Soc., 78, 1069-1079, 1997.

Meehl, G. A., Covey, C., Delworth, T., Latif, M., McAvaney, B., Mitchell, J. F. B., Stouffer, R. J., and Taylor, K. E.: The WCRP CMIP3 multi-model dataset: a new era in climate change research. Bull. Amer. Meteor. Soc., 88, 1383-1394, 2007.

Myneni, R. B., and co-authors: Global products of vegetation leaf area and fraction absorbed PAR from year one of MODIS data, Remote Sens. Environ., 83, 214–231, 2002.

Mori, M., Watanabe, M., Shiogama, H., Inoue, J., and Kimoto, M.: Robust Arctic sea-ice influence on the frequent Eurasian cold winters in past decades, Nature Geosci., 7, 869-873, 2014.

Marshall, A. G., Hendon, H. H., Son, S. W., and Lim, Y.: Impact of the quasi-biennial oscillation on predictability of the Madden–Julian oscillation, Clim. Dyn., doi:10.1007/s00382-016-3392-0, 2016.

McCarthy, G. D., Smeed, D. A., Johns, W. E., Frajka-Williams, E., Moat, B. I., Rayner, D., Baringer, M. O., Meinen, C. S., Collins, J., and Bryden, H. L.: Measuring the Atlantic Meridional Overturning Circulation at 26°N, Prog. Oceanogr., 130, 91-111, doi: 10.1016/j.pocean.2014.10.006, 2015.

Matsuno, T.: A dynamical mode of the stratospheric sudden warming, J. Atmos. Sci., 28, 1479-1494, 1971.

Matthes, K., and co-authors: Solar forcing for CMIP6 (v3.2), Geosc. Model Dev., 10, 2247-2302, doi:10.5194/gmd-10-2247-2017, 2017.

Meehl, G. A., Washington, W. M., Wigley, T. M. L., Arblaster, J. M., and Dai, A.: Solar and greenhouse gas forcing and climate response in the twentieth century, J. Clim., 16, 426-444, 2003.

Meehl, G. A., Arblaster, J. M., Fasullo, J. T., Hu, A., and Trenberth, K. E.: Model-based evidence of deep-ocean heat uptake during surface temperature hiatus periods, Nature Clim. Change, 1, 360-364, 2011.

Meinshausen, M., and co-authors: Historical greenhouse gas concentrations for climate modelling (CMIP6), Geosci. Model Dev., 10, 2057-2116, doi:10.5194/gmd-10-2057-2017, 2017.

1361 Michibata, T., Suzuki, K., Sato, Y., and Takemura, T.: The sources of discrepancies in aerosol-cloud-
1362 precipitation interactions between GCM and A-Train retrievals, Atmos. Chem. Phys., 16, 15413-
1363 15424, 2016.
1364 Mizuta, R.: Intensification of extratropical cyclones associated with the polar jet change in the CMIP5
1365 global warming projections, Geophys. Res. Lett., 39, doi:10.1029/2012GL053032, 2012.
1366 Mochizuki, M., and co-authors: Pacific decadal oscillation hindcasts relevant to near-term climate
1367 prediction, Proc. Natl. Acad. Sci. U.S.A., 107, 1833-1837, 2010.
1368 Mochizuki, T., Kimoto, M., Chikamoto, Y., Mori, M., Watanabe, M., and Ishii, M.: Error sensitivity
1369 to initial climate states in Pacific decadal hindcasts, SOLA, 10, 39-44, 2014.
1370 Mochizuki, T., Kimoto, M., Watanabe, M., Chikamoto, Y., and Ishii, M.: Interbasin effects of the
1371 Indian Ocean on Pacific decadal climate change, Geophys. Res. Lett., 43, 7168-7175, 2016.
1372 Morice, C. P., Kennedy, J. J., Rayner, N. A., and Jones, P. D.: Quantifying uncertainties in global and
1373 regional temperature change using an ensemble of observational estimates: The HadCRUT4 dataset,
1374 J. Geophys. Res., doi:10.1029/2011JD017187, 2012.
1375 Murphy, J. M.: Assessment of the practical utility of extended range ensemble forecasts, Q. J. R.
1376 Meteorol. Soc., 116, 89–125, 1990.
1377 Murray, R. J.: Explicit generation of orthogonal grids for ocean models, J. Comput. Phys., 126, 251–
1378 273, 1996.
1379 Nakamura, H.: Midwinter suppression of baroclinic wave activity in the Pacific, J. Atmos. Sci., 49,
1380 1629–1642, 1992.
1381 Nakamura, T., Toyoda, T., Ishikawa, Y., and Awaji, T.: Tidal mixing in the Kuril Straits and its impact
1382 on ventilation in the North Pacific Ocean, J. Oceanogr., 60, 411-423, 2004.
1383 Nakano, H., and Suginohara, N.: Effects of bottom boundary layer parameterization on reproducing
1384 deep and bottom waters in a world ocean model, J. Phys. Oceanogr., 32, 1209–1227, 2002.

National Geophysical Data Center, 1993: 5-minute Gridded Global Relief Data (ETOPO5), National Geophysical Data Center, NOAA, doi:10.7289/V5D798BF.

Neeling, J. D., Munnich, M., Su, H., Meyerson, J. E., and Holloway, C. E.: Tropical dying trends in global warming models and observations, Proc. Natl. Acad. Sci. U.S.A., 103, 6110-6115, 2006.

Ngo-Duc, T., Oki, T., and Kanae, S.: A variable streamflow velocity method for global river routing model: model description and preliminary results, Hydrol. Earth Syst. Sci. Discuss., 4, 4389-4414, doi:10.5194/hessd-4-4389-2007, 2007.

Ninomiya, K., and Akiyama, T.: Multi-scale features of Baiu, the summer monsoon over Japan and East Asia, J. Meteor. Res. Japan, 70, 467–495, 1992.

Nitta, T., Yoshimura, K., and Abe-Ouchi, A.: Impact of arctic wetlands on the climate system: Model sensitivity simulations with the MIROC5 AGCM and a snow-fed wetland scheme, J. Hydrometeor., 18, 2923-2936, 2017.

Nitta, T., Yoshimura, K., Takata, K., O'ishi, R., Sueyoshi, T., Kanae, S., Oki, T., Abe-Ouchi, A., and Liston, G. E.: Representing variability in subgrid snow cover and snow depth in a global land model, J. Clim., 27, 3318-3330, doi:10.1175/JCLI-D-13-003, 2014.

Nozawa, T., Nagashima, T., Shiogama, H., and Crooks, S.A.: Detecting natural influence on surface air temperature change in the early twentieth century, Geophys. Res. Lett., 32, doi:10.1029/2005GL023540, 2005.

Numaguti, A., Takahashi, M., Nakajima, T., and Sumi, A.: Description of CCSR/NIES atmospheric general circulation model. National Institute for Environmental Studies, Center for Global Environmental Research Supercomputer Monograph Rep., 3, 1-48, 1997.

Olbers, D., Borowski, D., Volker, C., and Wolff, J.-O.: The dynamical balance, transport and circulation of the Antarctic Circumpolar Current. Antarctic Sci., 14, 439-470, 2004.

Oki, T. and Sud, Y.C.: Design of Total Runoff Integrating Pathways (TRIP) - A global river channel

1409 netwerk, Earth Interact., 2, 1-37, 1998.
1410 Ono, J., Tatebe, H., Komuro, Y., Nodzu, M. I., and Ishii, M.: Mechanisms influencing seasonal to
1411 inter-annual prediction skill of sea ice extent in the Arctic Ocean in MIROC, The Cryosphere, 12, 675-
1412 683, 2018.
1413 Osprey, S. M., Gray, L. J., Hardiman, S. C., Butchart, N., and Hinton, T. J.: Stratospheric variability
1414 in twentieth-century CMIP5 simulations of the Met Office climate model: High top versus low top, J.
1415 Clim., 26, 1595-1606, 2013.
1416 Park, S. and Bretherton, C. S.: The University of Washington shallow convection and moist turbulence
1417 schemes and their impact on climate simulations with the Community Atmosphere Model, J. Clim.,
1418 22, 3449-3469, 2009.
1419 Power, S., Casey, T., Folland, C., Colman, A., and Mehta, V.: Interdecadal modulation of the impact
1420 of ENSO on Australia, Clim. Dyn., 15, 319-324, 1999.
1421 Prather, M. J.: Numerical advection by conservation of second-order moments, J. Geophys. Res. 91,
1422 6671–6681, 1986.
1423 Ramankutty, N. and Foley, J.A.: Estimating historical changes in global land cover: croplands from
1424 1700 to 1992, Global Biogeochem. Cycles, 13, 997-1027, 1999.
1425 Rio, M.-H., Mullet, S., and Picot, N.: Beyond GOCE for the ocean circulation estimate: Synergetic
1426 use of altimetry, gravimetry, and in-situ data provides new insight into geostrophic and Ekman currents,
1427 Geophys. Res. Lett., 41, 8192-8925, doi:10.1002/2014GL061773.
1428 Rockström, J., and co-authors: A safe operating space for humanity, Nature, 461, 472-475, 2009.
1429 Riebesell, U., Körtzinger, A., and Oschlies, A.: Sensitivities of marine carbon fluxes to ocean change,
1430 Proc. Natl. Acad. Sci. U.S.A., 106, 20602–20609, 2009.
1431 Roberts, M. J., Clayton, A., Demory, M.-E., Donners, J., Vidale, P. L., Norton, W., Shaffrey, L.,
1432 Stevens, D. P., Stevens, I., Wood, R. A., and Slingo, J.: Impact of resolution on the tropical Pacific

circulation in a matrix of coupled models. J. Clim., 22, 2541–2556, 2009.

Röske, F.: A global heat and freshwater forcing dataset for ocean models, Ocean Modell., 11, 235-297, 2006.

Rossow, W. B., Walker, A. W., Beuschel, D., and Roiter, M.: International Satellite Cloud Climatology Project (ISCCP) documentation of new cloud datasets, World Climate Research Programme (ICSU and WMO), WMO/TD 737, 115pp, 1996.

Scaife, A. A., and co-authors: Climate change projections and stratosphere-troposphere interaction, Clim. Dyn., 38, 2089-2097, 2012.

Scaife, A. A., and co-authors: Skillful long-range predictions of European and North American winters, Geophys. Res. Lett., 41, 2514-2519, 2014.

Saji, N. H., Goswami, B. N., Vinayachandran, P. N., and Yamagata, T.: A dipole mode in the tropical Indian Ocean, Nature, 401, 360–363, 1999.

Sakamoto, T., and co-authors: MIROC4h - A new high-resolution atmosphere-ocean coupled general circulation model, J. Meteor. Soc. Jpn., 90A, 325-359, 2012.

Satoh, M., and co-authors: The non-hydrostatic icosahedral atmospheric model: description and development, Prog. Earth Planet Sci., 1:18, doi:10.1186/s40645-017-014-0018-1, 2014.

Schlesinger, M. E. and Ramankutty, N.: An oscillation in the global climate system of period 65-70 years, Nature, 376, 723－726, 1994.

Sekiguchi, M. and Nakajima, T.: A k-distribution-based radiation code and its computational optimization for an atmospheric general circulation model, J. Quant. Spectrosc. Radiat. Transfer, doi:10.1016/j.jqsrt.2008.07.13, 2008.

Sellers, P.J., and co-authors: The ISLSCP Initiative I global datasets: surface boundary conditions and atmospheric forcings for land-atmosphere studies, Bull. Amer. Meteor. Soc., 1987-2005, 1997.

Shaffrey, L., and co-authors: U.K. HiGEM: The new U.K. high resolution global environment model

- Model description and basic evaluation, J. Clim., 22, 1861–1896, 2009.

Shiogama, H., Watanabe, M., Yoshimori, M., Yokohata, T., Ogura, T., Annan, J.D., Hargreaves, J.C., Abe, M., Kamae, Y., O'ishi, R., Nobui, R., Emori, S., Nozawa, T., Abe-Ouchi, A., and Kimoto, M.: Perturbed physics ensemble using the MIROC5 coupled atmosphere-ocean GCM without flux corrections: experimental design and results, Clim. Dyn., 39, 3041-3056, 2012.

Shiogama, H., Watanabe, M., Imada, Y., Mori, M., Kamae, Y., Ishii, M., and Kimoto, M.: Attribution of the June-July 2013 heat wave in the southwestern United States, SOLA, 10, 122-126, 2014.

Sillmann, J., Kharin, V. V., Zwiers, F. W., Zhang, X., and Bronaugh, D.: Climate extremes indices in the CMIP5 multimodel ensemble: Part 2. Future climate projections, J. Geophys. Res., 118, 2473-2493, 2013.

Solomon, S., Rosenlot, K. H., Portmann, R. W., Daniel, J. S., Davis, S. M., Sanford, T. J., and Plattner, G.-K.: Contributions of stratospheric water vapor to decadal changes in the rate of global warming, Science, 327, 1219-1223.

Steele, M., Morley, R., and Ermold, W.: PHC: A global ocean hydrography with a high-quality Arctic Ocean, J. Clim., 14, 2079-2087, 2001.

Stott, P. A., Stone, D. A. and Allen, M. R.: Human contribution to the European heatwave of 2003, Nature, 432, 610-614, 2004.

Sudo, K., Takahashi, M., Kurokawa, J., and Akimoto, H.: CHASER: A global chemical model of the troposphere 1. Model description, J. Geophys. Res., 107, 4339, doi:10.1029/2001JD001113, 2002.

Suzuki, K., Golaz, J-.C, and Stephens, G. L., 2013: Evaluating cloud tuning in a climate model with satellite observations, Geophys. Res. Lett., 40, 4464-4468, 2013.

Suzuki, T., Saito, F., Nishimura, T., and Ogochi, K.: Heat and freshwater exchanges between sub-models of MIROC version 4, JAMSTEC Rep. Res. Dev., 9, 2009 (in Japanese).

Suzuki, T., Hasumi, H., Sakamoto, T. T., Nishimura, T., Abe-Ouchi, A., Segawa, T., Okada, N., Oka,

A., and Emori, S.: Projection of future sea level and its variability in a high-resolution climate model: ocean processes and Greenland and Antarctic ice-melt contributions, Geophys. Res. Lett., 32, doi:10.1029/2005GL023677, 2005.

Suzuki, T. and Ishii, M.: Regional distribution of sea level changes resulting from enhanced greenhouse warming in the Model for Interdisciplinary Research on Climate version 3.2, Geophys. Res. Lett., 38, doi:10.1029/2010GL045693, 2011.

Takata, K., Emori, S., and Watanabe, T.: Development of the Minimal Advanced Treatments of Surface Interraction and RunOff (MATSIRO), Global and Planetary Change, 38, 209-222, 2003.

Takemura, T., Okamoto, H., Maruyama, Y., Numaguti, A., Higurashi, A., and Nakajima, T.: Global three-dimensional simulation of aerosol optical thickness distribution of various origins, J. Geophys. Res., 105, 17853-17873, 2000.

Takemura, T., Nakajima, T., Dubovik, O., Holben, B. N., and Kinne, S.: Single-scattering albedo and radiative forcing of various aerosol species with a global three-dimensional model, J. Clim., 15, 333-352, 2002.

Takemura, T., Nozawa, T., Emori, S., Nakajima, T. Y., and Nakajima, T.: Simulation of climate response to aerosol direct and indirect effects with aerosol transport-radiation model, J. Geophys. Res., 110, D02202, doi:10.1029/2004JD005029, 2005.

Takemura, T., Egashira, M., Matsuzawa, K., Ichijo, H., O'ishi, R., and Abe-Ouchi, A.: A simulation of the global distribution and radiative forcing of soil dust aerosols at the Last Glacial Maximum, Atmos. Chem. Phys., 9, 3061-3073, doi:10.5194/acp-9-3061-2009, 2009.

Talley, L. D., Reid, J. L., and Robbins, P. E.: Date-based meridional overturning streamfuctions for the global ocean, J. Clim., 16, 3213-3226, 2003.

Tatebe, H. and Yasuda, I: Oyashio southward intrusion and cross-gyre transport related to diapycnal upwelling in the Okhotsk Sea, J. Phys. Oceanogr., 34, 2327-2341, 2004.

Tatebe, H. and Hasumi, H.: Formation mechanism of the Pacific equatorial thermocline revealed by a general circulation model with a high accuracy tracer advection scheme, Ocean Modell., 35, 245-252, 2010.

Tatebe, H., and co-authors: The initialization of the MIROC climate models with hydrographic data assimilation for decadal prediction, J. Meteor. Soc. Jpn., 90A, 275-294, 2012.

Tatebe, H., Imada, Y., Mori, M., Kimoto, M., and Hasumi, H.: Control of decadal and bidecadal climate variability in the tropical Pacific by the off-equatorial South Pacific Ocean, J. Clim., 26, 6524-6534, 2013.

Taucher, J. and Oschlies, A.: Can we predict the direction of marine primary production change under global warming? Geophys. Res. Lett., 38, doi:10.1029/2010GL045934, 2011.

Taylor, K. E., Stouffer, R. J., and Meehl, G. A.: A summary of the CMIP5 experiment design. https://pcmdi.llnl.gov/?cmip5/docs/Taylor_CMIP5_22Jan11_marked.pdf, 2011.

Thompson, D. M., Cole, J. E., Shen, G. T., Tudhope, A. W., and Meehl, G. A.: Early twentieth-century warming linked to tropical Pacific wind strength. Nature Geosci., 8, doi:10.1038/ngeo2321, 2014.

Thomason, L., Vernier, J.-P., Bourassa, A., Arfeuille, F., Bingen, C., Peter, T., and Luo, B.: Stratospheric Aerosol Data Set (SADS Version 2) Prospectus, to be submitted to Geosci. Model Dev. Dis-cuss., 2016.

Trenberth, K. E., and Shea, D. J.: Atlantic hurricanes and natural variability in 2005, Geophys. Res. Lett., 33, L12704, doi:10.1029/2006GL026894, 2006.

van Marle, M.J.E., and co-authors: Historic global biomass burning emissions for CMIP6 (BB4CMIP) based on merging satellite observations with proxies and fire models (1750-2015), Geosci. Model Dev., 10, 3329-3357, doi:10.5194/gmd-10-3329-2017, 2017.

Waliser, D. E., Li, J.-L. F., L'Ecuyer, T. S., and Chen, W.-T.: The impact of precipitating ice and snow on the radiation balance in global climate models, Geophys. Res. Lett., 38, L06802,

1529 doi:10.1029/2010GL046478, 2011.
1530 Wallace, J. M. and Gutzler, D. S.: Teleconnections in the geopotential height field during the northern
1531 hemisphere winter, Mon. Wea. Rev., 109, 784-812, 1981.
1532 Watanabe, M., Suzuki, T., O'ishi, R., Komuro, Y., Watanabe, S., Emori, S., Takemura, T., Chikira, M.,
1533 Ogura, T., Sekiguchi, M., Takata, K., Yamazaki, D., Yokohata, T., Nozawa, T., Hasumi, H., Tatebe, H.,
1534 and Kimoto, M.: Improved climate simulation by MIROC5: Mean states, variability, and climate
1535 sensitivity, J. Clim., 23, 6312-6335, DOI: 10.1175/2010JCLI3679.1, 2010.
1536 Watanabe, M., Chikira, M., Imada, Y., and Kimoto, M.: Convective control of ENSO, J. Climate, 24,
1537 543-562, 2011.
1538 Watanabe, M., Shiogama, H., Tatebe, H., Hayashi, M., Ishii, M., and Kimoto, M.: Contribution of
1539 natural decadal variability to global warming acceleration and hiatus, Nature Clim. Change, 4, 893-
1540 897, 2014.
1541 Watanabe, M., Shiogama, H., Imada, Y., Mori, M., Ishii, M., and Kimoto, M.: Event attribution of the
1542 August 2010 Russian heat wave, SOLA, 9, 65-68, 2013.
1543 Watanabe, S.: Constraints on a non-orographic gravity wave drag parameterization using a gravity
1544 wave resolving general circulation model, SOLA(Scientific Online Letters on the Atmosphere), 4, 61–
1545 64, doi:10.2151/sola.2008-016, 2008.
1546 Watanabe, S., Kawatani, Y., Tomikawa, Y., Miyazaki, K., Takahashi, M., and Sato, K.: General aspects
1547 of a T213L256 middle atmosphere general circulation model, J. Geophys. Res., 113, D12110,
1548 doi:10.1029/2008JD010026, 2008.
1549 Watanabe, S., Hajima, T., Sudo, K., Nagashima, T., Takemura, T., Okajima, H., Nozawa, T., Kawase,
1550 H., Abe, M., Yokohata, T., Ise, T., Sato, H., Kato, E., Takata, K., Emori, S., and Kawamiya, M.:
1551 MIROC-ESM 2010: model description and basic results of CMIP5-20c3m experiments, Geosci.
1552 Model Dev., 4, 845-872, doi:10.5194/gmd-4-845-2011, 2011.

1553 Watanabe, M., and Kawamiya, M.: Remote effects of mixed layer development on ocean acidification
1554 in the subsurface layers of the North Pacific, J. Oceanogr., 73, 771-784, 2017.
1555 Wood, R. and Bretherton, C. S.: On the relationship between stratiform low cloud cover and lower-
1556 tropospheric stability, J. Clim., 19, 6425-6432, 2006.
1557 Webster, P. J., Moore, A. M., Loschnigg, J. P., and Leben, R. R.: Coupled ocean-atmosphere dynamics
1558 in the Indian Ocean during 1997-98, Nature, 401, 35-360, 1999.
1559 Wheeler, M. and Kiladis, G. N.: Convectively coupled equatorial waves: Analysis of clouds and
1560 temperature in the wavenumberfrequency domain, J. Atmos. Sci., 56, 374-399, 1999.
1561 Yamazaki, D., Oki, T., and Kanae, S.: Deriving a global river network map and its sub-grid topographic
1562 characteristics from a fine-resolution flow direction map, Hydrol. Earth Syst. Sci., 13, 2241–2251,
1563 2009.
1564 Yang, P., Lei, B., Baum, B.A., Liou, K-N., Kattawar, G.W., Mischenko, M. I., and Cole, B.: Spectrally
1565 consistent scattering, absorption, and polarization properties of atmospheric ice crystals at
1566 wavelengths from 0.2 to 100 μm, J. Atm. Sci., 70, 330-347, 2013.
1567 Yoo, C. and Son, S. W.: Modulation of the boreal wintertime Madden Julian oscillation by the
1568 stratospheric quasi-biennial oscillation, Geophys. Res. Lett., 43, 1392-1398, 2016.
1569 Zappa, G., Shaffrey, L. C., Hodges, K. I., Sansom, P. G., and Stephenson, D. B.: A multi-model
1570 assessment of future projections of North Atlantic and European extratropical cyclones in the CMIP5
1571 climate models, J. Clim., doi:10.1175/JCLI-D-12-00573.1, 2013.
1572 Zhang, X. B., and co-authors: Detection of human influence on twentieth-century precipitation trends,
1573 Nature, 448, 461-464, 2007.
1574 Zhang, Y., Sperber, K. R., and Boyle, J. S.: Climatology and interannual variation of the East Asian
1575 winter monsoon: Results from the 1979-95 NCEP/NCAR reanalysis, Mon. Wea. Rev., 125, 2605-2619,
1576 1997.

Zhang, Y., Rossow, W. B., Lacis, A. A., Oinas, V., and Mishchenko, M. I.: Calculation of radiative fluxes from the surface to top of atmosphere based on ISCCP and other global data sets: Refinements of the radiative transfer model and the input data, J. Geophys. Res., 109, doi:10.1029/2003JD004457, 2004.

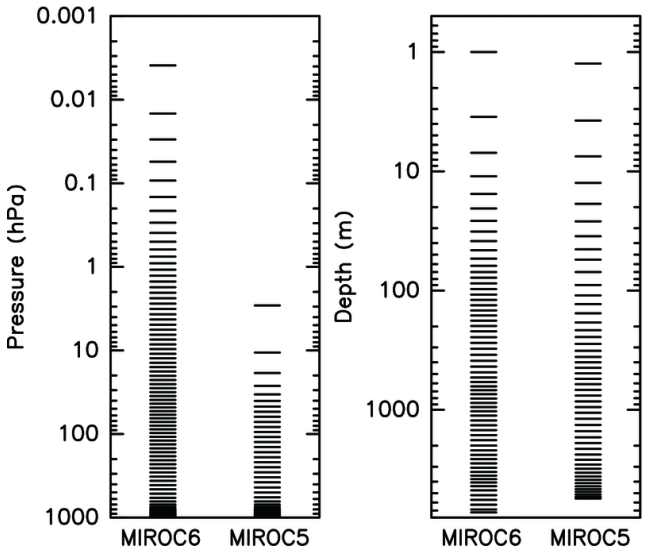

Fig. 1. Vertical half levels for the atmospheric (left panel) and the oceanic (right panel) components of MIROC6 and MIROC5.

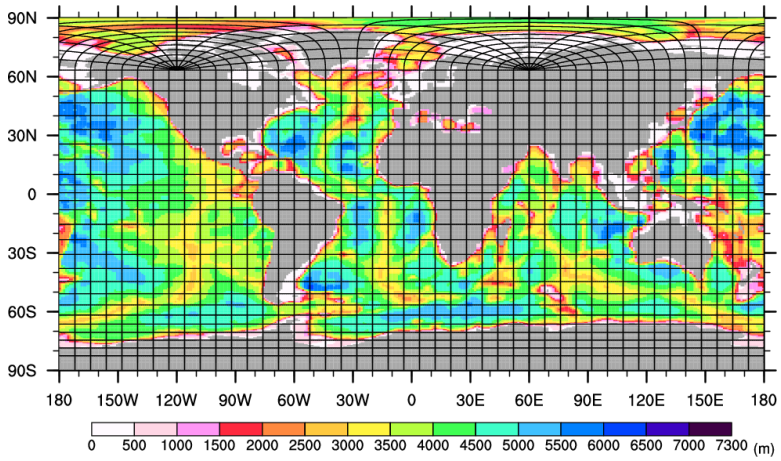

Fig. 2. Horizontal grid coordinate system and model bathymetry of the ocean component of MIROC6.

1591

1592

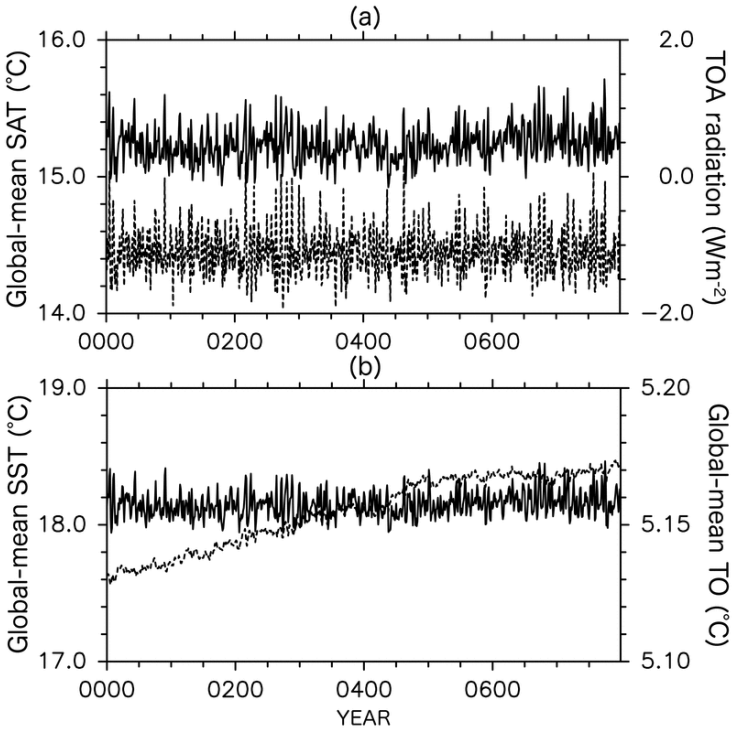

1593

1594 Fig. 3. (a) Time series of the global-mean SAT (solid) and the TOA radiation budget (dashed; upward

1595 positive). (b) Same as (a), but for the global-mean SST (solid) and the ocean temperature through the

1596 full water column (dashed).

1597

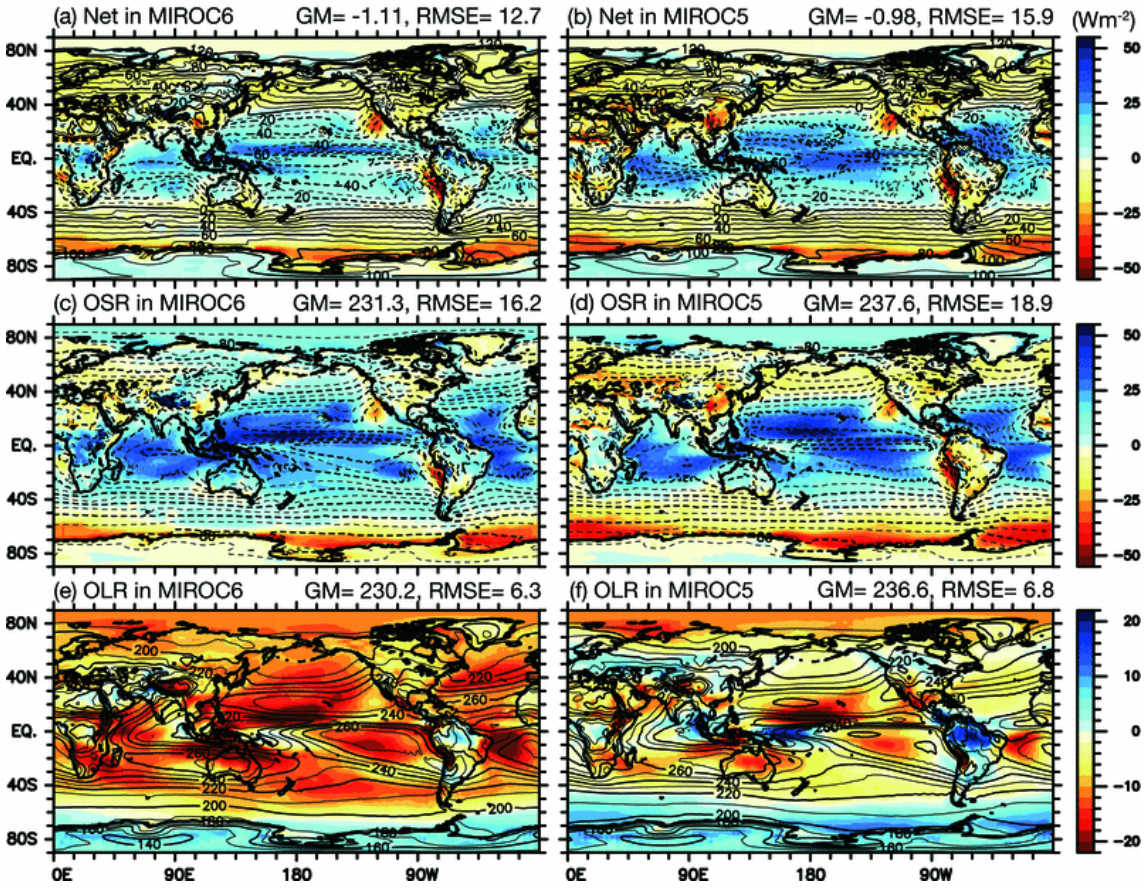

Fig. 4. Annual-mean TOA radiative fluxes in MIROC6 (left panels) and MIROC5 (right panels). Upward is defined as positive. Net shortwave and longwave radiative fluxes, and the sum of the two fluxes are denoted as OSR, OLR, and NET, respectively. Colors indicate errors with respect to observations (CERES) and contours denote values in each model. Note that a different color scale is used for the longwave radiations. The global-mean values and root-mean-squared errors are indicated by GM and RMSE, respectively. In the present manuscript, RMSE is computed without model and observed global-mean quantities unless otherwise noted.

1610

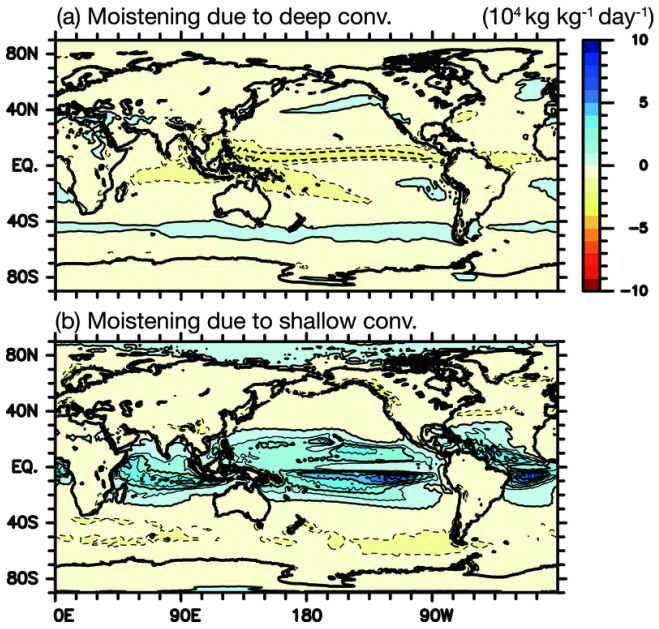

1611

1612 Fig. 5. Annual-mean moistening rate associated with (a) deep convections and (b) shallow convections

1613 in MIROC6 at the 850 hPa pressure level.

1614

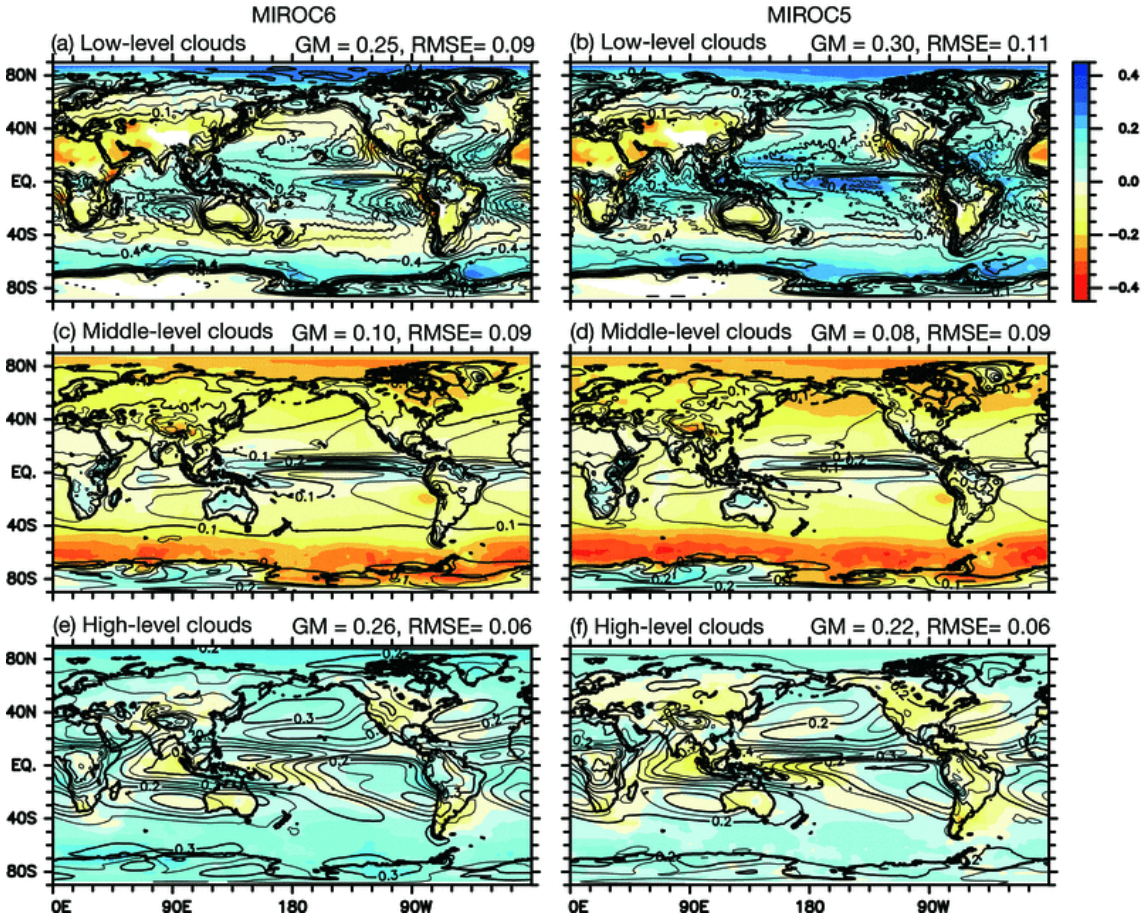

Fig. 6. Same as Fig. 4, but for cloud covers in MIROC6 (left panels) and MIROC5 (right panels). Low-, middle-, and high-level cloud covers are aligned from the top to the bottom. The tops for low-, middle-, and high-level clouds are defined to exist below the 680 hPa, between the 680 hPa and 440 hPa, and above the 440 hPa pressure levels, respectively. The unit is non-dimensional. ISCCP climatology is used as observations.

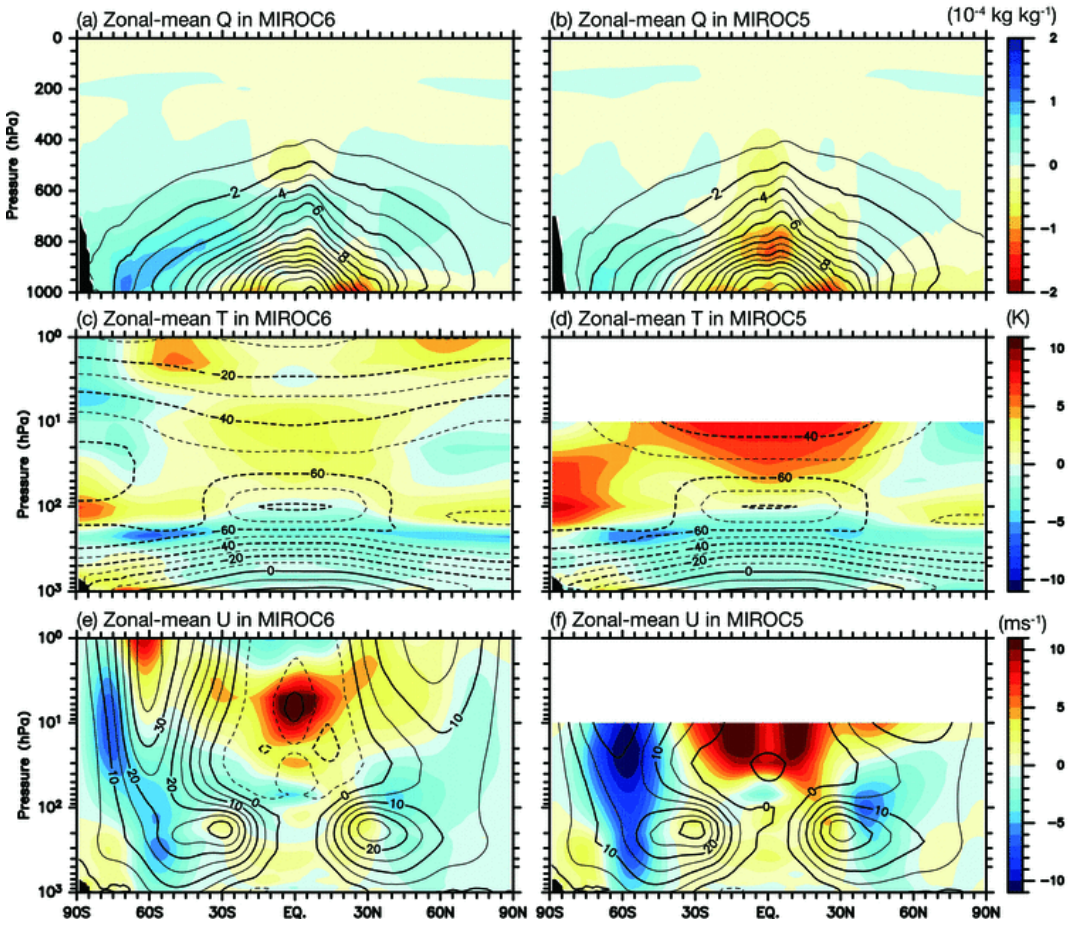

Fig. 7. Annual and zonal-mean specific humidity (top panels), temperature (middle), and zonal wind (bottom) in MIROC6 (left) and MIROC5 (right). Colors indicate errors with respect to observations (ERA-I) and contours denote values in each model.

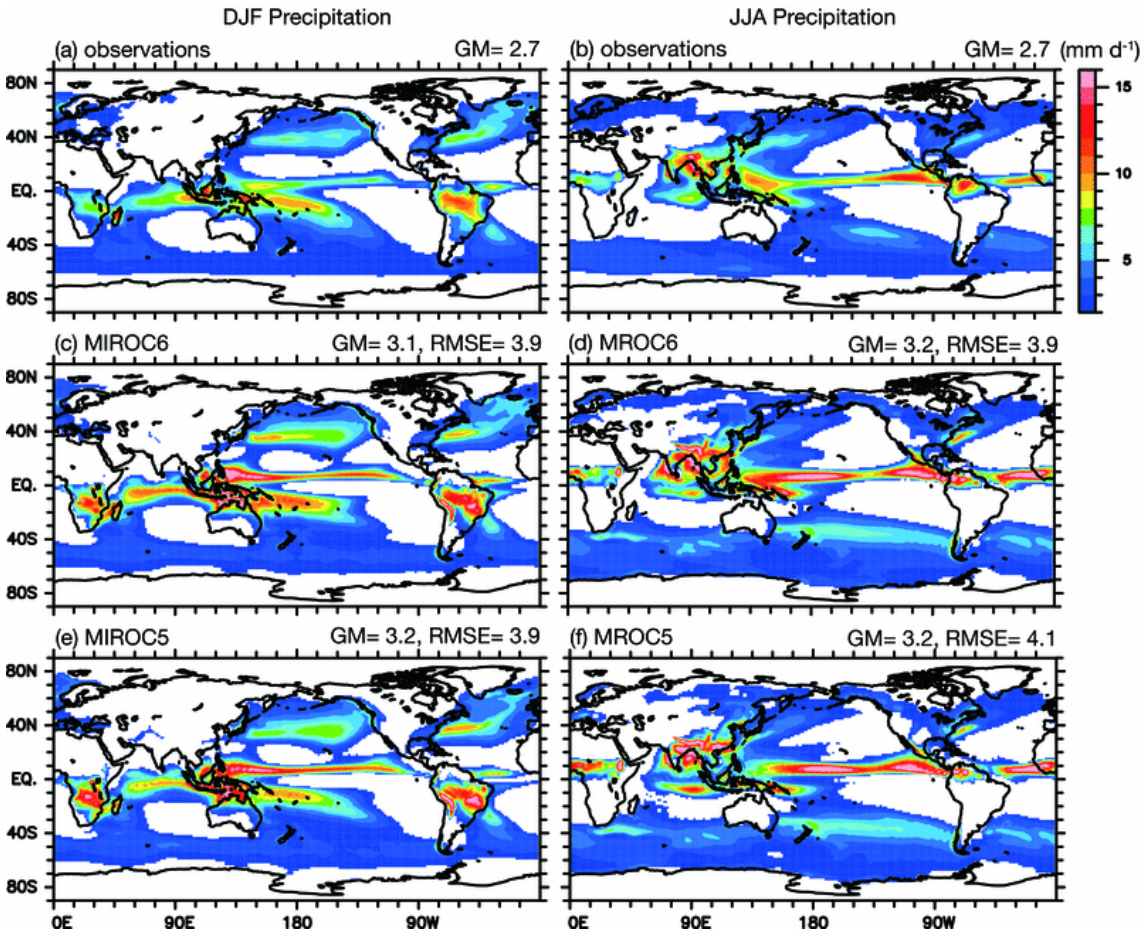

1627

1628 Fig. 8. Precipitation in boreal winter (December–February; left panels) and summer (June–August;

1629 right panels) in observations (top; GPCP), MIROC6 (middle), and MIROC5 (bottom). Areas with

1630 precipitation smaller than 3 mm d^{-1} are not colored.

1631

1632

1633

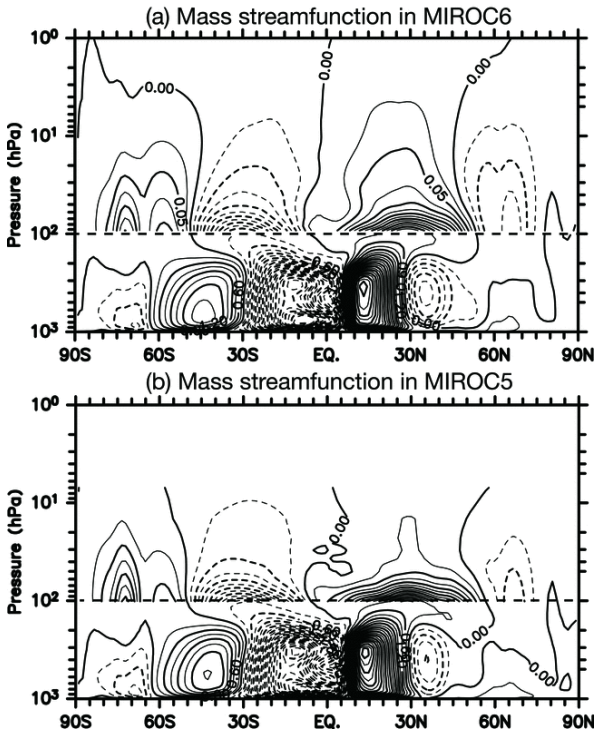

1634

1635 Fig. 9. Annual-mean mass stream functions in (a) MIROC6 and (b) MIROC5. Contour interval is 0.3

1636 $(0.025) \times 10^{10}$ kg s^{-1} below (above) the 100 hPa pressure level. Negative values are denoted by dashed

1637 contours, and the horizontal dashed lines indicate the 100 hPa pressure level.

1638

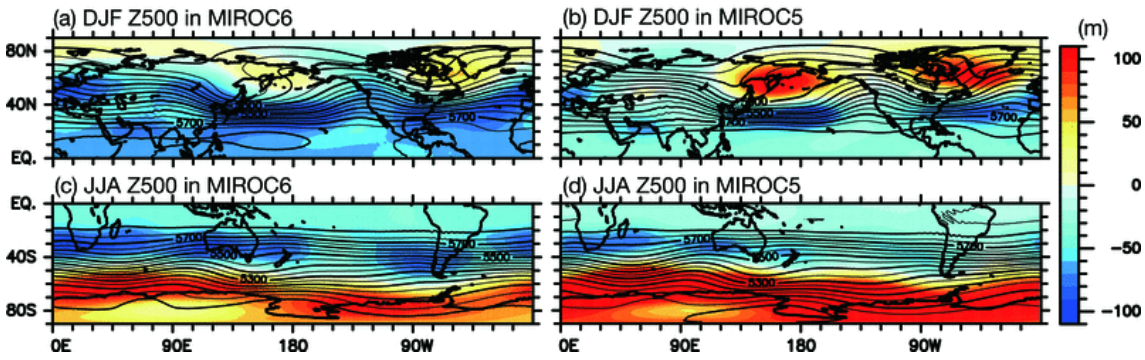

Fig. 10. Same as Fig. 4, but for the wintertime 500 hPa pressure level in MIROC6 (left panels) and MIROC5 (right panels). Maps for boreal (austral) winter are shown in the upper (lower) panels. ERA-I is used as observations.

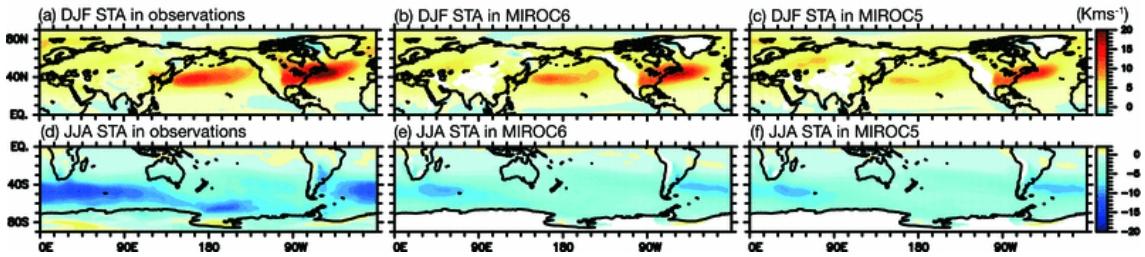

Fig. 11. Wintertime storm track activity (STA) in observations (left), MIROC6 (center), and MIROC5 (right). STA is defined as 8-day-highpass-filtered eddy meridional temperature flux at the 850 hPa pressure level. Maps for boreal (austral) winter are shown in the upper (lower) panels. ERA-I is used as observations.

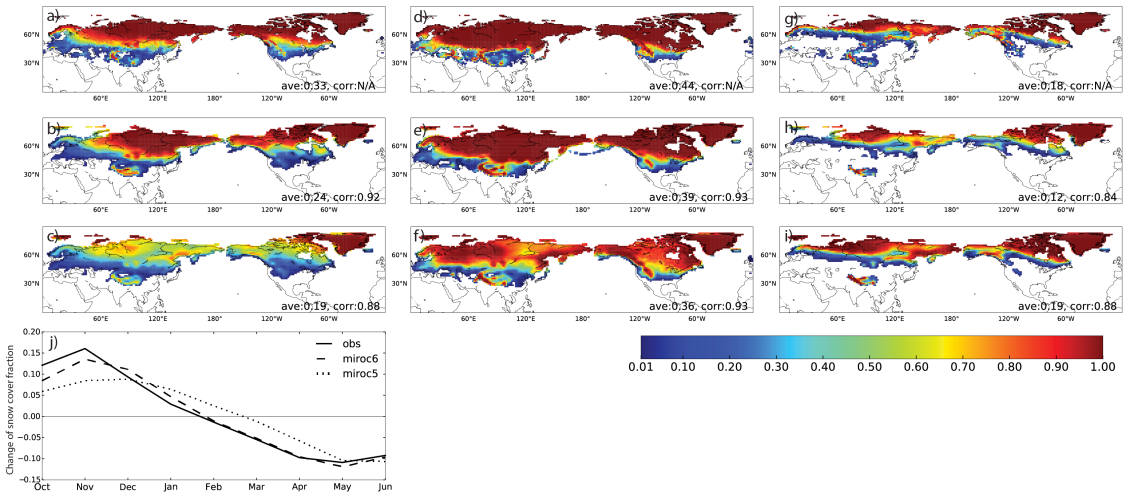

Fig. 12. Snow cover fractions for observations (top panels), MIROC6 (middle), and MIROC5 (bottom). Maps in November, February, and May are aligned from the left to the right. The unit is non-dimensional. Areas where snow cover fractions are less than 0.01 are masked. Ave and corr. in the panels indicate spatial averages and correlation coefficients between observations and models over the land surface in the Northern Hemisphere, respectively. Time series in the bottom-left panel shows temporal rate of change of the monthly spatial averages. Snow-cover dataset of the Northern Hemisphere EASE-Grid 2.0 is used as observations.

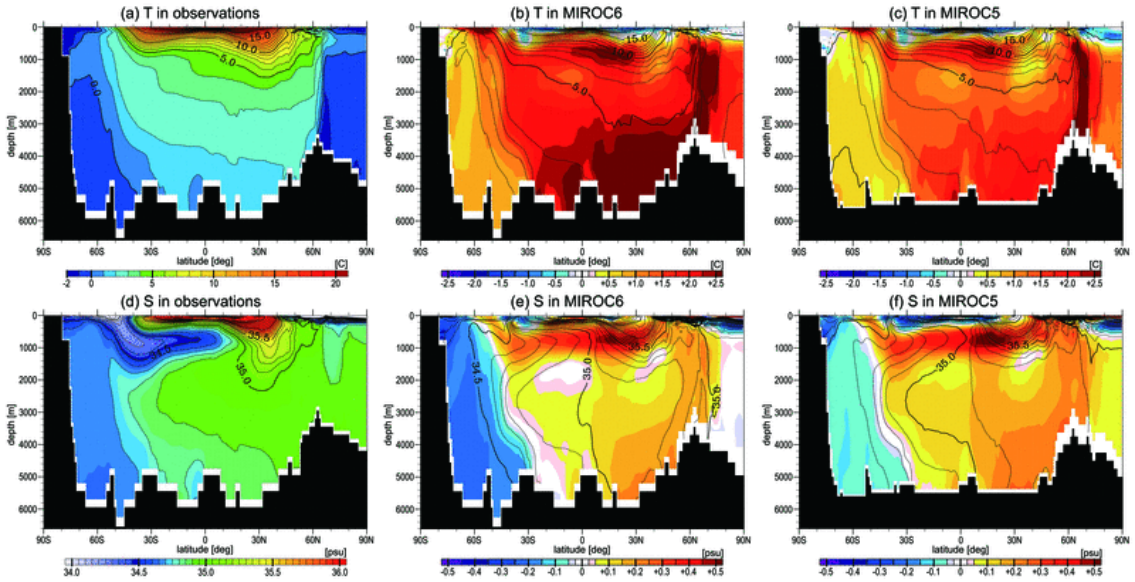

Fig. 13. Annual-mean potential temperature (upper panels; unit is °C) and salinity (lower; psu) in the Atlantic sector for observations (left), MIROC6 (middle), and MIROC5 (right). Colors indicate errors with respect to observations (ProjD) and contours denote model values in the middle and right panels.

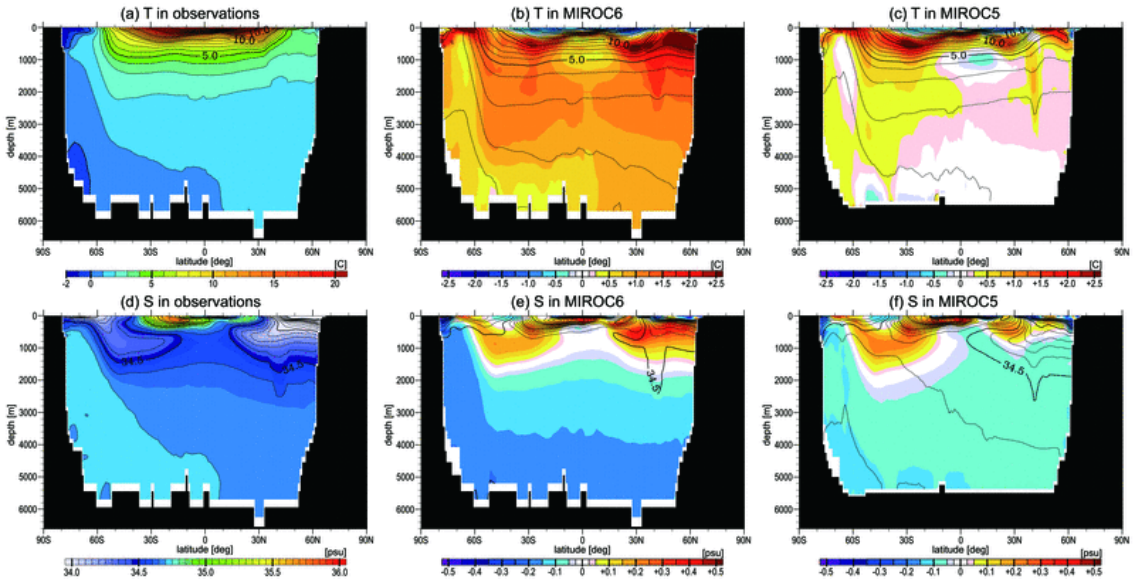

Fig. 14. Same as Fig. 13, but for the Pacific sector.

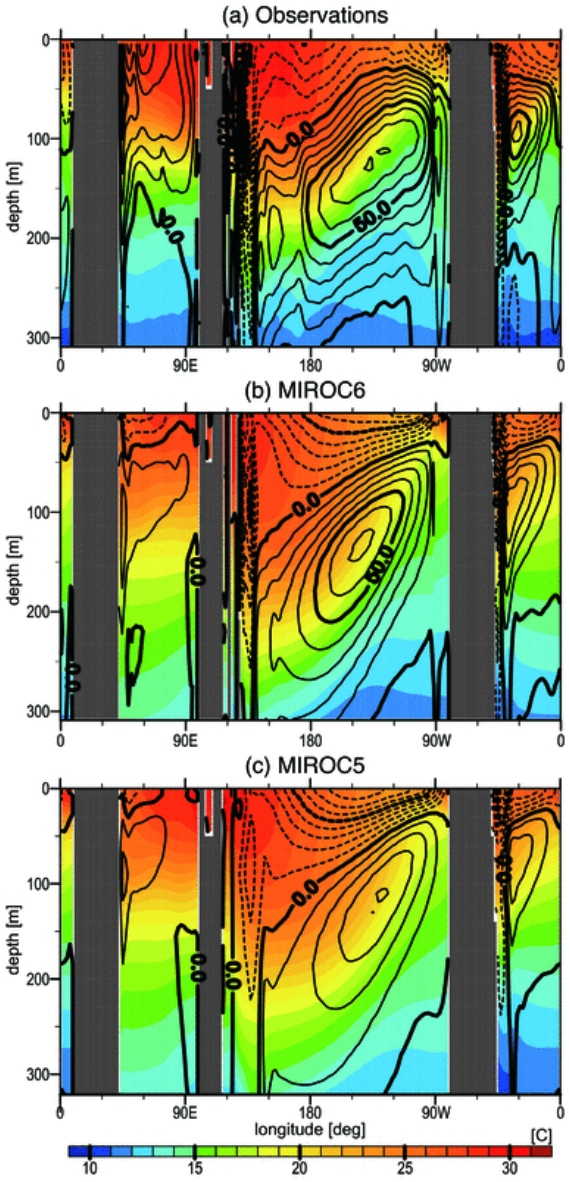

Fig. 15. Annual-mean climatology of potential temperature (°C; colors) and zonal current speed (cm s^{-1}; contours) along the equator (1°S–1°N) in (a) observations (ProjD and SODA), (b) MIROC6, and (c) MIROC5.

1680

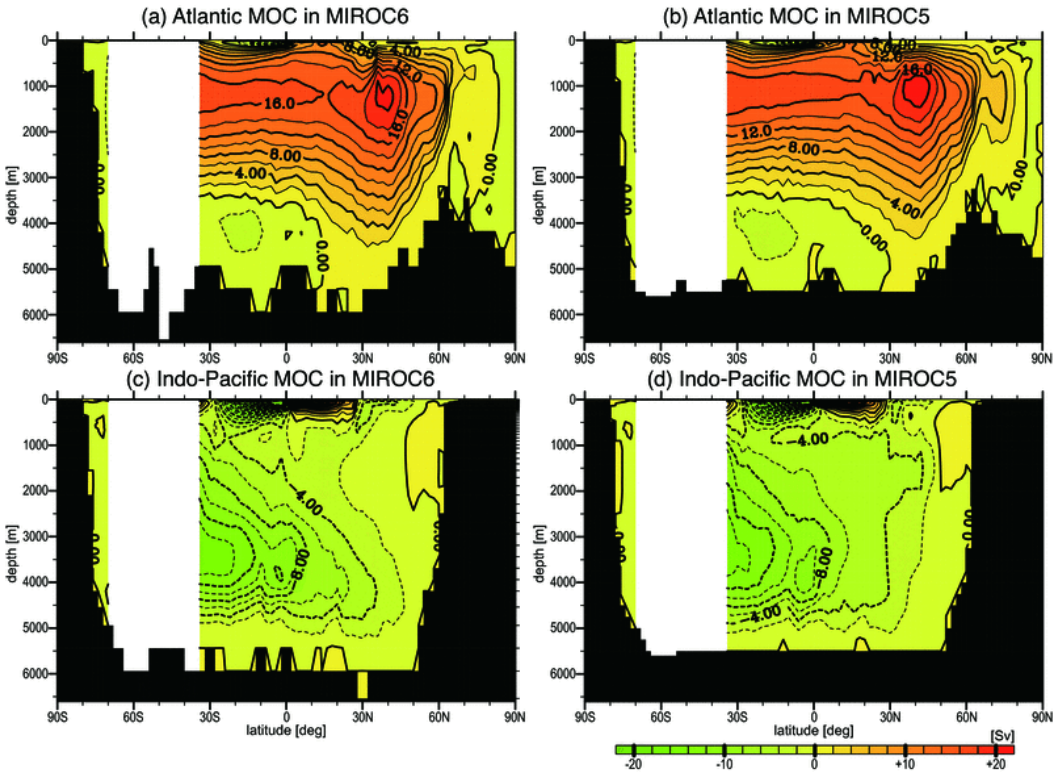

1681

1682 Fig. 16. Annual-mean meridional overturning circulations in the Atlantic (upper panels) and the Indo-

1683 Pacific sectors (lower) in MIROC6 (left) and MIROC5 (right). The unit is Sv ($\equiv 10^6$ $m^3 s^{-1}$).

1684

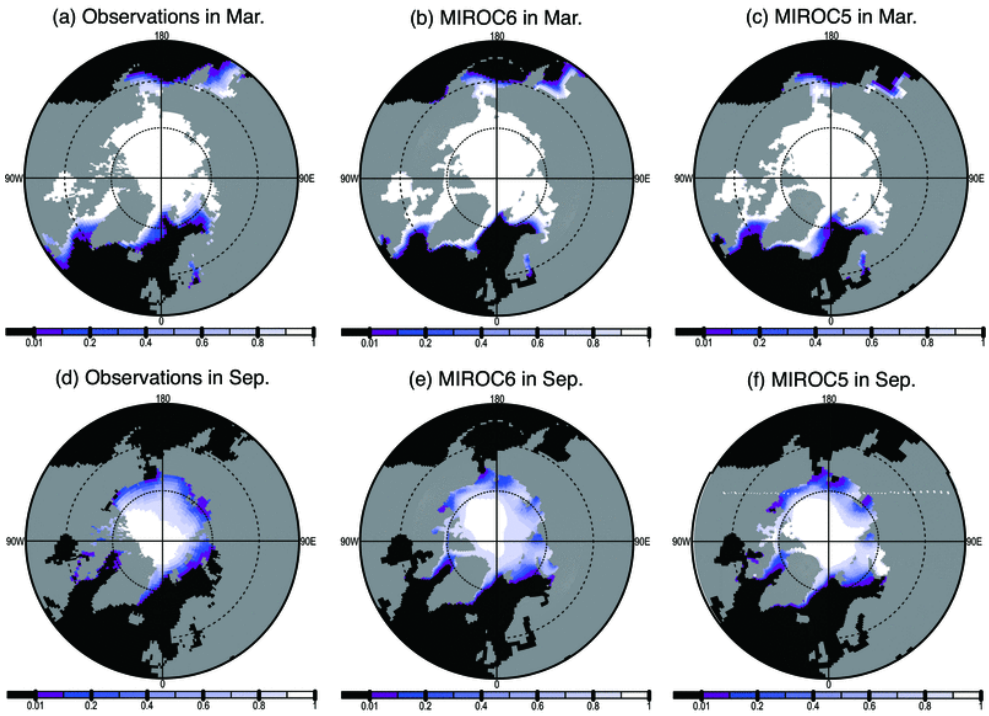

Fig. 17. Northern Hemisphere sea-ice concentrations in March (upper panels) and September (lower panels) for observations (left), MIROC6 (middle), and MIROC5 (right). The unit is non-dimensional. Satellite-based sea-ice concentration data of the SSM/I are used as observations.

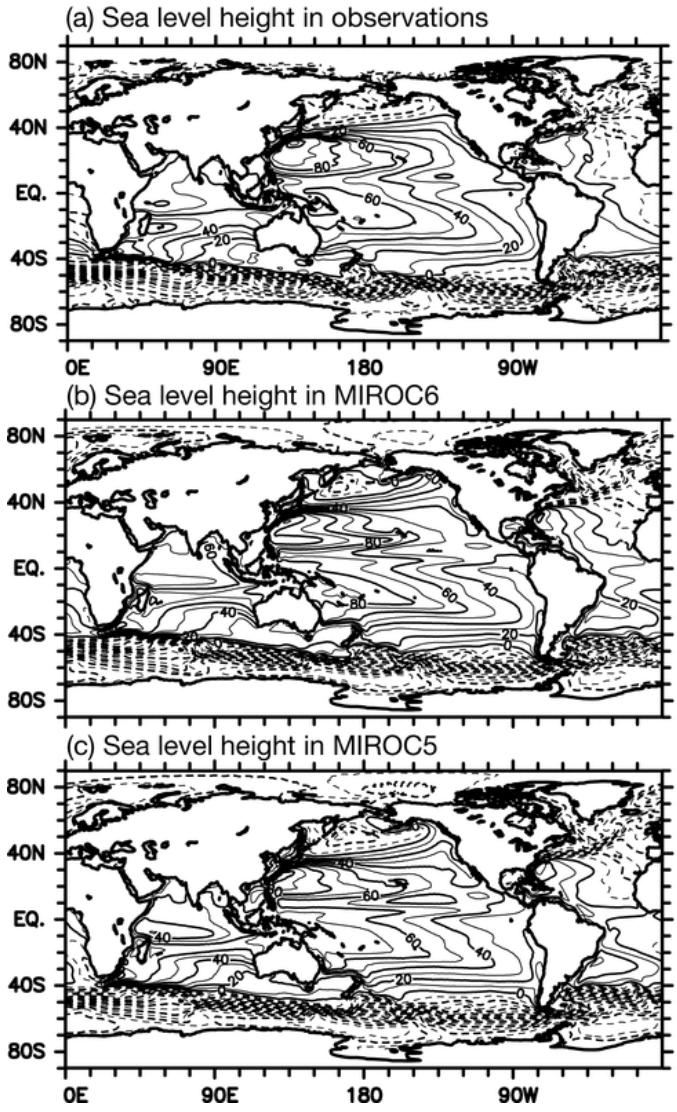

Fig. 18. Annual-mean sea level height relative to the geoid in (a) observations, (b) MIROC6, and (c) MIROC5. Contour interval is 20 cm. Negative values are denoted by dashed lines. Note that loading due to sea-ice and accumulated snow on sea-ice are removed from the model sea level height and that the global-mean value is eliminated.

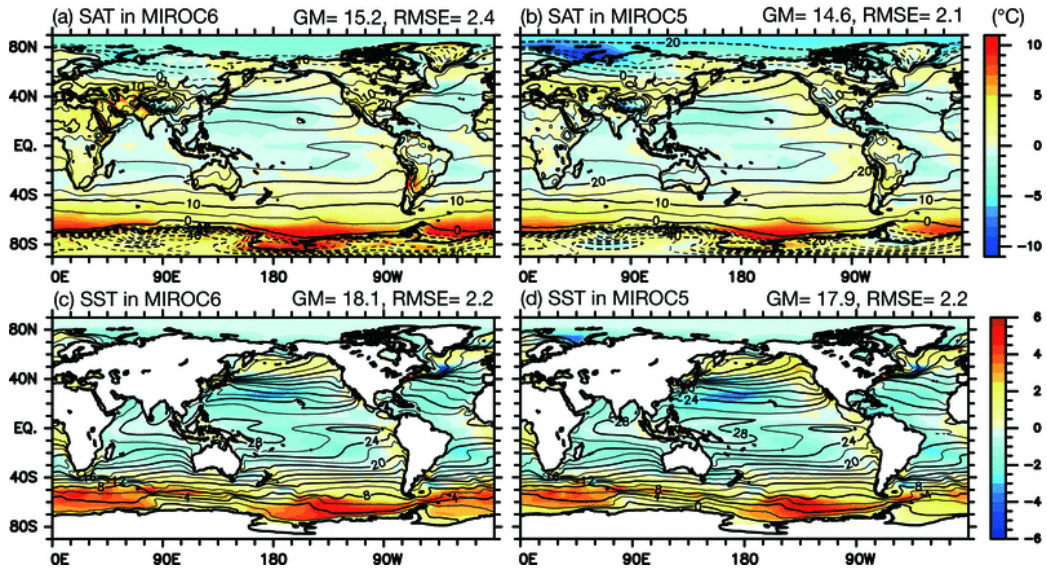

Fig. 19. Same as Fig. 4, but for annual-mean SAT (upper panels) and SST (lower panels). ERA-I for the SAT and the ProjD for the SST are used as observations.

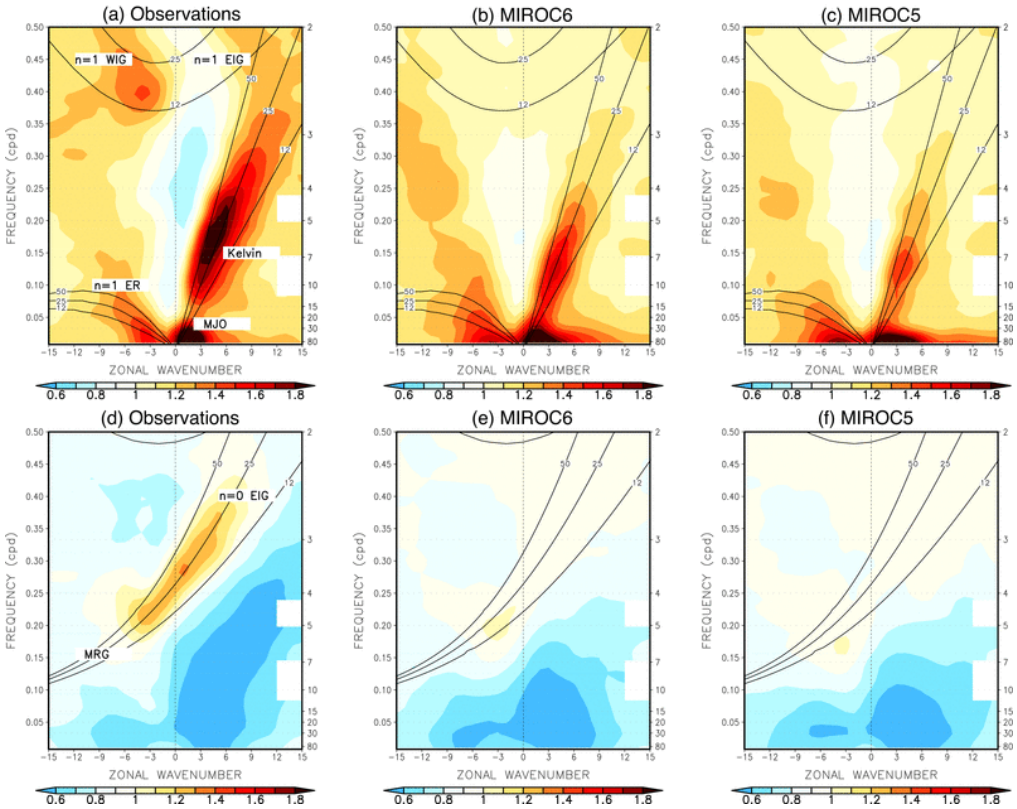

Fig. 20. Zonal wavenumber–frequency power spectra of the (a-c) symmetric and (d-f) antisymmetric component of OLR divided by background power in (a, d) observations (NOAA OLR), (b, e) MIROC6, and (c, f) MIROC5. Dispersion curves of equatorial waves for the three equivalent depths of 12, 25, and 50 m are indicated by black lines. Signals corresponding to the westward and eastward inertia-gravity (WIG and EIG) waves, the equatorial Rossby (ER) waves, equatorial Kelvin waves, the mixed Rossby-gravity waves (MRG), and Madden-Julian oscillation (MJO) are labeled in (a). The unit of the vertical axes is cycle per day (cpd).

1716

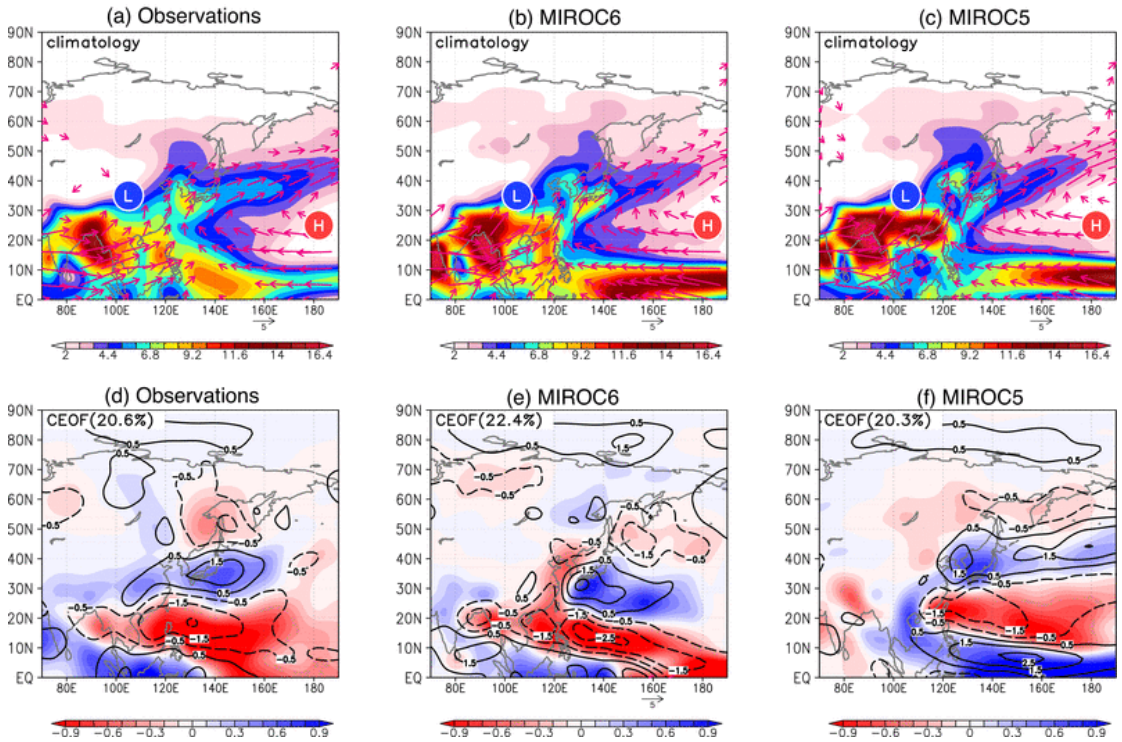

1717

1718 Fig. 21. (a-c) Summertime (JJA) climatology of precipitation (colors, mm day^{-1}) and the 850 hPa

1719 horizontal wind (vector; m s^{-1}) for (a) observations (ERA-I), (b) MIROC6, and (c) MIROC5. (d-f)

1720 Anomalies of summertime precipitation (shading; mm day $^{-1}$) and the 850 hPa vorticity (contour; 10^{-6}

1721 s^{-1}) regressed to the time series of EOF1 of the 850 hPa vorticity over [100°E–150°E, 0°N–60°N] for

1722 (d) observations, (e) MIROC6, and (f) MIROC5.

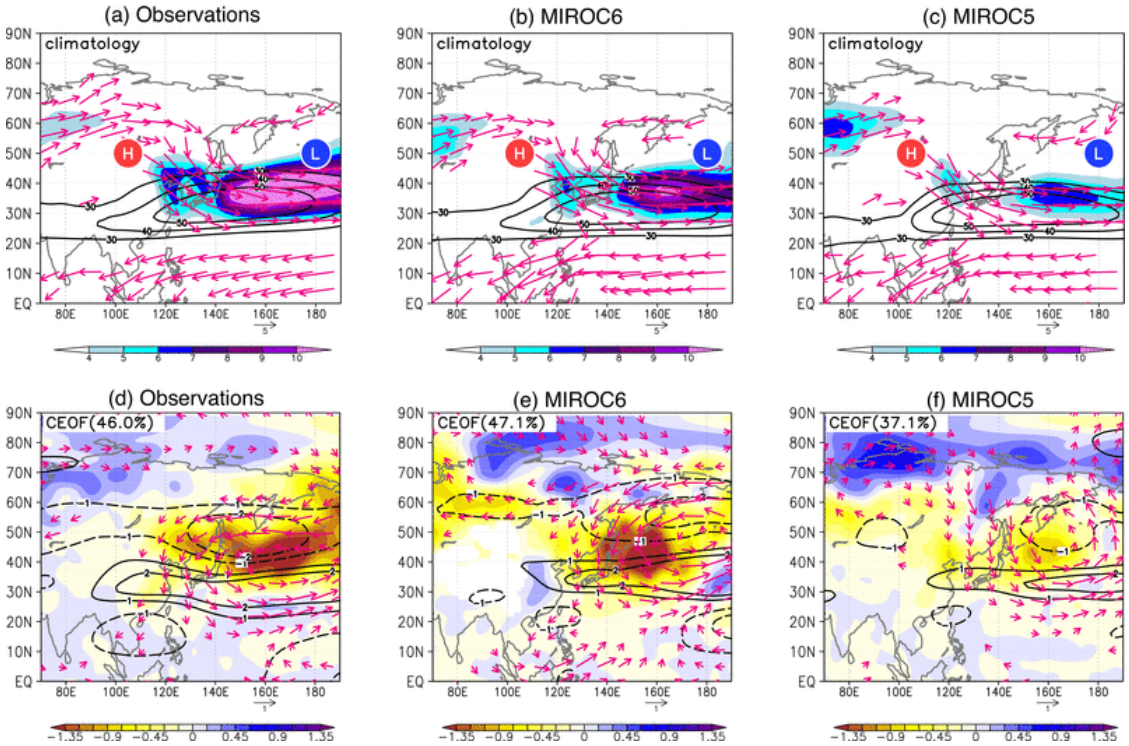

1723

1724 Fig. 22. (a-c) Wintertime (DJF) climatology of STA (colors; K m s^{-1}), the 300 hPa zonal wind (contour;

1725 m s^{-1}), and the 300 hPa horizontal wind (vector; m s^{-1}) for (a) observations (ERA-I), (b) MIROC6, and

1726 (c) MIROC5. (d-f) As in (a-c), but for anomalies regressed onto the time series of the EOF1 of the 850

1727 hPa meridional wind over [120°E–150°E, 30°N–60°N].

1728

1729

1730

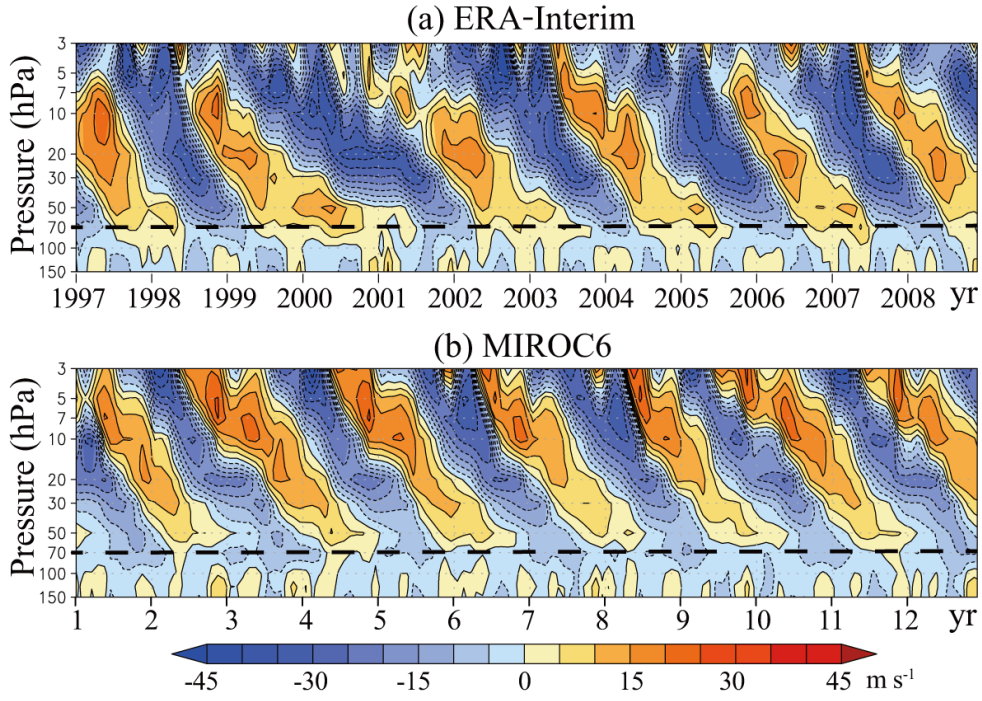

1731

1732 Fig. 23. Time-height cross section of the monthly mean, zonal mean zonal wind over the equator for

1733 (a) observations (ERA-I) and (b) MIROC6. The contour intervals are 5 m s^{-1}. Dashed lines correspond

1734 to the altitude of the 70 hPa pressure level. The red and blue colors correspond to westerlies and

1735 easterlies, respectively.

1736

1737

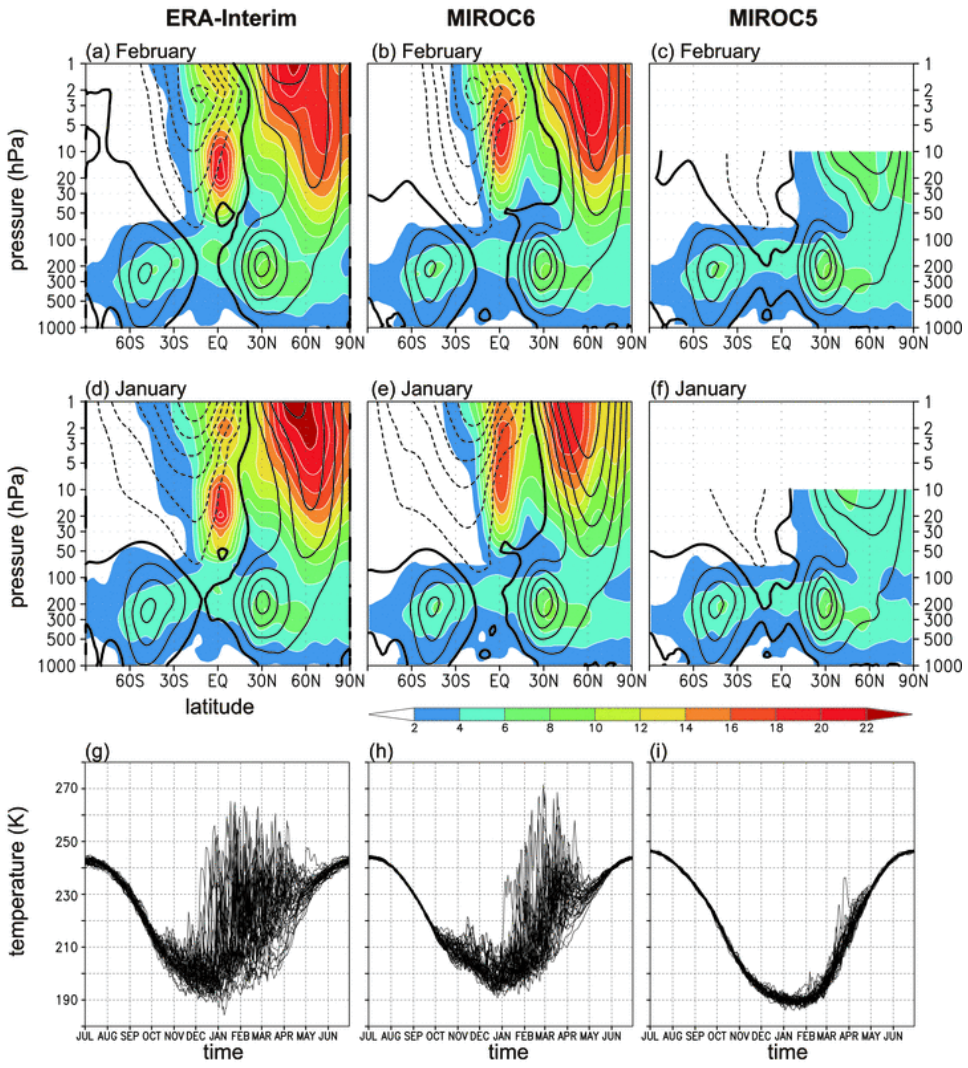

Fig. 24. Standard deviation of monthly and zonal-mean zonal wind (colors; unit is m s^{-1}) superimposed on monthly climatology of zonal-mean zonal wind (black contours; unit is m s^{-1}) in (a-c) February and (d-f) January for observations (ERA-I in 1979-2014; left panels), MIROC6 (middle) and MIROC5 (right) during 60-year period. In panels (g-i), the daily-mean temperatures at the 10 hPa pressure level on the North Pole are plotted.

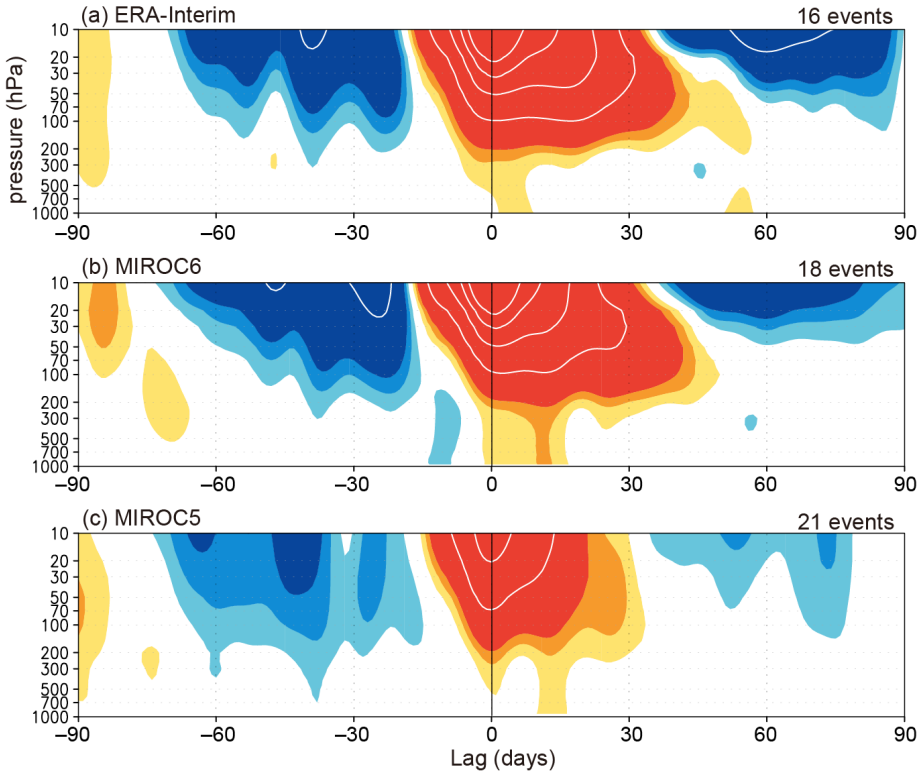

Fig. 25. Composites of time development of the zonal-mean NAM index for stratospheric weak polar vortex events in (a) observations (ERA-I), (b) MIROC6, and (c) MIROC5. The indices having dimension of geopotential height (m), and red colors denote negative values. Interval of colors (contours) is 50 (400) m. The number of events included in the composite are indicated above each panel.

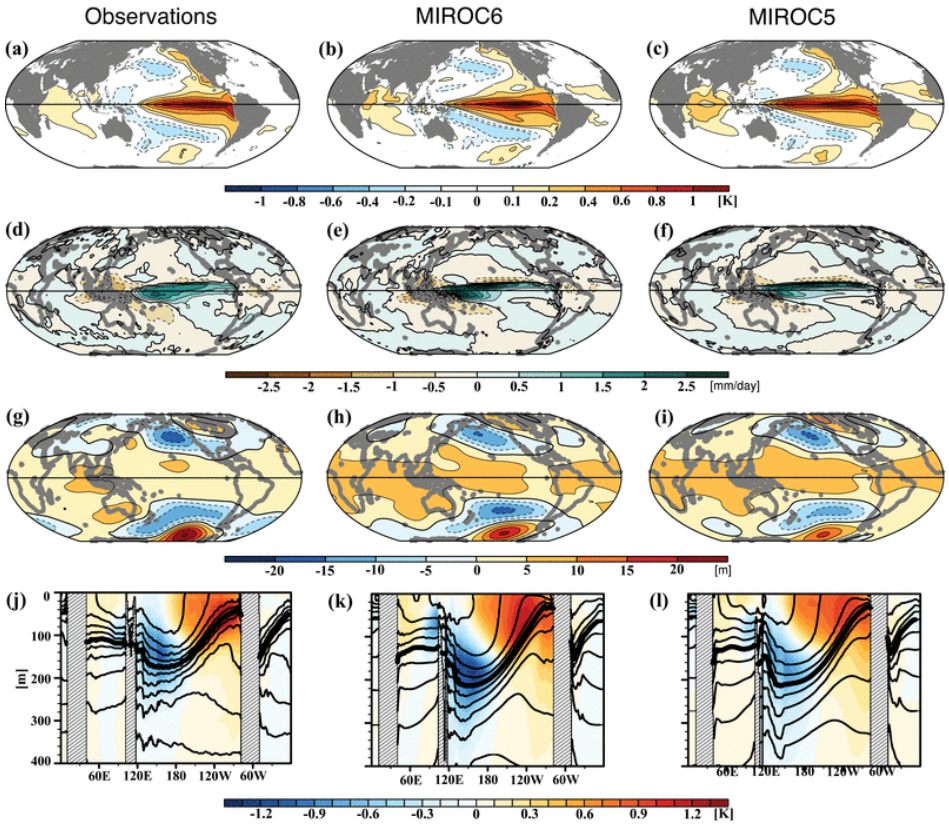

Figure 26. Anomalies of SST (K), precipitation (mm day^{-1}), the 500 hPa pressure height (m), and the equatorial ocean temperature averaged in 5°S–5°N (K) which are regressed onto the Niño3 index. Monthly anomalies with respect to monthly climatology are used here. From the left to the right, the anomalies in observations (ProjD and ERA-I), MIROC6, and MIROC5 are aligned. In the bottom panels, contours denote annual-mean climatological temperature with the 20°C isotherms thickened and the contour interval is 2°C.

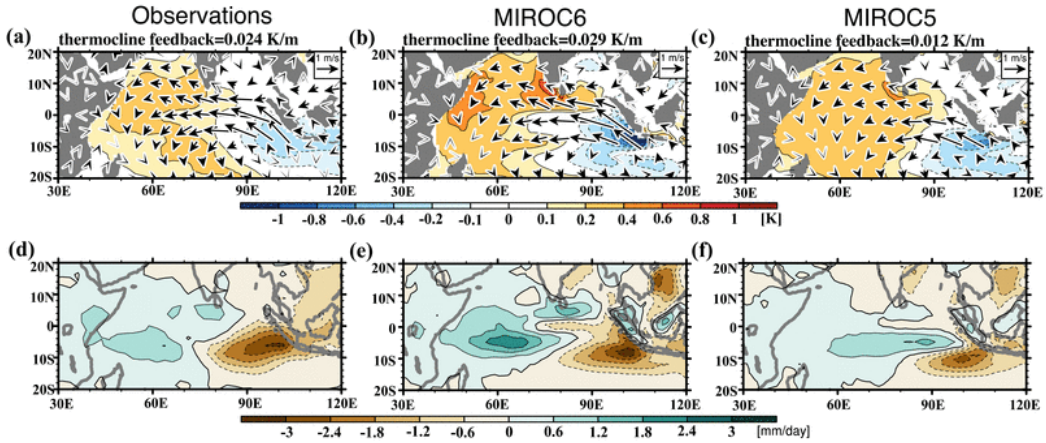

Figure 27. Same as Fig. 26, but for anomalies of SST (colors), 10 m wind vectors (upper panels) and precipitation (lower panels) regressed onto the autumn DMI. The values of the regression slope between anomalies of the 20°C isotherm depth and the SST over the eastern IOD region, which indicates the thermocline feedback, are displayed on the top of the upper panels.

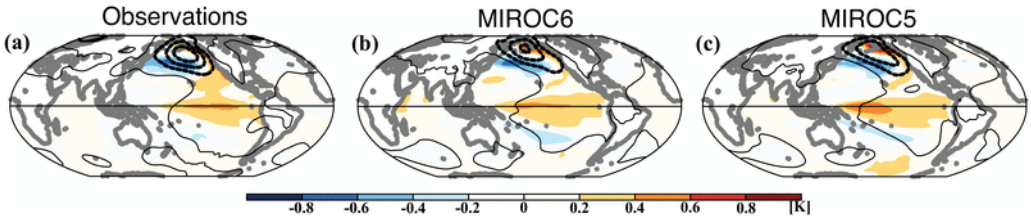

Figure 28. Same as Fig. 26, but for anomalies of monthly SST and wintertime SLP regressed onto the PDO index (see the text). COBE-SST2/SLP2 data in 1900–2013 are used as observations.

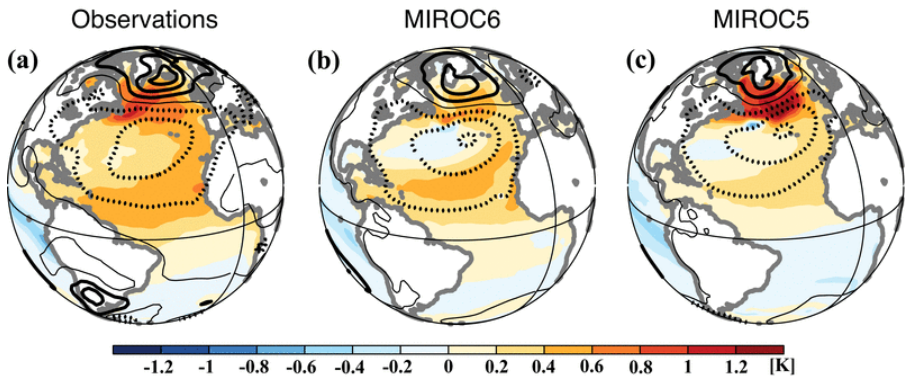

Figure 29. Same as Fig. 26, but for anomalies of SST (colors) and SLP (contours; 0.2 hPa) regressed onto the AMO index (see the text). Negative values are denoted by dashed contours.

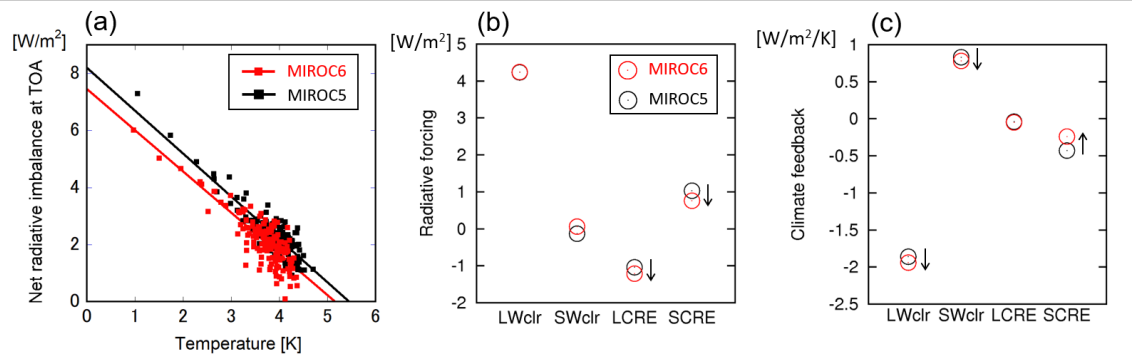

Fig. 30. (a) Global mean net radiative imbalance at the TOA plotted against the global mean SAT increase. Data from the first 150 years after the abrupt CO_2 quadrupling are used. (b) $2 \times CO_2$ radiative forcing estimated by regressing four components of TOA radiation against the global-mean SAT, following Gregory and Webb (2008). (c) Same as (b) but for climate feedback. In Figs. 30bc, LWclr (SWclr) and LCRE (SCRE) denote a clear-sky longwave (shortwave) component and a longwave (shortwave) cloud component, respectively. The arrows in (b) and (c) indicate that the results of MIROC6 are different from MIROC5 at the 5% level.

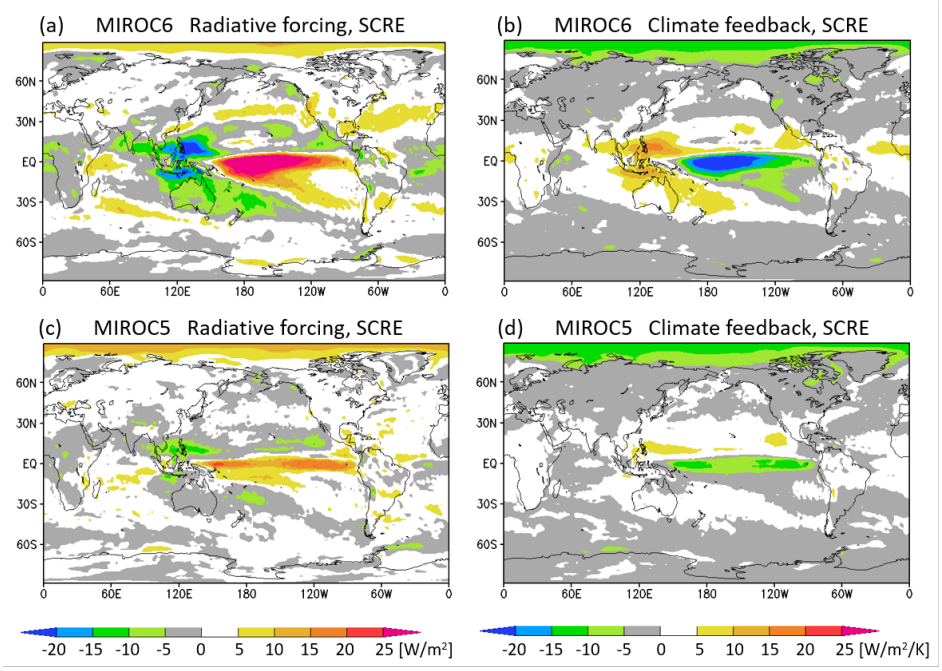

Figure 31. Shortwave cloud component of (a, c) 2 × CO_2 radiative forcing and (b, d) climate feedback in MIROC6 (upper panels) and MIROC5 (lower panels).

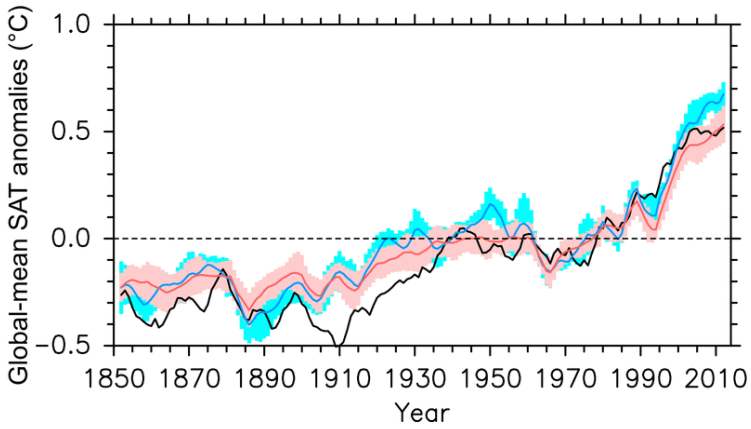

Figure 32. Time series of the global-mean SAT anomalies for observations (black), MIROC6 (red), and MIROC5 (blue). A 5-yr running-mean filter is applied to the anomalies with respect to the 1961–1990 mean. Colors indicate spreads of ensemble experiments for each model (1 standard deviation).

Dataset	Used data period (year)	Reference
CERES (edition 2.8)	2001–2013	Loeb et al. (2009)
ISCCP	Climatology	Zhang et al. (2004)
ERA-Interim	1980–2009	Dee et al. (2011)
GPCPv2	1980–2009	Adler et al. (2003)
EASE-Grid 2.0	1980–2009	Brodzik and Armstrong (2013)
ProjD	1980–2009	Ishii et al. (2013)
SODA	1980–2009	Carton and Giese (2008)
SSM/I	1980–2009	Cavarieli et al. (1991)
NOAA OLR	1974–2013	Liebmann and Smith (1996)
COBE-SST2/SLP2	1900–2013	Hirahara et al. (2014)
HadCRUT	1850–2015	Morice et al. (2012)

Table 1. Summary of observation and reanalysis datasets used as the references in the present manuscript.

Model	ECS [K]	Radiative forcing [W/m^2]	Climate feedback [W/m^2/K]
MIROC6	2.6	3.72*	-1.44
MIROC5	2.7	4.10	-1.50

Table 2. Effective climate sensitivity (ECS), radiative forcing of CO_2 doubling, and climate feedback for MIROC6 and MIROC5. The result of MIROC6 with '*' is different from MIROC5 at the 5% level.

Model	Radiative forcing [W/m^2]				Climate feedback [W/m^2/K]			
	LWclr	SWclr	LCRE	SCRE	LWclr	SWclr	LCRE	SCRE
MIROC6	4.24	-0.06	-1.21*	0.76*	-1.94*	0.78*	-0.05	-0.24*
MIROC5	4.23	-0.13	-1.04	1.03	-1.86	0.83	-0.04	-0.43

Table 3. Radiative forcing of CO_2 doubling and climate feedback for MIROC6 and MIROC5, evaluated with different components of TOA radiation as longwave clear sky (LWclr), shortwave clear sky (SWclr), longwave cloud radiative effect (LCRE), and shortwave cloud radiative effect (SCRE). The results of MIROC6 with '*' are different from MIROC5 at the 5% level.

1815 **Appendix**

1816

		MIROC5 (Watanabe et al., 2010)	MIROC6 (this issue)
Atmosphere	Core	CCSR-NIES AGCM (Numaguti et al., 1997)	Same as MIROC5
	Resolution	T85 (150 km), 40 levels up to 3 hPa	T85 (150 km), 81 levels up to 0.004 hPa
	Cumulus	An entrainment plume model with multiple cloud-types (Chikira and Sugiyama, 2010)	Same as MIROC5
	Shallow conv.	N/A	A mass flux-based single plume model based on Park and Bretherton (2009)
	Aerosol	SPRINTARS (Takemura et al., 2000, 2005, 2009)	Same as MIROC5, but with prognostic precursor gases of organic matters and diagnostic oceanic primary and secondary organic matters.
	Radiation	*k*-distribution scheme (Sekiguchi and Nakajima, 2008)	Same as MIROC5, but with a hexagonal solid column as ice particle habit and extended mode radius of cloud particles.
	Gravity waves	An orographic gravity wave parameterization (McFarlane, 1987)	Same as MIROC5, but with a non-orographic gravity wave parameterization (Hines, 1997)
Land	Core	MATSIRO (Takata et al., 2003)	Same as MIROC5, but with parameterizations for subgrid snow distribution (Liston et al. 2004; Nitta et al., 2014) and a snow-fed wetland (Nitta et al., 2017)
	Resolution	T85 (150 km), 3 snow layers and 6 soil layers down to 14 m depth	Same as MIROC5
Ocean/sea-ice	Core	COCO4.9 (Hasumi, 2004)	Same as MIROC5
	Resolution	Nominal 1.4° (bipolar grid system), 49 levels down to 5500 m	Nominal 1° (tripolar grid system), 63 levels down to 6300 m
	Turbulence	1.5 level turbulent closure model (Noh and Kim, 1999)	Same as MIROC5, but modified turbulent kinetic energy input and smaller background vertical diffusivity under sea-ice (Komuro 2014)

1817

Table A. Summary of the updated configurations from MIROC5 to MIROC6